Investigations of surface plasmon resonances by energy-filtering transmission electron microscopy methods

Dissertation

zur Erlangung des akademischen Grades
Doktor der Naturwissenschaften

(Dr. rer. nat.)

der Technischen Fakultät
der Christian-Albrechts-Universität zu Kiel

Burcu Öğüt
aus Istanbul

Kiel

December 2012

1. Gutachter: Prof. Dr. Wolfgang Jäger
2. Gutachter: Prof. Dr. Peter A. van Aken

Datum der mündlichen Prüfung: 30.01.2013

Dedicated to my parents

Abstract

Miniaturization technology has become an emerging field due to the astonishing trend of the electronic and devices' diminishing down to the nano scale since the beginning of the last decade. The obstacle of today's information technology is the diffraction limit of light, which prevents information transfer at the nano scale. Plasmons which are coherent collective oscillations of quasi-free electrons in a metal volume or on a surface offer numerous application possibilities to transfer information beyond the diffraction limit. However, there are many questions to be answered in the young field of plasmonics in terms of characteristics and applications.

This thesis concentrates on different plasmonic phenomena which are observed with a transmission electron microscope (TEM) in combination with electron energy loss spectroscopy (EELS) and energy-filtering transmission electron microscopy (EFTEM) techniques offering high energy and spatial resolution. Plasmonic coupling behaviour of nanoholes and nanoparticles having rectangular, circular, triangular etc. shapes were investigated using different techniques. The electromagnetic nature of the observed situations was unveiled with different simulation techniques based on discrete dipole approximation (DDA), finite element method (FEM), and three-dimensional finite-difference time-domain methods (3D-FDTD).

In this thesis, firstly hybridization of closely spaced rectangular nanoslits was analyzed in the framework of Babinet's principle. The research proceeds with the first demonstration of toroidal modes in a metal ring formed by an oligomer of holes at optical wavelengths. Moreover the resonant wedge plasmon modes in a triangular nanoprism were observed. Symmetry breaking concepts were intensively discussed as well. It is expected that the findings in this thesis bear great potential for novel applications such as information technology, magnetic data storage, medical science and solar cell engineering.

Zusammenfassung

Seit Beginn des letzten Jahrzehntes erfuhr die Miniaturisierungstechnologie eine herausragende Entwicklung durch den einschneidenden Trend in der Elektronik- und Bauteilverkleinerung bis auf die Nanometerskala. Die Hürde der heutigen Informations technologie ist die Begrenzung durch die Beugung von Licht, die den Informationstransfer auf Nanometerskala verhindert. Kohärente kollektive Oszillationen von quasifreien Elektronen in einem Metallvolumen oder an einer Metalloberfläche bezeichnet man als Plasmonen. Diese bieten zahlreiche Anwendungsmöglichkeiten, um Informationen jenseits des Beugungslimits zu übertragen. Jedoch gibt es eine große Anzahl von Fragen, die auf diesem neuen Gebiet der „Plasmonics“ bezüglich Charakterisierung und Anwendungen beantwortet werden müssen.

Diese Doktorarbeit konzentriert sich auf die verschiedenen Phänomene von Plasmonen, welche mit Hilfe von Transmissions-elektronenmikroskopie (TEM) untersucht wurden. Elekronen-Energieverlust-Spektroskopie (EELS) und energiegefilterte Transmissions-Elektronenmikroskopie (EFTEM) ermöglichen sowohl hohe Energie als auch räumliche Auflösung. Das Verhalten der Kopplung von Plasmonen an Nanolöchern und Nanopartikeln mit unterschiedlichen Formen (rechtwinklig, rund, dreieckig, etc.) wurden mit diesen Methoden untersucht. Elektromagnetische Eigenschaften der untersuchten Geometrien wurden analysiert und interpretiert anhand von verschiedenen Simulationstechniken basierend auf die Discrete Dipole Näherung (DDA), Finite Element Methoden (FEM) und drei dimensionale Finite-Difference Time-Domain Methoden (3D-FDTD).

Erstmals überhaupt gelang es, die Hybridisierung von eng aneinander liegenden Nanoschlitzen mit Hilfe des Babinetschen Prinzips im Rahmen dieser Doktorarbeit zu analysiereren. Ebenfalls zum ersten Mal konnte die toroidale Mode an Bereich optischer Wellenlängen gezeigt werden. Realisiert wurde dies an Löchern in einem Silberfilm, die in Form eines Oligomers angeordnet waren. Darüber hinaus wurde die resonante Kanten-Plasmon-Mode in dreieckigen Nanoprismen untersucht. Außerdem wurden Konzepte zur Symmetriebrechung ausführlich diskutiert. Es ist zu erwarten, dass die Ergebnisse aus dieser Arbeit ein großes Potential haben, neuartigen Anwendungen hervorzubringen, wie zum Beispiel in der Informationstechnologie, der magnetischen Datenspeicherung, in der Medizintechnik und beim Solarzellen-Engineering.

Table of Contents

List of Figures

List of Abbreviations

CCD	Charge Coupled Device
DDA	Discrete Dipole Approximation
DDSCAT	Discrete Dipole Approximation Code
EELS	Electron Energy Loss Spectroscopy
EFTEM	Energy-Filtering Transmission Electron Microscopy
ELNES	Energy-Loss Near-Edge Structure
ESTEEM	Enabling Science and Technology through European Electron Microscopy
EXELFS	Extended Energy-Loss Fine Structure
FEM	Finite Element Method
FIB	Focused Ion Beam
FWHM	Full Width at Half Maximum
3D-FDTD	Three-Dimensional Finite-Difference Time Domain
HFSS	High Frequency Structure Simulator
LSPR	Localized Surface Plasmon Resonance
PCA	Principle Component Analysis
PEC	Perfect Electrical Conductor
PMMA	Poly(methyl methacrylate)
PMC	Perfect Magnetic Conductor
PML	Perfectly Matched Layer
SESAM	Sub-Electron-Volt-Sub Ångstrom Microscope
SP	Surface Plasmon
SPP	Surface Plasmon Polariton
SPR	Surface Plasmon Resonance
STEM	Scanning Transmission Electron Microscopy
TEM	Transmission Electron Microscopy
TM	Transverse Magnetic

CHAPTER 1

General Introduction

Nanotechnology has become the center of attention since the beginning of the twenty-first century, namely "communication age", due to the astonishing trend of optical, electrical, and mechanical devices' metamorphosis to smaller size. It has been discovered that materials fabricated at the nanoscale possess extraordinarily different properties compared to the materials at the macroscale size.

Today's information technology is based on light pulses transferring data through optical fibers. Nanoscale applications sounded rather utopic as the diffraction limit of light was the main handicap to diminish the size to nanometers until the end of 1990's when it was uncovered that plasmons could be the solution to focus or manipulate the direction of the electromagnetic waves below the diffraction limit.[1, 2]

Actually, the first known plasmon effects date back to the 4th century AD. The Lycurgus Cup, exhibited in British Museum, has green colour in the day light and it has red colour when it is illuminated from inside due to the electromagnetic oscillations of gold nanoparticles embedded in the glass.[3] Similarly, gold nanoparticles were widely used to colour stained church windows.

Real plasmon research has started at the beginning of the twentieth century. Firstly Wood has done some experiments and the results, called Wood's anomaly[4] were later on interpreted by Rayleigh[5]. Much later, Fano found that the source of this anomaly might be the excited electromagnetic waves[6]. In 1908, Mie has started to investigate how light is scattered by nanospheres[7]. Subsequentially, Kretschmann[8] and Otto[9] proved that photons can be used to excite plasmons. The pioneering researches of Pines & Bohm[10] and Ritchie[11] have established the fact that some part of the energy losses of electrons passing through thin films are assigned to plasmon excitations, which is the basic idea of measuring plasmon losses with electron energy-loss spectroscopy (EELS). Batson has performed the first EELS experiment to measure plasmonic losses in a metal.[12] Especially after introduction of the plasmonic hybridization theory[13], which gives the possibility to understand plasmonic behaviour from a simpler point of

view, there has been an astounding amount of research about plasmonics. Imaging of localized surface plasmons on a nanoprism with sufficient resolution could only be achieved in 2007[14]. After this, EELS has become a popular way to investigate the optical properties of materials[15]. During this dissertation, the tool that was used for plasmon measurements is EELS and energy-filtering transmission electron microcopy (EFTEM). Technical details of EELS and EFTEM are discussed in chapter 2.

1.1. What are Plasmons?

Metallic bonding is mediated by a free electron gas. This electron gas consists of quasi-free electrons which enable electrical conductivity. Coherent collective oscillations of the quasi-free electrons cause small variations in the density of the electron gas. These oscillations in the volume of the metal are called volume or bulk plasmons. In a free-electron material the energy (E_p) of the volume plasmons are[16];

$$E_p = \hbar\omega_p = \hbar\sqrt{\frac{ne^2}{\varepsilon_0 m_0}} \tag{1.1}$$

where ω_p is the frequency of the volume plasmons, n is the density of electrons per unit volume, e is the electric charge, ε_0 is the permittivity of free space, and m_0 is the rest mass of the electron. If these oscillations occur at the surface of a metal they are named surface plasmons (SPs) with an energy $E_p^{surface} = E_p/\sqrt{2}$.[16] Owing to the spatial variation of the electron density on the surface, a SP is inherently connected with an electromagnetic field and is thus often called surface plasmon polariton (SPP, figure 1.1). As SPPs propagate, the quasi-free electrons move over the metal surface.

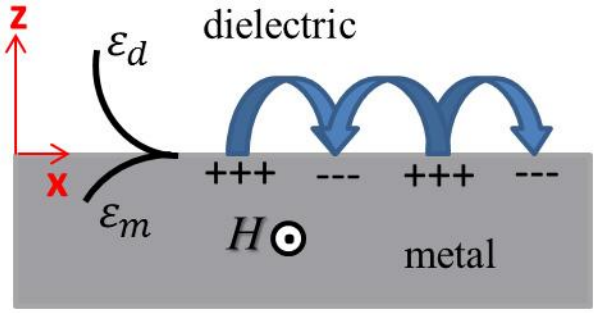

Figure 1.1: Typical behaviour of SPPs propagating over a metallic surface.

The electromagnetic waves propagating along the surface have a transverse magnetic (TM) character, which means that the electric field component has a component in *z*-direction, whereas the magnetic field component has no component in *z*-direction. The magnetic field vector lies along the *y*-direction perpendicular to the propagation direction as shown in figure 1.1.[17]

Surface plasmons are highly localized at the surface and decay exponentially as going further away from the interface (along ± *z*-direction) into the dielectric and metal volume both. The decay length into the vacuum is half of the wavelength of light. The decay length into the

metal is the skin depth, which depends on the wavelength region studied and the type of the metal. For the case of silver and gold, the skin depth is calculated to be around 25–30 nm for the wavelength (energy-loss) region studied throughout this PhD work (figure 1.2). The dielectric function data have been retrieved from another reference[18].

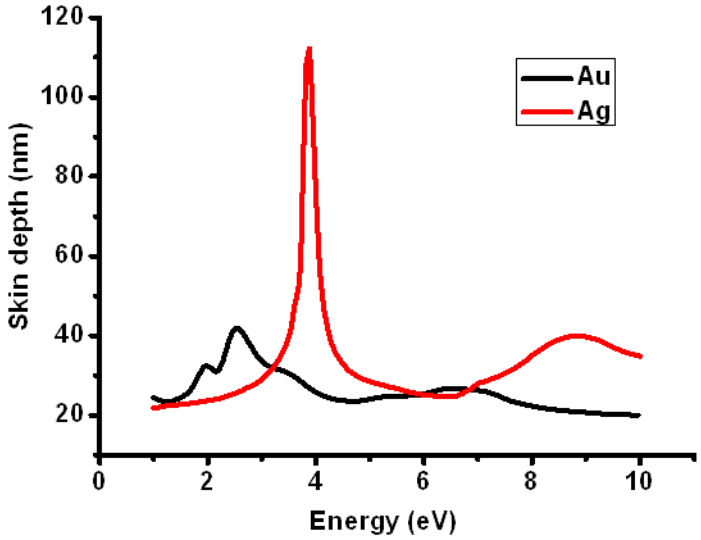

Figure 1.2: The calculated skin depth for silver and gold between 1 eV and 10 eV.

In order to figure out the surface plasmon condition one should start from the Maxwell's equations where there is no external source;[16]

$$\nabla \times H_i = \varepsilon_i \frac{1}{c}\frac{\partial}{\partial t} E_i \tag{1.2}$$

$$\nabla \times E_i = -\frac{1}{c}\frac{\partial}{\partial t} H_i \tag{1.3}$$

$$\nabla \cdot (\varepsilon_i E_i) = 0 \tag{1.4}$$

$$\nabla \cdot H_i = 0 \tag{1.5}$$

Where c is the speed of light and i describes the type of medium. When $z > 0$, i refers to the dielectric and when $z < 0$, it refers to the metal. The electric field component of surface plasmon waves is defined as $E_i = E_o exp(-i\omega t)$, and for the case of electric field having components in x and z direction and magnetic field having components in y direction. If these electrostatic components are inserted into the Maxwell's equations where there is no external source one can calculate the dispersion relation for the wave vector;[19]

$$|k|^2 = k_x^2 + k_y^2 + k_z^2 = \varepsilon k_o^2 \tag{1.6}$$

From equation 1.6, the correlation between the surface plasmon wave vector propagation and the energy is defined by the dispersion relation[20]

$$k_{spp} = \frac{2\pi}{\lambda}\sqrt{\frac{\varepsilon_d \varepsilon_m}{\varepsilon_d + \varepsilon_m}} \tag{1.7}$$

where ε_m and ε_d are the permittivities of metal and the dielectric. $2\pi/\lambda$ stands for the wave vector of bare light. If the dielectric medium is vacuum, as it is the case in chapters 4, 5, 6, and 7, dielectric permittivity (ε_d) is taken as 1. Surface plasmons are signaled with the disappearance of the dielectric function,

$$\varepsilon_d + \varepsilon_m = 0 \tag{1.8},$$

As going from 0 eV to higher energies, surface plasmons converge to the Ritchie's nonretarded plasmon condition[11] signaled by equation 1.8. This condition is indicated by the situation where the SPP dispersion curve becomes flat (figure 1.3).[16] $\varepsilon_m < -\varepsilon_d$ situation has to be satisfied for the existence of surface plasmons. For the cases where the losses are negligible between a metal/vacuum surface, ε_d is 1 and the permittivity of the metal is calculated as $\varepsilon_m = 1 - \frac{\omega_p^2}{\omega}$, where $\omega_p$is the volume plasmon frequency of the metal studied.[21]

From 0 eV to the surface plasmon energy, the dispersion curve (black curve, figure 1.3) bends away from the light line (blue curve), *k*, as the wavevector of plasmons is larger than the wave vector of bare light at a fixed energy.[20] This momentum mismatch is visible in figure 1.3. Only if the magnitude of the wave vector of light becomes equal with the wave vector of plasmons, plasmons can start to resonate with the frequency of the external electromagnetic field. At this condition, the external electromagnetic field of light can couple with surface plasmons.[22] It means that one cannot directly excite plasmons with light. Some special setup such as gratings or total reflection condition has to accompany the light exertion in order to excite plasmons. A comprehensive explanation about how to excite plasmons with EELS technique will be given in chapter 2.

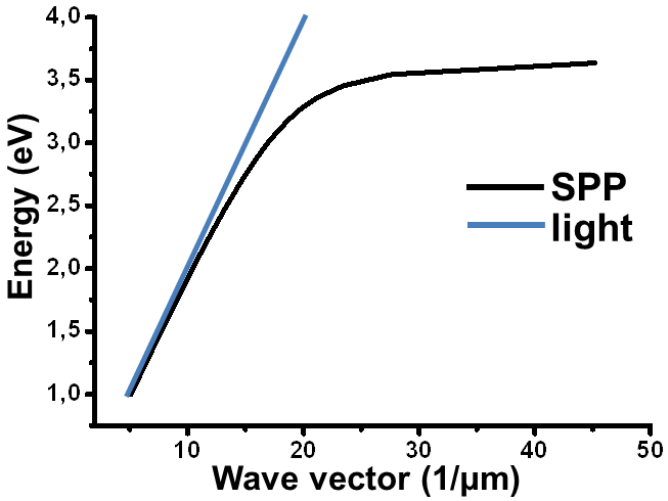

Figure 1.3: A typical dispersion curve for light and a surface plasmon polariton. The SPP curvebends to the right side of light causing a momentum mismatch.

The dispersion relation of surface plasmons requires that the permittivities of the material and the dielectric have to have opposite signs. This condition is well suited for the metal/vacuum interfaces as it will be seen in further discussions in the proceeding chapters. Figure 1.4 shows the values for the real and imaginary components for silver (fig. 1.4a) and gold (fig. 1.4b) between 0 and 10 eV retrieved from the data by Johnson & Christy.[18] The real parts of the dielectric functions of silver and gold have negative values in the optical wavelength regime (~0–4 eV).

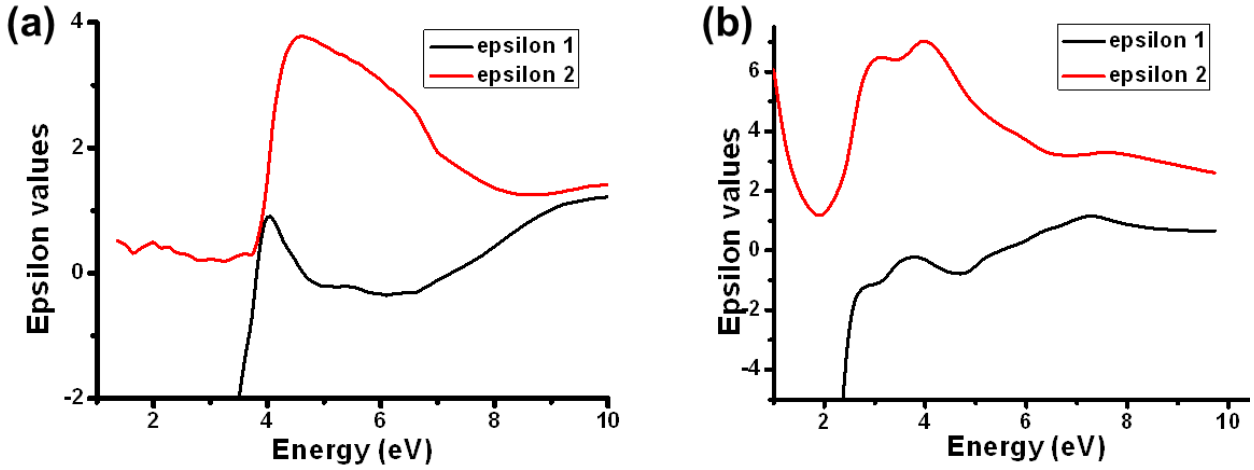

Figure 1.4: Real (black) and and imaginary (red) parts of the complex dielectric function of (a) silver (Ag) and (b) gold (Au) drawn according to the data taken from Johnson and Christy[18].

The things that have been discussed up to this point are valid only if the size of the surface is unlimited. If there is a finite system, surface plasmons are highly localized and resonate on the finite surface, also called as localized surface plasmon resonances (LSPRs). LSPRs happen naturally to the scattering condition of the structures which have sub-wavelength size in an electromagnetic field oscillation. The curved surfaces apply a restoring force on the driven electrons and the electromagnetic field increases in ± z direction.[23] This causes resonant eigenmodes to occur. If two of these resonant systems come together, they electromagnetically couple and hybridize with each other having dipolar, quadrupolar, octupolar etc. nature.

The electric field components due to the surface plasmon resonances (SPRs) shown in Fig. 1.5 were calculated with the High Frequency Structure Simulator (HFSS). As the surface to volume ratio is high, localized surface plasmon resonances are dominant compared to volume plasmons. An elaborate description about the HFSS simulation technique will be given in chapter 3. Localized surface plasmons and their electromagnetic nature in different structures are intensively elucidated in chapters 4–9.

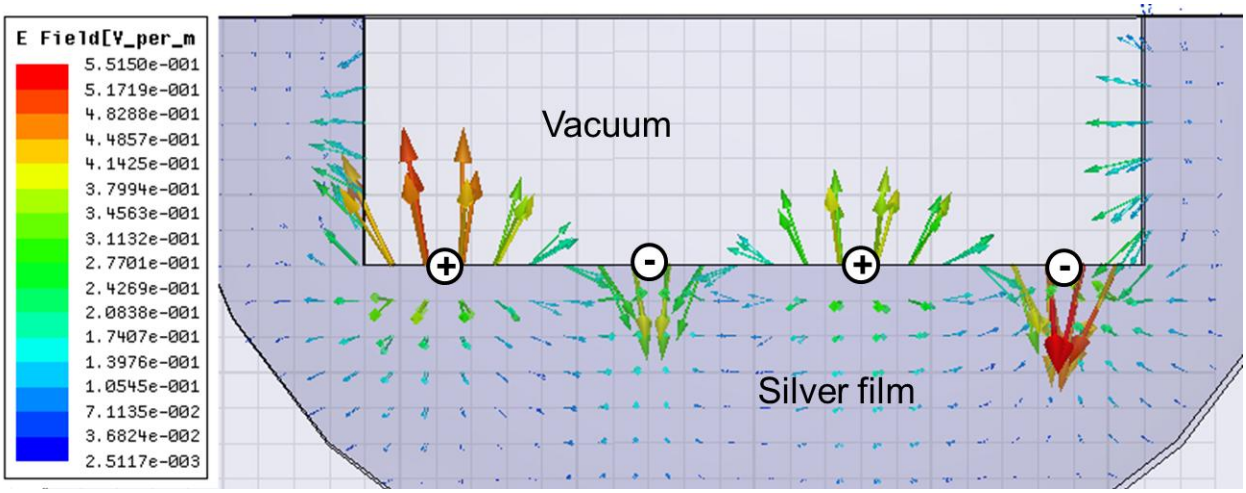

Figure 1.5: Electric field due to a localized surface plasmon resonance at an energy-loss value of 1.71 eV. The strength of the electric field is shown in the legend.

1.2. Application Areas of Plasmons

Today's plasmonics research is mostly application-oriented[24], having a tendency to use nanoparticles and nanoholes as canditates for the possible areas of use. Optical properties of these structures can be modified by altering the geometry, material, and chemical composition at a resonant energy.[25]

Nanoparticles highly sustain SPRs. In addition, they scatter light intensively, which enables easy detection of plasmons with various methods. Noble metals such as gold, silver, and copper are highly preferred materials for production of nanoparticles. Due to these properties, nanoparticles could be the best canditates for biological[26] and chemical[27] sensing, particularly cancer diagnostics[28] and treatment[29] by combining protein chains to them to chase the tumors. For biological applications, the most widely used material is gold since other elements such as silver and copper are poisonous.

Furthermore, electromagnetic waves can easily be manipulated if several nanoparticles or holes are electromagnetically coupled, so that SPPs can propagate forward the necessary information at high speed in plasmonic computers of the future.[30,31] Electromagnetically coupled nanoholes with a special configuration can lead to a nearly radiation free character, which promises applications in solar cell applications and Purcell effect engineering (see chapter 5). Graphene offers applications in optoelectronics as well.[32] Furthermore, plasmons promise applications in near-field optics[33] and surface-enhanced Raman spectroscopy[34]. Metamaterials which are artificial materials with properties non-existing in nature (e.g. negative refractive index) can be another example for the borderline applications of plasmons.[35]

Although there is an enormous amount of research about plasmonic applications concerning particles and holes, there are still several questions to be answered such as, how grain boundaries and crystallographic orientation affect the plasmonic behaviour. In order to investigate these effects, instruments offering even higher energy and spatial resolution are necessary. This will be a further challenge for the development of electron microscope technology.

1.3. Outline of this Dissertation

In this thesis, EELS and EFTEM experiments used to investigate the plasmonic behaviour of various structures were supported by simulations based on discrete-dipole approximation (DDA), finite-element method (FEM), and three-dimensional finite-difference time-domain (3D-FDTD) solutions of Maxwell's equations. I principally dealt with EFTEM imaging, and simulations based on DDA and FEM. 3D-FDTD simulations were performed by Nahid Talebi. This dissertation comprises on five articles published in different scientific journals and one manuscript in preparation. Detailed information about the contributions of the co-authors can be found at the beginning of each chapter. The organization of the chapters is in the following manner:

Chapter 2 is mainly about the experimental methods, specifically an overview of transmission electron microscopy (TEM), EELS and EFTEM. Also the sample preparation techniques are summarized.

Chapter 3 is devoted to the basics of the simulation methods that have been used to obtain deeper insight into the electromagnetic behaviour: The DDA code (DDSCAT), the FEM code (HFSS), and 3D-FDTD code.

Particles and holes having the same geometry behave in a complementary manner. This correlation is intensively discussed in chapter 4 [36] comprising the research about the single and double rectangular slits drilled into a silver film. The experimental method that was used for this purpose was EFTEM. In order to comprehend the electromagnetic nature of the structures, HFSS simulations were achieved. The results are discussed in the framework of Babinet's Principle.

Chapter 5 focuses on the toroidal eigenmodes of circular nanohole aggregates in the benzene configuration detected by EFTEM combined with 3D-FDTD simulations. [37]

Chapter 6 further investigates the coupling behaviour in the nanoholes which are configured as artificial hexamers and pentamers with EFTEM and 3D-FDTD simulations.

In chapter 7, plasmon resonances are observed in a grape-like structure comprised of nine circular holes by EFTEM. The simulations based on DDA demonstrate the dipolar and quadrupolar resonances in the singular holes. [38]

Chapter 8 proceeds with the investigation of nanoprisms. This chapter concentrates on the measurements of surface plasmon resonances in gold nanoplatelets with different geometric shapes at high spatial resolution with EFTEM, supported with 3D-FDTD simulations.[39]

Chapter 9 systematically investigates the surface plasmon resonances in triangular systems. Effects of placing another triangular particle nearby are studied in terms of symmetry breaking of plasmonic eigenmodes by EFTEM combined with 3D- FDTD simulations.[40]

Conclusions and future outlook of this doctorate work are summarized in chapter 10.

References:

1. Maier, S.A.; Kik, P.G.; Atwater, H.A.; Meltzer, S.; Harel, E.; Koel, B.E.; Requicha, A..G. Local detection of electromagnetic energy transport below the diffraction limit in metal nanoparticle plasmon waveguides, *Nature Mater.* **2**, 229-232 (2003).
2. Gramotnev, D.K.; Bozhevolnyi S.I. Plasmonics beyond the diffraction limit *Nat. Photon.* **4**, 83-91 (2010).
3. Barber, D.J.; Freestone, I.C. An investigation of the origin of the colour of the Lycurgus cup by analytical transmission electron microscopy, *Archeometry* **32**, 33-45 (1990).
4. Wood, R.W. On a remarkable case of uneven distribution of light in a diffraction grating spectrum, *Phil. Mag*. **4**, 396-402 (1902).
5. Rayleigh, L. Note on the remarkable case of diffraction spectra described by Prof. Wood, *Phil. Mag.* **14**, 60-65 (1907).
6. Fano, U. The theory of anomalous diffraction gratings and quasi-stationary waves on metallic surfaces (Sommerfeld's waves*) J. Opt. Soc. Am.* **31**, 213-222 (1941).
7. Mie, G. Beiträge zur Optik trüber Medien, speziell kolloidaler Metallösungen, Ann. Phys. (Leipzig) **25**, 377 (1908).
8. Kretschmann, E.; Raether, H. Radiative decay of non-radiative surface plasmons excited by light, *Z. Naturf.* **23A**, 2135, (1968).
9. Otto, A. Excitation of nonradiative surface plasma waves in silver by the method of frustrated total reflection, *Z. Phys.* **216**, 398 (1968).
10. Pines, D.; Bohm, D. A collective description of electron interactions: II. collective *vs* individual Particle Aspects of the Interactions *Phys. Rev.* **85**, 338– 353 (1952).
11. Ritchie, R. H. Plasma losses by fast electrons in thin films *Phys. Rev.* **106**, 874– 881, (1957).
12. Batson, P. E. Surface plasmon coupling in clusters of small spheres *Phys. Rev. Lett.*, **49**, 936– 940, (1982).
13. Prodan, E.; Radloff, C.; Halas, N.J.; Nordlander, P. A hybridization model for the plasmon response of complex nanostructures, *Science* **120**, 5444– 5454, (2004).
14. Nelayah, J.; Kociak, M.; Stephan, O.; Garcia de Abajo, F. J.; Tence, M.; Henrard, L.; Taverna, D.; Pastoriza-Santos, I.; Liz-Marzan, L. M.; Colliex, C.Mapping Surface Plasmons on a Single Metallic Nanoparticle *Nat. Phys.* **3**, 348– 353, (2007).

15. Garcia de Abajo, F.J. Optical excitations in electron microscopy, *Rev. Mod. Phys.* **82**, 209-275 (2010).
16. Pitarke, J.M.; Silkin, V.M.; Chulkov, E.V.; Echenique, P.M. Theory of plasmons and surface plasmon polaritons, *Rep. Prog. Phys.* **70**, 1-87 (2007).
17. Barnes, W.L.; Dereux, A.; Ebbesen, T.W. Surface plasmon subwavelength optics, *Nature* **424**, 824-830, (2003).
18. Johnson, P.B.; Christy, R.W. Optical constants of noble metals, Phys Rev. B 6, 4370-4379, (1972).
19. Bozhevolnyi, S.I. *Plasmonic nanoguides and circuits*, Pan Stanford Publishing, 2009.
20. Raether, H. *Surface Plasmons on Smooth & Rough Surfaces and on Gratings*, Springer Verlag, 1986.
21. Egerton, R.F. *Electron Energy-Loss Spectroscopy in the Electron Microscope*, Springer, 2011.
22. Brongersma, M. L.; Kik, P.G. *Surface plasmon nanophotonics*, Springer, 2007.
23. Maier, S.A. Plasmonics fundamentals and applications, Springer, 2007.
24. Halas, N.J. Connecting the dots: Reinventing optics for nanoscale dimensions, *Proc. Natl. Acad. Sci. USA* **106**, 3643-3644 (2009).
25. Halas, N.J.; Lal, S.; Link, S.; Chang, W.S.; Natelson, D.; Hafner, J.H.; Nordlander P. A Plethora of plasmonics from the laboratory for nanophotonics at rice university *Advanced Materials* **24**, 4842-4877 (2012).
26. Anker, J.N.; Hall, W.P.; Lyandres, O.; Shah, N.C.; Zhao, J.; Van Duyne, R.P. Biosensing with plasmonic nanosensors, *Nature Mater.* **7**, 442-452, (2008).
27. Tittl, A.; Mai, P.; Taubert, R.; Dregely, D.; Liu, N.; Giessen, H. Palladium-Based plasmonic perfect absorber in the visible wavelength range and its application to hydrogen sensing *Nano Lett.*, **11**, 4366– 4369, (2011).
28. El-Sayed, I. H.; Huang, X.; El-Sayed, M. A.Surface Plasmon Resonance Scattering and Absorption of Anti-EGFR Antibody Conjugated Gold Nanoparticles in Cancer Diagnostics: Applications in Oral Cancer *Nano Lett.* **5**, 829– 834, (2005).
29. Lal, S.; Clare, S. E.; Halas, N. J.Nanoshell-Enabled Photothermal Cancer Therapy: Impending Clinical Impact *Acc. Chem. Res.* **41**, 1842– 1851, (2008).

30. Ebbesen, T.W.; Lezec, H.J.; Ghaemi, H.F.; Thio, T.; Wolff, P.A. Extraordinary optical transmission through subwavelength hole arrays, *Nature* **391**, 667-669 (1998).
31. Zia, R.; Schuller, J.A.; Chandran, A.; Brongersma, M.L. Plasmonics: the next chip-scale technology, *Mater. Today*, **9**, 20-27, (2006).
32. Koppens, F.H.L.; Chang, D. E.; Garcia de Abajo, F.J. Graphene plasmonics: a platform for strong light-matter interactions, *Nano Lett.* **11**, 3370-3377 (2011).
33. Grosse, N. B.; Heckmann, J.; Woggon, U. Nonlinear plasmon-photon interaction resolved by k-space spectroscopy, *Phys. Rev. Lett.*, **108**, 136802 (2012).
34. Kneipp, K.; Wang, Y.; Kneipp, H.; Perelmann, L. T.; Itzkani, I.; Dasari, R. R.; Feld, M.Single Molecule Detection Using Surface-Enhanced Raman Scattering *Phys. Rev. Lett.* **78**, 1667– 1670, (1997).
35. Liu, N.; Liu, H.; Zhu, S.; Giessen, H. Stereometamaterials, *Nature Photon.* **3**, 157-162 (2009).
36. Ögüt, B.; Vogelgesang, R.; Sigle, W.; Talebi, N.; Koch, C.T.; van Aken, P.A., Hybridized metal slit eigenmodes as an illustration of Babinet's Principle", *ACS Nano*, **5**, 6701-6706, (2011).
37. Ögüt, B.; Talebi, N.; Vogelgesang, R.; Sigle, W.; van Aken, P.A. Toroidal plasmonic eigenmodes in oligomer nanocavities for the visible, *Nano Lett.*, **12**, 5239-5244, (2012).
38. Sigle, W.; Nelayah, J.; Koch, C.T.; Ögüt, B.**;** Gu, L.; van Aken, P.A. EFTEM Study of Surface Plasmon Resonances in Silver Nanoholes, *Ultramicroscopy*, **110**, 1094-1100, (2010).
39. Gu, L.; Sigle, W.; Koch, C.T.; Ögüt, B.; van Aken, P.A.;Talebi, N.; Vogelgesang, R.; Mu, J.; Wen, X.;Mao, J. Resonant Wedge Plasmon Modes in Single Crystalline Gold Nanoplatelets, *Phys. Rev. B*, **83**, 195433, (2011).
40. Talebi, N.; Sigle, W.; Vogelgesang, R.; Koch, C.T.; Fernández-Lopez, C.; Liz-Marzán, L.M.; Ögüt, B.; Rohm, M.; van Aken, P.A. Breaking the mode degeneracy of surface plasmon resonances in a triangular system, *Langmuir*, **28**, 8867-8873, (2012).

CHAPTER 2

Experimental Methods

2.1. Transmission Electron Microscopy (TEM)

TEM offers very high energy and spatial resolution especially after the introduction of aberration correctors and electron monochromators. EELS and EFTEM are the two analytical TEM methods based on the inelastic interaction between the electron beam and the investigated specimen.[1] Monochromated electrons are sent through the target specimen. While the electrons are passing they interact with the specimen and the energy loss of the electrons is measured by the energy filter. The convergent illumination condition at TEM is shown in figure 2.1. At convergent illumination condition, the electron beam is focused onto the specimen with an angle α (convergence angle) and electrons up to a maximum scattering angle β (collector angle) are collected by the spectrometer.[2] These angles are important for EELS. Conventional TEM (CTEM) and scanning transmission electron microscopy (STEM) are correlated to each other by the reciprocity theorem.[1] Therefore, the role of the objective aperture and the collection aperture are exchanged for the case of illumination in the STEM mode. The image resolution mainly depends on the quality of the objective lenses used. Imperfections of the objective lens cause spherical aberrations. This is minimized at today's technology with the C_s-corrected TEMs.

The sub-electronvolt sub-Ångstrom microscope (SESAM) from Carl Zeiss (Oberkochen, Germany) was the main instrument where the experiments were carried out. SESAM works at an accelerating voltage of 200 kV.[3,4] It has a Schottky field emission gun, the MANDOLINE filter, and a symmetric electrostatic omega-type monochromator. The omega-type monochromator enables an energy resolution better than 100 meV. The MANDOLINE filter offersa high dispersion of about 6 μm/eV, and very small non-isochromaticity. High energy resolution enables imaging plasmon modes in the visible and infrared wavelength regimes, which have been hindered for a long time due to the masking of the tail of the intensive zero-loss peak. The spatial resolution in the energy-loss region of interest is around 10–15 nm. Alternatively, optical methods such as far-field microscopy and apertureless scanning near-field optical microscopy

(aSNOM) could also be applied for plasmon research[5]. A further advantage is that electrons allow excitation also of optically dark modes over a wide energy range at high spatial resolution.

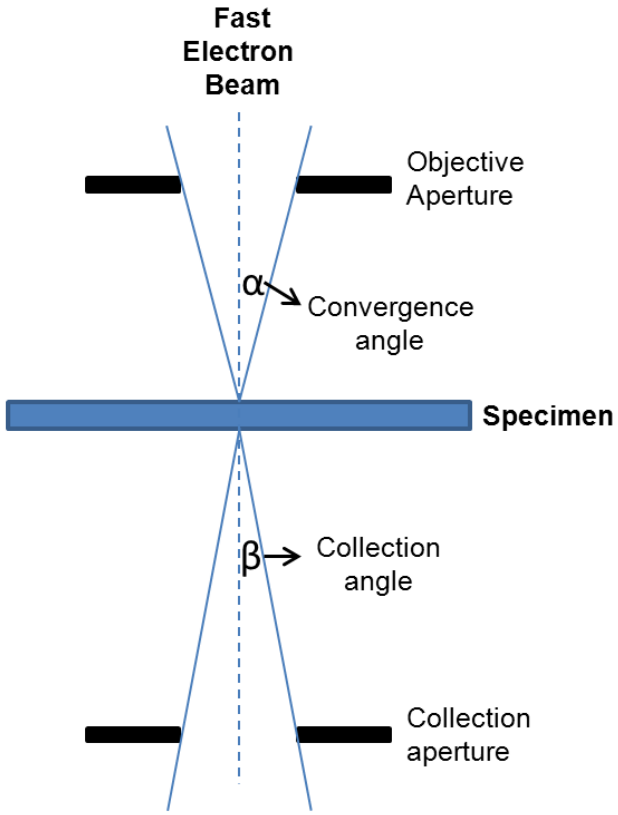

Figure 2.1: Convergent-beam illumination condition in the TEM. Convergence and collection angles depend on the size of the objective and collection apertures.[2]

Fast electrons penetrating an electron-transparent specimen interact with the material both elastically and inelastically via Coulomb forces.[6] A wealth of structural and chemical information about the investigated specimen can be obtained from the elastic and inelastic scattering processes. Among the inelastic scattering processes, the ones which happen due to collective oscillations of the quasi-free electrons attributed to plasmon excitations are the main center of concentration in this thesis. This chapter mainly concentrates on the experimental methods that have been used in order to measure and image surface plasmon resonances and plasmon eigenmodes in different structures.

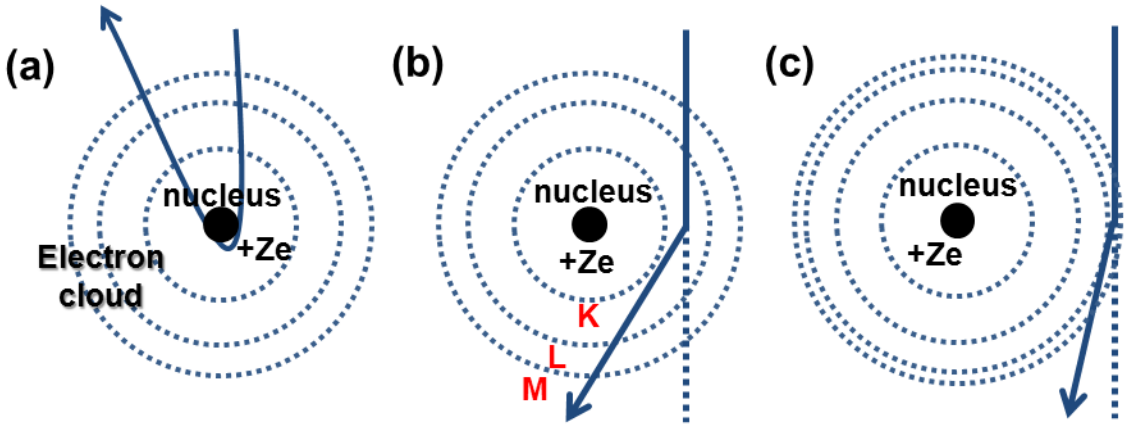

Figure 2.2: A single-atom picture of the Bohr model showing (a) elastic scattering and inelastic scattering involving (b) inner-shell ionization, and (c) outer-shell ionization.

According to the Bohr model[7], electrons of an atom are confined on shells surrounding the positively charged nucleus (figure 2.2). The shells exhibit different energies. Inelastic scattering involves energy transfer to one or several of these electrons whereas in elastic scattering processes no electron excitation takes place and the fast electron does not lose energy, but changes momentum. If the fast electron passes close to the nucleus it can be scattered at high angle or even back scattered and the scattering resembles Rutherford scattering with a near Z^2-dependence (figure 2.2.a). This is used in Z-contrast imaging.

During inelastic scattering[1], the fast electrons loose some amount of kinetic energy due to the interaction of the incoming electron beam with the inner and outer shell electrons (figure 2.2.b & c). If this interaction occurs with an inner-shell (K, L, M) core electron (figure 2.2.b), it absorbs some energy from the fast electron and the core electron is excited to an energy state above the Fermi level. This high-energy state of the atom is compensated by releasing X-rays or Auger electrons after an electron from an outer shell has filled the core hole.

Collision of a fast electron beam with outer-shell electrons can be used to observe interband transitions and plasmon excitations. Interband transition occurs if the fast electron interacts with a single electron from the outer shells. An outer-shell electron is then transferred from the valence band to the conduction band. Secondary electrons might be released if the energy of the excited electron is high enough to leave the atom and to reach the surface of the specimen. As a secondary relaxation process, cathodoluminescence occurs when the hole in the valence band is filled by another electron from the conduction band accompanied by the emission of a photon. Instead of cathodoluminescence the excess energy can be released as heat as well. Actually, this technique is another alternative for measuring the plasmon resonances[8]. As

it is beyond the scope of this work, it is not explained in detail. Unlike interband transitions, plasmons are collective oscillations of the electrons in the conduction and valence bands. Interaction of the fast electron with the outer-shell electrons leads to scattering angles that are smaller (figure 2.2.c) compared to inner-shell excitations.

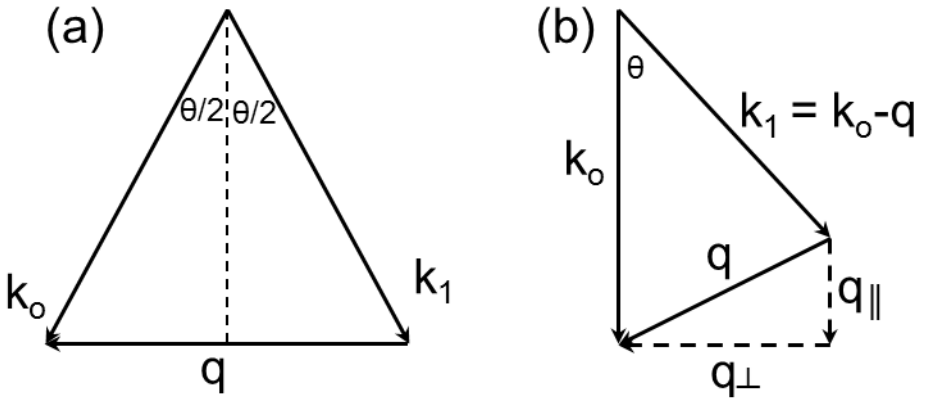

Figure 2.3: Wave vector diagram for (a) elastic scattering, and (b) inelastic scattering.

The initial and final wave vectors for elastic and inelastic scattering are shown in figure 2.3.[9] Momentum is always conserved for both cases. For the elastic scattering case (figure 2.3.a) the wave vector before and after the scattering procedure are equal in magnitude and the scattering vector (q) is calculated as $\boldsymbol{2k_o \sin \theta/2}$. During inelastic scattering, the magnitude of the wave vector changes and the scattering vector has a value of $\boldsymbol{q^2 = k_o^2(\theta^2 + \theta_E^2)}$, where θ_E is the characteristic scattering angle related with the energy loss by $\boldsymbol{\theta_E = \Delta E/2E_o}$. For small scattering angles, q is much smaller than k and therefore it can be decomposed into its components as shown in figure 2.3.b as $\boldsymbol{q_\perp = k_o \sin \theta \approx k_o \theta}$, and $\boldsymbol{q_\parallel = k_o \theta_E}$. It means that at low energy losses momentum transfer converges to the perpendicular component, whereas at high energy losses it converges to the parallel component.

2.2. Electron Energy-Loss Spectroscopy (EELS)

EELS analyzes the changes of the kinetic energy of the electrons travelling through the material, displayed as an electron energy-loss spectrum. Figure 2.4 shows a typical electron energy-loss spectrum of $SrTiO_3$. The zero-loss peak is the most intense peak and is mainly caused by elastically scattered electrons and electrons which has suffered negligible amount of energy loss that cannot be measured with today's technology. Phonons which are collective lattice vibrations can be given as a good example for that. They cause an electron energy loss of ~ 0.01-0.02 eV.

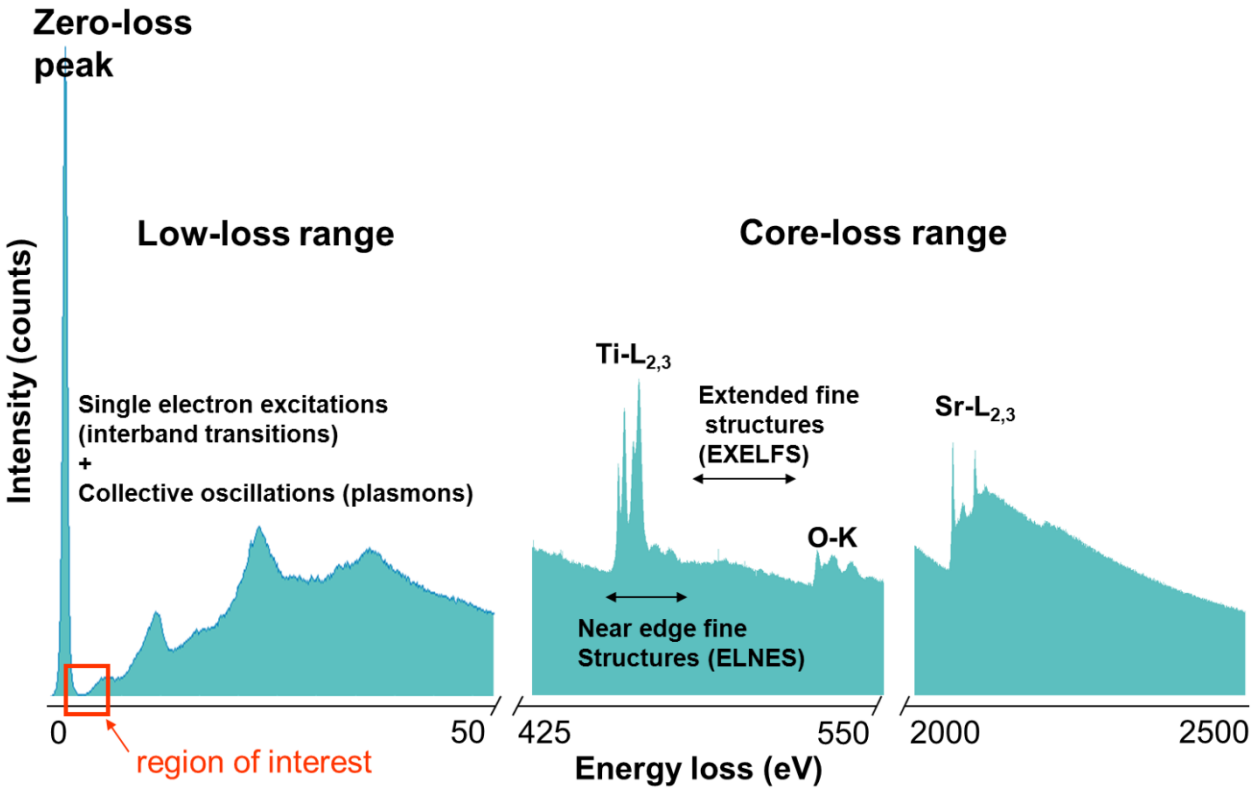

Figure 2.4: A typical EELS spectrum belonging to $SrTiO_3$, showing the low-loss and core-loss regions. The main region of interest has been marked with a red rectangle.[2]

The core-loss region covers the energy-loss range above about 50 eV, where one can detect inner-shell ionization edges. These can be used to unravel the chemical composition and electronic structure of a material. The core-loss range, shown in figure 2.4., is magnified 500 times with respect to the low-loss range and the zero-loss peak because the intensity is lower due to the high dynamic range in the EELS spectrum. The shape of the inner-shell absorption edges

is called energy-loss near-edge structure (ELNES), which gives information about the unoccupied electron density of states. Weak oscillations well above the edge onset are called extended energy-loss fine structure (EXELFS) and can be used for the determination of the local atomic ordering around the excited atom.

The energy-loss region between 0–50 eV is called low-loss region. It contains information about the optical properties of the investigated material (such as the complex dielectric permittivity and band gaps), inter- and intraband transitions, and electromagnetic fields due to volume and surface plasmon losses. The investigated materials in this thesis were silver and gold. The bulk plasmon energies of gold and silver are calculated to be 2,4 eV and 3.8 eV, respectively.[10,11] As the thickness of the investigated specimen increases, the number of scattering events will increase and multiple plasmon peaks will be measured. Therefore, the low-loss region is also used to measure specimen thickness by evaluating intensities of multiple inelastic scattering processes the number of which increases with the thickness of the material. An example of the thickness measurement will be given in the next section. Besides, plasmon losses are advantageous for determining the physical and chemical properties of materials as the plasmon energy changes with the alloy composition[12] and the amount of strain[13].

The energetic position and the intensity of the energy-loss peaks that appear in the low-loss region of an EELS spectrum highly depend on the type of the investigated solid, specifically on the dielectric function, $\varepsilon(E)$, of the material. The dielectric function describes the response of the solid to an external electromagnetic field, e.g. the fast electron. A travelling electron passing by a dielectric leads to polarization. The polarization field acts back on the fast electron and the *z*-component of this field leads to an energy loss. The differential inelastic scattering cross-section can be written as[14]

$$\frac{d\sigma_i}{dE} = \frac{2}{\pi a_o m_o v^2 n_a} Im\left(\frac{-1}{\varepsilon(E)}\right) ln\left[1 + \left(\frac{\beta}{\theta_E}\right)^2\right] \tag{2.1}$$

where a_o is the Bohr radius, m_o is the electron rest mass, n_a is the atom density of the investigated material, v is the velocity of the travelling electrons, β is the collection angle and θ_E is the scattering angle. The imaginary part of the reciprocal dielectric function is called the energy-loss function. The logarithmic part of the above equation stands for the angular scattering distribution. For the case where the EELS spectrum is recorded with very small collection angle the result can be compared to optical data. Then, the complex dielectric function $\varepsilon(E) =$

$\varepsilon_1(E) + i\varepsilon_2(E)$ can directly be calculated as a function of energy by a Kramers–Kronig analysis[1]. In addition, refractive index, absorption coefficient and reflectivity can be calculated. The real part of the dielectric function represents the permittivity, whereas the complex part represents absorption effects. The energy-loss function can be written as,[1]

$$Im\left(\frac{-1}{\varepsilon(E)}\right) = \frac{\varepsilon_2}{\varepsilon_1^2 + \varepsilon_2^2} \tag{2.2}$$

The energy loss function can be written as a function of energy since it determines the energy of the peak that will be seen in the EELS spectrum after the inelastic scattering,[1]

$$Im\left(\frac{-1}{\varepsilon(E)}\right) = \frac{E_p^2(E\,\hbar/\tau)}{\left(E^2 - E_p^2\right)^2 + (E\,\hbar/\tau)^2} = \frac{E\left(\Delta E_p\right)E_p^2}{\left(E^2 - E_p^2\right)^2 + \left(E\,\Delta E_p\right)^2} \tag{2.3}$$

where E_p is the plasmon energy that was previously defined in chapter 1 and τ is the relaxation time when the plasmons decay. ΔE_p symbolizes the full width at half maximum value (FWHM) of the energy loss function. The FWHM reaches a maximum value at the energy loss defined by $E_{max} = \left[E_p^2 - \left(\Delta E_p^2/2\right)\right]^{1/2}$.[1]

For the case of the surface plasmons, the peak width yields as $\Delta E_s = E_s\varepsilon_2(1 + \varepsilon_1)^{-3/2}$ if the damping effect is assumed to be negligible.[1] The intensity of the surface plasmons are identified by the probability of the scattering per angle instead of the cross section, which is the case for the volume plasmons. In general in order to calculate this intensity of the surface plasmon peak, it is necessary to know the energy dependence of both, the dielectric and the metal permittivities, indicated as ε_a and ε_b below. For the perpendicular incidence, the probability is computed as;[15]

$$\frac{dP_s}{dE} = \frac{1}{\pi a_o k_o T}\left(\frac{\tan^{-1}\frac{\beta}{\theta_E}}{\theta_E}\right) Im\left(\frac{-4}{\varepsilon_a + \varepsilon_b} + \frac{1}{\varepsilon_a} + \frac{1}{\varepsilon_b}\right) \tag{2.4}$$

Where the term T corresponds to the nonrelativistic incident energy described as $m_o v_o^2/2$.[13] The last two terms $\frac{1}{\varepsilon_a}$ and $\frac{1}{\varepsilon_b}$ exist in the imaginary term representing the begrenzungs effect. The Begrenzungs effect is a side effect of the surface plasmon excititation causing a diminishing of the volume plasmon peak intensity.[15] The possibility of surface plasmon excitation rather than volume plasmon excitation ascends as the path of the travelling electron gets further away from the surface. Furthermore, the geometrical shape of the investigated

structure plays a role as well. Actually the energy loss function of the surface plasmons can be calculated via many different ways[16, 17], but for simplicity, it is most of the time accepted as $Im\left(\frac{-1}{\varepsilon+p}\right)$, where p represents the geometry dependent dimensionless variable.[18] For bulk plasmon losses that variable is 0, whereas for a planar surface p becomes equal to 1. An example of an energy loss function calculation for silver is demonstrated in figure 2.5. The energy-loss functions belonging to volume (blue curve), and surface losses (pink curve) show that surface plasmon energy (3.6 eV) is slightly smaller than the volume plasmon energy (3.8 eV).

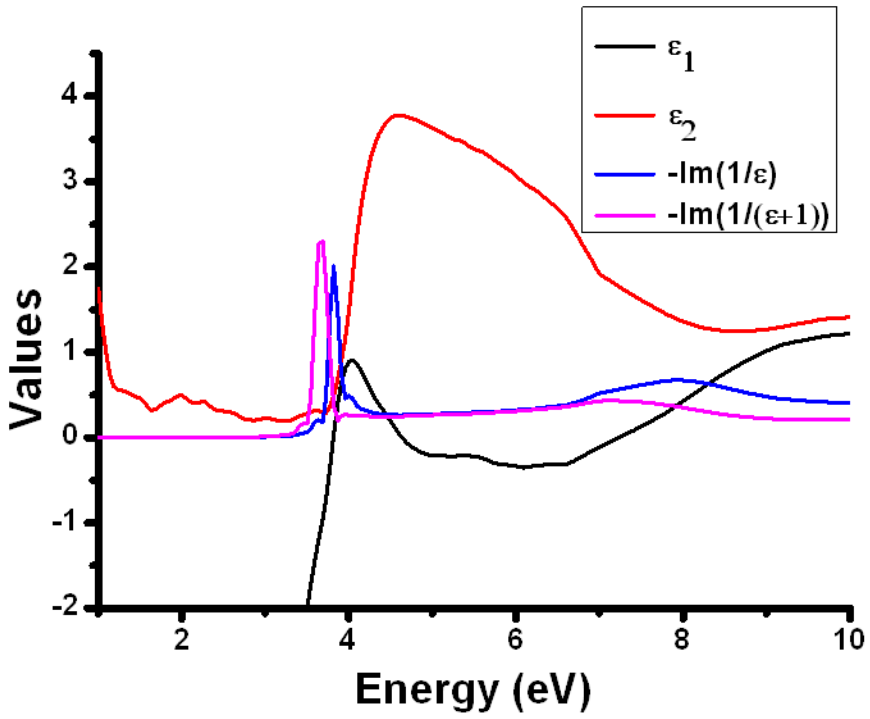

Figure 2.5: Real (black) and and imaginary (red) parts of the complex dielectric function according to the data retrieved from Johnson and Christy[19], and the calculated energy loss function for volume (blue) and surface (pink) plasmon excitations.

Although there is plenty of information about the electronic structure of the specimen that can be reached via equations 2.3 and 2.4, the energy-loss function still fails to capture information about all of the additional phenomena that occur during the electron beam transmission (e. g. spatial dispersion, retardation). For example, in these equations it is assumed that the thickness of the specimen is high enough so that there is no coupling between the upper and lower surfaces of the material. Cerenkov radiation, which becomes especially important for band gap measurements in semiconductors, is another effect that partly restricts the interpretation of low loss data. Cerenkov radiation occurs when the charged particle exceeds the speed of light

below band gap frequency while passing through the specimen due to the coupling of electric and magnetic fields. Cerenkov radiation becomes prominent especially in thicker specimens.[16]

Another effect is the guided light modes. In this case, the electromagnetic waves propagate in a normal way with sinusoidal character inside the material but these waves decay exponentially as going further away from the surface.

2.3. Energy-Filtering Transmission Electron Microscopy (EFTEM)

EFTEM is based on acquiring energy-filtered image series at different energies of the transmitted fast electrons by parallel illumination. Figure 2.6 shows the experimental setup of the Zeiss SESAM[3].

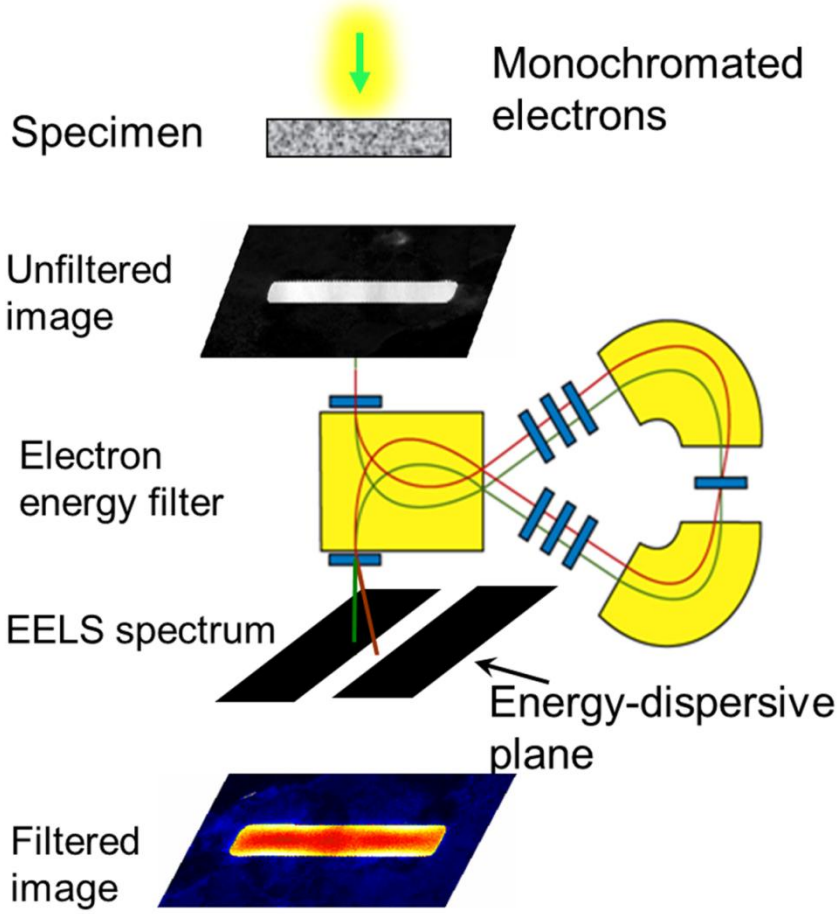

Figure 2.6: The experimental setup of the Zeiss SESAM for conducting EFTEM experiments.

After the energy losses of the fast electrons are measured with the energy filter, an energy filtered image is acquired by using an energy-selecting slit which allows only electrons with specific energy loss to pass. The energy-selecting slit width that has been used throughout the whole experiments was 0.2 eV. Changing the kinetic energy of the fast electrons by increasing the high voltage changes the detected energy loss. This was done in 0.2 eV energy-loss steps, resulting in an EFTEM image series which is displayed as a data cube in figure 2.7. The experimental conditions will be given for every experiment in the following chapters.

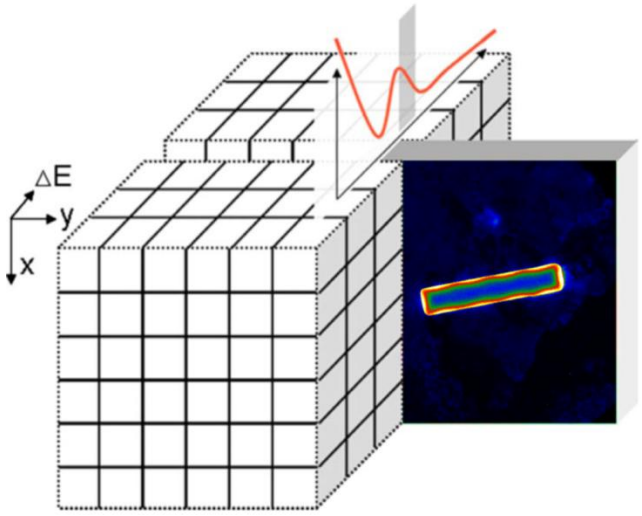

Figure 2.7: The data cube that is obtained from EFTEM experiments.[20]

This thesis contains EFTEM images only for the study of the plasmonic response of the investigated specimen. However, it can also be used for elemental mapping and thickness mapping purposes. The thickness maps of the investigated specimens were acquired using the Zeiss EM 912 Omega microscope by applying the log–ratio method[1].

The log–ratio method is based on the comparison of the areas under the zero-loss peak, I_0, and the total energy-loss spectrum, I_t. The probability that a transmitted electron suffers n collisions is represented by Poisson's statistics[1]

$$P_n = I_n/I_t = (1/n!)(t/\lambda)^n exp(-t/\lambda) \quad (2.5)$$

where n represents the number of scattering events, t is the specimen thickness, and λ is the mean free path describing the mean distance between two inelastic collisions. The highest intensity is measured when $t/\lambda = n$. For the unscattered ($n=0$) component, which is the zero-loss peak, the intensity is the highest at $t = 0$. This value decreases exponentially with specimen thickness and one can rewrite Eq. 2.6 as[1]

$$t/\lambda = ln(I_t/I_0) \quad (2.6)$$

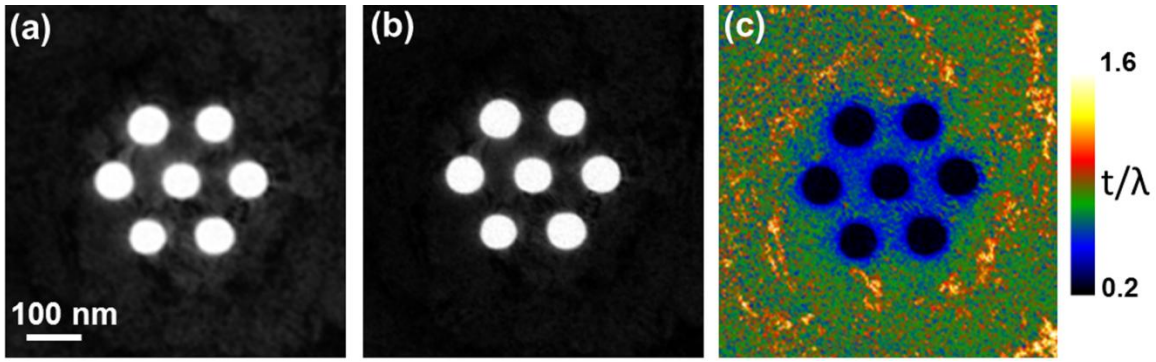

Figure 2.8: (a) an unfiltered image (b) a filtered image, and (c) a t/λ map acquired in order to obtain the thickness of silver film with plasmonic heptamer cavities explained in chapter 5.

The mean free path is dependent on the acceleration voltage of the electrons, size of the objective aperture, and atomic percentage of the elements that the investigated material consists of.[1] An example about the application of the log–ratio method is demonstrated in figure 2.8. The unfiltered (corresponding to I_t) and zero-loss-filtered (corresponding to I_0) images are shown in figures 2.8.a and 2.8.b and the t/λ-map is displayed in figure 2.8.c. By multiplying the t/λ map with the mean free path value one can get a map showing the real thickness values.

EELS measurements were combined with scanning transmission electron microscopy, where one gets an EELS spectrum at every point of the scanned region in 1D or 2D (STEM-EELS spectrum imaging), and EFTEM imaging, which enables to get rapid energy filtered image series, were used in a complementary manner to each other. EFTEM is advantageous compared to EELS spectrum imaging because one can obtain series of energy-filtered images with high spatial sampling over a large imaging region with short acquisition times. The series of images between 0 and 5 eV energy loss using a 0.2 eV wide filter slit takes about 15 min. If the same series of images is acquired by using STEM-EELS, it takes around half an hour depending on time per spectrum/pixel. However, EELS spectrum imaging is more efficient for the investigations of small areas, as more spectral information can be obtained due to better sampling of the energy space.

In the case of EFTEM there are some factors that should be taken into account during the acquisition procedure, which are spatial drift, energy fluctuations, non-isochromaticity, and image distortion. These are very influential and have to be corrected in order to do correct analysis of the acquired images. Spatial drift was the most frequently encountered problem during acquisition. The origin of drift can be instabilities of the microscope or the specimen.

Specimen drift was corrected using a script as described in reference 21 which is based on the cross-correlation of all individual images of the EFTEM series.

Energy fluctuation sometimes occurs due to the high voltage instabilities of the microscope. During the acquisition time of an EFTEM image (often 30 s) the position of the zero-loss fluctuates due to high-voltage instabilities. Therefore, the energy loss values of the energy filtered images have an error of about $\pm$ 0.1 eV.

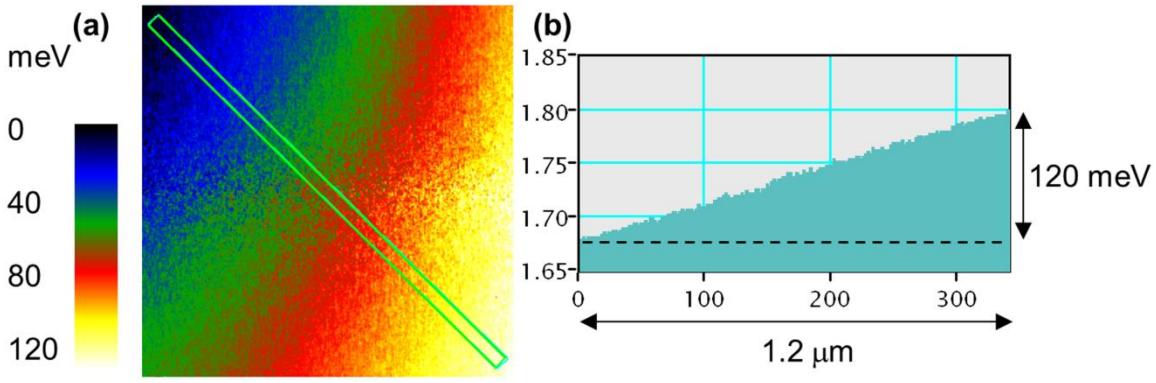

Figure 2.9: The measured non-isochromaticity of the Zeiss SESAM microscope. The profile in (b) has been retrieved from the rectangular region marked in (a).

Non-isochromaticity of the energy filter also influences the EFTEM images. Non-isochromaticity means that due to remaining filter aberrations the selected energy loss is not the same in different parts of the energy-filtered image. This leads to the shift of spectra of off-axis image compared to the spectra of axial image points.[4] Non-isochromaticity can be measured either with specimen or without a specimen. During the measurement without using the specimen, one takes an EFTEM image series of the CCD area across the zero-loss peak, using the smallest filter slit (0.2 eV).[4] By using a large filter entrance aperture (*diameter* = 120 nm) of SESAM, the non-isochromaticity has been measured on the entire 2048 x 2048 pixel CCD camera at a magnification of 20000, an EFTEM image series was acquired in the case shown in figure 2.9. After EFTEM acquisition, a Gaussian fitting is applied on the acquired data cube to determine the position of the zero loss peak in each pixel, and difference between the maximum and the minimum values in the line profile taken from the selected area in resulting map (figure 2.9a) gives the non-isochromaticity value. The measured non-isochromaticity of the Zeiss SESAM is around 10^{-5} eV/nm, as displayed in figure 2.9b. So it does not have an influential effect on the results shown in the present thesis.

Alternatively, in order to measure the non-isochromaticity of MANDOLINE filter, a homogeneous amorphous thin carbon film (PLANO GmbH, Wetzlar) can be used.[12] Since the test specimen has known plasmon energy, and plasmon energy is the same in all parts of the film, the plasmon map gives direct information about the non-isochromaticity of the energy filter.

Finally it should be pointed out that sometimes the electromagnetic field maxima which are expected to be seen on the EFTEM images according to simulations are not visible due to the fact that the background subtraction function fails for the energy-loss region in which the EFTEM experiments were performed. Therefore a new algorithm was developed, the technical details and the examples of which are described in chapters 5, 6, and 9.

EELS and EFTEM are two of the most efficient techniques for plasmon mapping but there are still some points to pay more attention during and after acquisition.[22] The most frequently encountered artefacts are as follows:

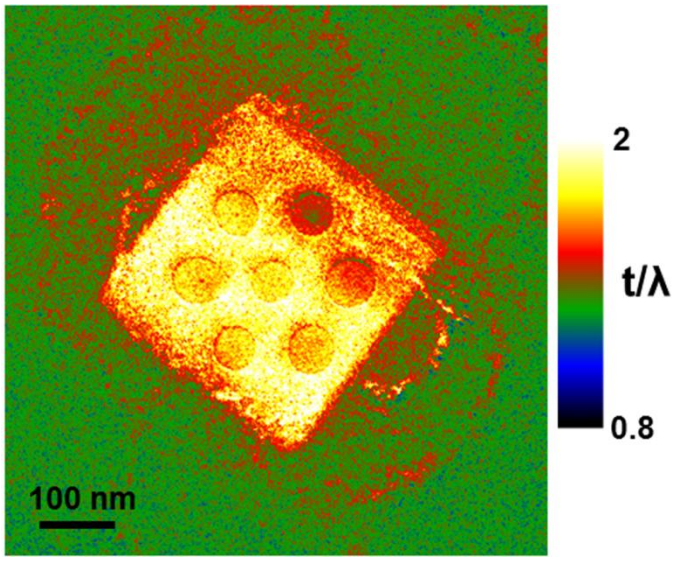

Figure 2.10: A *t*/*λ*-map showing the contamination layer on the heptamer nanocavities drilled into a silver film after a STEM-EELS experiment.

The first problem is contamination, which is caused by hydrocarbons covering the specimen surface. They can be caused by the oil used for pumps, fingerprints, and the surrounding atmosphere. When the electron beam interacts with the specimen, the chemical bonds of the hydrocarbons are broken and they are cross-linked (carbonaceous polymerization).[23]

These cross-linked hydrocarbons form a layer on the specimen, which is visible in figure 2.10. Figure 2.10 shows the situation after contamination of the heptamer holes that were previously shown in figure 2.8. The holes have been totally filled with carbon in addition to the surface contamination of silver film. As the newly formed carbon layer has a different dielectric response function it will cause misinterpretation of the plasmonic eigenmodes. Moreover, this new layer increases the thickness of the specimen in the investigated area leading to unnecessary multiple scattering as the electrons pass through. The contamination layer leads to a shift in the position of the plasmon peaks and a decrease of intensity.

Another effect comes from the zero-loss peak, the tail of which masks the direct observation of the plasmonic eigenmodes in the infrared regime, even in the monochromated. Zeiss SESAM. For example, some low-energy SPR modes could not be observed. An example is shown in Fig. 2.11. HFSS simulations prove that a resonance is supposed to be seen at around 0.6 eV (figure 2.11.b), but the tail of the zero loss peak hinders the observation of this mode completely (figure 2.11.a). Even after background subtraction such a mode could not be observed.

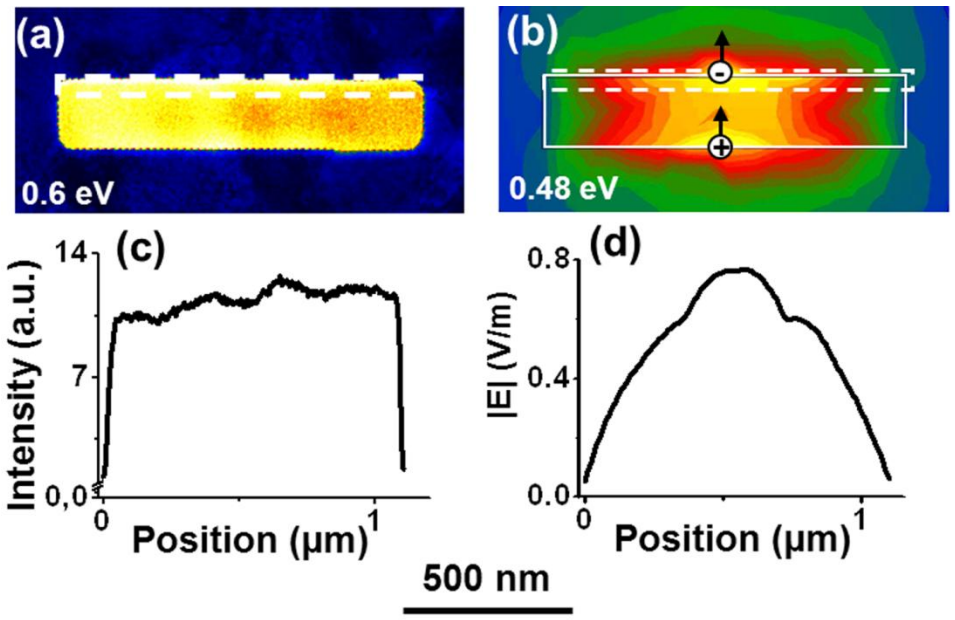

Figure 2.11: (a) An EFTEM image acquired at an energy loss of 0.6 eV. (b) The expected plasmonic eigenmode simulated with HFSS at an energy loss of 0.48 eV. (c) The intensity profile and (d) the *E*-field profile along the regions, as marked in (a) and (b).

2.4. Specimen-Preparation Methods

It is a crucial issue to prepare specimens with smooth surfaces in order to see the plasmonic effect as clear as possible without the influence of artefacts which may damp the plasmonic oscillations.

During this doctorate work the main aim was to prepare free-standing metallic films to eliminate the effects of the substrate. Two different approaches were tried for this purpose. In the first approach, a silver film was produced by physical vapour deposition (PVD). Silver material was sputtered onto a commercially available NaCl window (Korth Kristalle, Kiel, Germany). Although a single crystalline film was desired, the product was polycrystalline due to the fact that the surface of NaCl is not clean enough for this purpose. Despite these facts, NaCl was selected to be the substrate for deposition, because it can be easily detached from the silver film with the least amount of damage as NaCl can be dissolved in water easily. After dissolving the NaCl crystal in distilled water, the remaining polycrystalline silver film was transferred onto a 300 mesh Cu grid. The results of this technique can be seen in chapter 4.

The second approach was using a cold rolled and annealed silver film. Silver discs with 3 mm diameter were punched out and subsequently electropolished in a Struers Tenupol by using the recipe described in reference[24]. A new polish was prepared for each session. Voltage, current, and light sensitivity were set to 4 V, 25 mA, and 100, respectively. Although the reference recommends rinsing the specimens first with anhydrous methyl alcohol and then with CS_2 solution, the second step was skipped as in order to avoid contact with cyanide which is extremely poisonous. As the final step the specimen was ion-milled in a FISCHIONE Instrument (Model 1010) for an hour in total (at 2 kV and 0.5 kV for 30 min each). A double beam was used at a milling angle of 12°. All of the circular and rectangular holes were drilled with a focused ion beam using FEI Nova NANOLAB 60. The results of this preparation technique are displayed in chapters 5, 6, and 7.

Nanoparticles that are analyzed in chapters 8 and 9 were synthesized at two other institutions in China and Spain, respectively.

References

1. Egerton, R.F. *Electron Energy-Loss Spectroscopy in the Electron Microscope*, Springer, 2011.
2. Sigle, W. Analytical Transmission Electron Microscopy, *Annu. Rev. Mater. Sci.* **35**, 239-314, (2005).
3. Koch, C.T.; Sigle, W.; Höschen, R.; Rühle, M.; Essers, E.; Benner, G.; Matijevic, M. SESAM: Exploring the frontiers of electron microscopy, *Microsc. Microanal*. **12**, 506-514, (2006).
4. Essers, E.; Benner, G.; Mandler, T.; Meyer, S.; Mittmann, D.; Schnell, M.; Höschen, R.Energy Resolution of an Omega-Type Monochromator and Imaging Properties of the MANDOLINE Filter *Ultramicroscopy* **110**, 971– 980, (2010).
5. Vogelgesang, R.; Dmitriev, A. Real-space imaging of nanoplasmonic resonances, *Analyst* **135**, 1175-1181 (2010).
6. Williams, D.B.; Carter, C.B. *Transmission Electron Microscopy*, Plenum Press, 1996.
7. Bohr, N. On the constitution of atoms and molecules, part II systems containing only a single nucleus". *Phil. Mag.* **26,** 476–502, (1913).
8. Vesseur, E.J.R.; de Waele, R.; Kuttge, M.; Polman, A. Direct observation of plasmonic modes in Au nanowires using high resolution cathodoluminescence *Nano Lett.* **7**, 2843-2846, (2007).
9. Brydson, R. *Electron Energy Loss Spectroscopy*, BIOS Scientific Publishers Limited, 2001.
10. Garcia de Abajo, F.J. Optical excitations in electron microscopy, *Rev. Mod. Phys.* **82**, 209-275, (2010).
11. Fröhlich, H.; Pelzer, H. Plasma oscillations and energy loss of charged particles in solids, *Proc. Phys. Soc. A*, **68**, 525-529, (1955).
12. Sigle, W.; Krämer, S.; Varshney, V.; Zern, A.; Eigenthaler, U.; Rühle, M. Plasmon energy mapping in energy-filtering transmission electron microscopy, *Ultramicroscopy*, **96**, 565-571, (2003).
13. Gu, L.; Özdöl, V.B.; Sigle, W.; Koch, C.T.; Srot, V.; van Aken, P.A. Correlating the structural, chemical, and optical properties at nanometer resolution, *J. Appl. Phys.*, **107**, 013501, (2010).

14. Potapov, P.L.; Engelmann, H.-J.; Zschech, E.; Stöger-Pollach, M. Measuring the dielectric constant of materials from valence EELS, *Micron*, **40**, 262-268, (2009).
15. Egerton, R.F. Electron energy-loss spectroscopy in the TEM, *Rep. Prog. Phys.*, **72**, 016502, (2009).
16. Stöger-Pollach, M. Optical properties and bandgaps from low loss EELS: Pitfalls and solutions, *Micron*, **39**, 1092-1110, (2008).
17. Mkhoyan, K.A.; Babinec, T.; Maccagnano, S.E.; Kirkland, E.J.; Silcox, J. Separation of bulk and surface losses in low loss EELS measurements in STEM, *Ultramicroscopy*, **107**, 345-355, (2007).
18. Pennycook, S.J.; Nellist, P.D. Scanning Transmission Electron Microscopy, Springer Science+Business Media, 2011, doi: 10.1007/978-1-4419-7200-2_16.
19. Johnson, P.B.; Christy, R.W. Optical constants of the noble metals, *Phys. Rev. B* **6**, 4370-4379, (1972).
20. Nelayah, J.; Gu, L.; Sigle, W.; Koch, C.T.; Pastoriza-Santos, I.; Liz-Marzan, L.M.; van Aken, P.A. Direct imaging of surface plasmon resonances on single triangular silver nanoprisms at optical wavelength using low loss EFTEM imaging, *Opt. Lett.* **34**, 1003-1005, (2009).
21. Schaffer, B.; Grogger, W.; Kothleitner, G. Automated Spatial Drift Correction for EFTEM image series, *Ultramicroscopy* **102**, 27-36, (2004).
22. Schaffer, B.; Kothleitner, G.; Grogger, W. EFTEM spectrum imaging at high-energy resolution, *Ultramicroscopy* **106**, 1129-1138, (2006).
23. Fuchs, E.; Oppolzer, H.; Rehme, H. *Particle Beam Microanalysis*, VCH Verlagsgesellschaft, 1990.
24. Lyles, R. L., Jr.; Rothman, S. J.; Jäger, W. A cyanide free solution for electropolishing silver, *Metallography*, **11**, 361– 363, (1978).

CHAPTER 3

Simulation Methods

3.1. Discrete Dipole Approximation Code (DDSCAT)

Understanding the electromagnetic nature of the observed plasmonic eigenmodes has become an essential issue, especially after the discovery of new plasmonic phenomena within this decade. In this context, simulations based on different methods are offering the possibility to analyze the electromagnetic field concentrations and the coupling behaviour in three dimensions. Discrete dipole approximation (DDA) is one of these techniques, which is used for calculating the electromagnetic scattering and absorption properties of the structures by approximating them as a matrix of "*N*" dipoles with separation "*d*". Then the total volume becomes[1]:

$$V = Nd^3 \tag{3.1}$$

The effective radius of a sphere with the identical volume is calculated as[1]:

$$a_{eff} = (3V/4\pi)^{1/3} \tag{3.2}$$

After defining these values, DDSCAT calculates the absorption efficiency factor (Q_{abs}), the scattering efficiency factor (Q_{sca}), the extinction efficiency factor (Q_{ext}), and the phase lag efficiency factor (Q_{pha}), as described in equations 3.3 to 3.5 below. C_{abs} represents the absorption cross section, and C_{sca} is the scattering cross section[1].

$$Q_{abs} = C_{abs}/\pi a_{eff}^2 \tag{3.3}$$

$$Q_{sca} = C_{sca}/\pi a_{eff}^2 \tag{3.4}$$

$$Q_{ext} = Q_{sca} + Q_{abs} \tag{3.5}$$

The only limitation for the simulations based on DDA is that the inter-dipolar separation should be smaller than the dimensions of target and wavelength. DDSCAT works efficiently for the simulation of the plasmonic behaviour of small nanoparticles[2], and inverse structures, namely

nanoholes, however only up to a certain size. In chapter 7, the circular nanoholes with diameters ranging between 160–200 nm with aspect ratio (= diameter / thickness of the silver film) of 0.5–0.6 were successfully simulated. The simulation of the rectangular holes having much larger size (400*1040 nm^2) shown in figure 3.1 could not be accomplished with DDSCAT. The simulations applied to a rectangular slit failed mainly due to the following reasons: The huge amount of memory occupied on the computer lead to crash the program, the very long simulation period (up to weeks), because DDSCAT has no adaptive mesh refinement , which is fundamental to identify and calculate hot spot positions clearly. Reduction of the sizes down to 260*100 nm^2, while keeping the ratio of long axis to short axis the same in order to save time, did not help either as it is shown in figure 3.2.

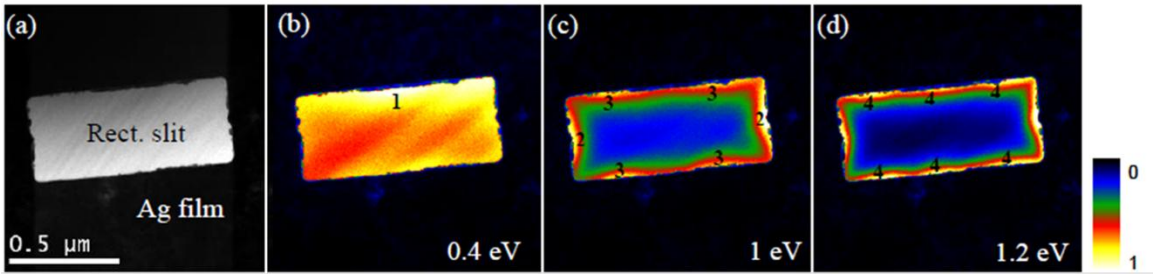

Figure 3.1: Series of images showing (a) the bright-field image, and the energy-filtered images acquired at energy losses of (b) 0.4 eV, (c) 1 eV, and (d) 1.2 eV. Scale bar is valid for all images.[3]

The calculations were repeated for three different thickness values that are 40 nm (N = 107580), 20 nm (N=54090), and 10 nm (N = 27505). The inter-dipolar distance was kept constant ($d = 2\,nm$) in all three cases. The results are displayed in figure 3.2. The simulation setup is displayed in figure 3.2.a. The calculated extinction efficiency factor has maxima at 0.79 eV, 1.05 eV, and 1.18 eV for the different thickness values (10 nm, 20 nm, 40 nm, respectively) as displayed in figure 3.2.b. The corresponding energy values decrease with increasing aspect ratio (fig. 3.2.c). Although the experimental value (red) follows the trend of the calculated data, the energy value is too low compared to the calculated values.

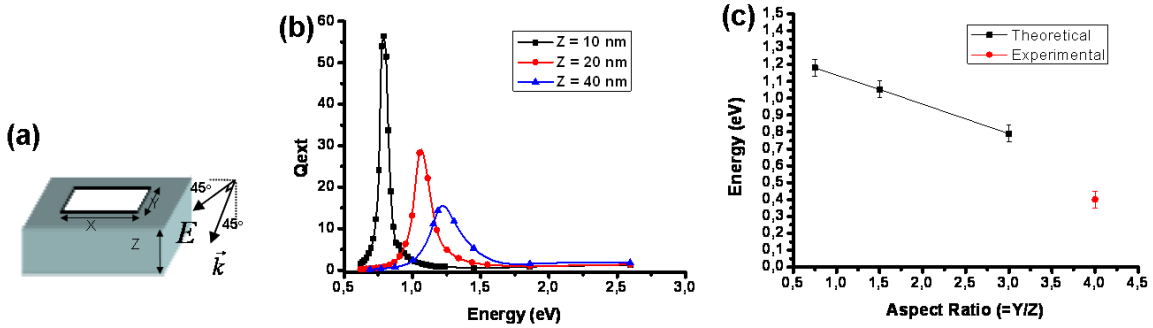

Figure 3.2: (a) The simulation setup showing the polarization direction, (b) Q_{ext} versus energy diagram, and (c) energy versus aspect ratio diagram comparing the simulated and experimental results.[3]

3.2. High Frequency Structure Simulator (HFSS)

HFSS is a commercially available software from ANSOFT Inc., USA, based on FEM.[4] FEM solves the partial differential form of Maxwell's equations in the frequency domain. Equations 3.6 and 3.7 are the Laplace transforms of Maxwell's equations[5]

$$\nabla \times \vec{E} = -\mu(s - s_0)\vec{H} - \mu s_0 \vec{H} \tag{3.6}$$

$$\nabla \times \vec{H} = \varepsilon(s - s_0)\vec{E} + (\varepsilon s_0 + \sigma)\vec{E} \tag{3.7}$$

where s_0 is an arbitrary complex frequency. The problem is defined for a frequency interval $(s - s_o)$, and the calculations are repeated until they converge for these frequency values.

HFSS uses three different solution types for different problems. "Driven modal" solves scattering parameters (s-parameter) based on a model, "Driven terminal" finds voltages and currents in a multi-conductor transmission line and "Eigenmode solver" calculates resonant frequencies and corresponding eigenmodes of a structure. Although HFSS is designed for microwave and radio frequency engineering applications, it works efficiently for the simulations of plasmonic eigenmodes in a rectangular slit investigated at THz frequency region as discussed in detail in chapter 4.

For discretization, the structure is divided into thousands of small cells in the shape of tetrahedra, where the necessary components of the simulated field are deposited at the corners, faces and vertices of each (figure 3.3.a). This shape is quite advantageous in discretization of structures with curves and sharp corners. The area around the discretized system has to be limited with some boundary conditions before starting the calculations. For the simulation of rectangular slits in chapter 4, a spherical impedance boundary was chosen as the boundary condition. The impedance boundary introduces a resistive surface around the system. With the selection of the impedance boundary, the surrounding environment could be limited and set as free space by entering the resistance and reactance values to 376.73 Ω and 0 Ω, respectively. The radius of the sphere was adjusted to be large enough not to affect the results by setting it as a function of the starting frequency value and the size of the long edge of the slit ($radius = 0.5 \times l_{slit} + 0.25 \times 3 \times 10^8/f$). In figure 3.3.b, it is possible to see the borders of the bounding sphere in the shape of a circle surrounding the rectangular slit.

The eigenmode solver was used for simulation of the rectangular slits. The starting frequency value, maximum number of calculation sessions (passes), maximum delta frequency,

and maximum mesh refinement percentage values are entered by the user into the system as calculation parameters before the session starts. At each adaptive pass, a frequency value is defined by the system automatically for each possible eigenmode by solving Maxwell's equations until the maximum adaptive pass number is reached.[4] The calculation routine is as follows: At each divided tetrahedral cell unit a polynomial function is created along the edge (figure 3.3a). Using adaptive mesh refinement, the system automatically modifies the number of tetrahedral units at each pass for each eigenmode up to the maximum mesh refinement percentage value (set as 30% in this case). For a particular eigenmode, a specific frequency value is calculated at each adaptive pass. If the difference among these frequency values determined at every pass for a particular eigenmode is less than the maximum delta frequency (1% in this case), which is the threshold value, it means that the calculation has converged and the simulation stops for this eigenmode simulation session.[4]

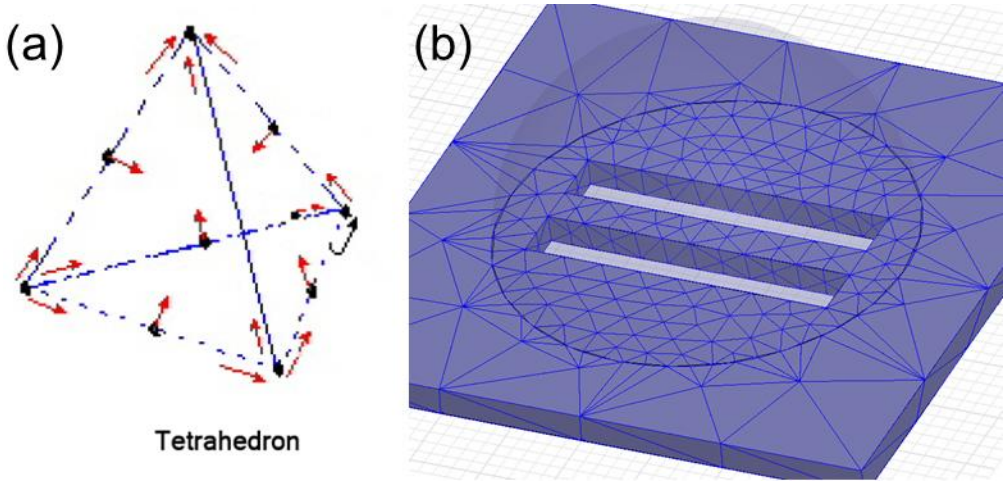

Figure 3.3: (a) The tetragonal unit cell in order to discretize a structure, and (b) a discretized double rectangular slit system that will be discussed in the proceeding chapters.[4]

3.3. Three-Dimensional Finite-Difference Time-Domain Simulations (3D-FDTD)

3D-FDTD simulations are based on solving the partial differential forms of Maxwell's equations as function of time which are denoted in equations 3.8 and 3.9 as follows:[6]

$$\frac{\partial H}{\partial t} = -\frac{1}{\mu}\nabla \times E - \frac{\rho'}{\mu}H \tag{3.8}$$

$$\frac{\partial E}{\partial t} = \frac{1}{\varepsilon}\nabla \times H - \frac{\sigma}{\varepsilon}E \tag{3.9},$$

where E is the electric field, H is the magnetic field, ε is the electrical permittivity, σ is the electrical conductivity, and μ is the magnetic permeabilitiy. ρ' represents an equivalent magnetic resistivity, which is necessary so that magnetic loss mechanisms can be taken into account. This can be calculated from the magnetic current annotated as;

$$J_m = \rho' H \tag{3.10}$$

FDTD uses a rectangular coordinate system where Maxwell's equations are defined in three dimensions through equations 3.11 to 3.16;[7]

$$\frac{\partial H_x}{\partial t} = \frac{1}{\mu}\left(\frac{\partial E_y}{\partial z} - \frac{\partial E_z}{\partial y} - \rho' H_x\right) \tag{3.11}$$

$$\frac{\partial H_y}{\partial t} = \frac{1}{\mu}\left(\frac{\partial E_z}{\partial x} - \frac{\partial E_x}{\partial z} - \rho' H_y\right) \tag{3.12}$$

$$\frac{\partial H_z}{\partial t} = \frac{1}{\mu}\left(\frac{\partial E_x}{\partial y} - \frac{\partial E_y}{\partial x} - \rho' H_z\right) \tag{3.13}$$

$$\frac{\partial E_x}{\partial t} = \frac{1}{\varepsilon}\left(\frac{\partial H_z}{\partial y} - \frac{\partial H_y}{\partial z} - \sigma E_x\right) \tag{3.14}$$

$$\frac{\partial E_y}{\partial t} = \frac{1}{\varepsilon}\left(\frac{\partial H_x}{\partial z} - \frac{\partial H_z}{\partial x} - \sigma E_y\right) \tag{3.15}$$

$$\frac{\partial E_z}{\partial t} = \frac{1}{\varepsilon}\left(\frac{\partial H_y}{\partial x} - \frac{\partial H_x}{\partial y} - \sigma E_z\right) \tag{3.16}$$

These equations make up the unit cell of Yee's mesh, which is used in order to discretize the structure (figure 3.4).

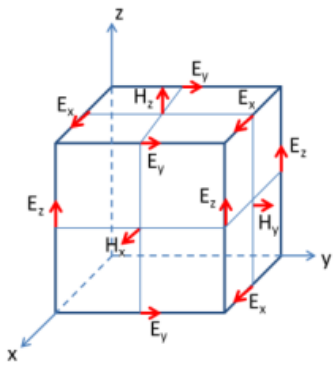

Figure 3.4: A unit cell of the Yee's mesh which show the electric and magnetic field in three dimensions.

A boundary condition is necessary for FDTD simulations to limit the simulated region. A perfectly matched layer (PML) was exploited to avoid reflections from the boundaries for the FDTD simulations conducted for the cases in this thesis (chapters 5, 6, 8, and 9). With the selection of PML, a non-physical medium that splits the magnetic and electric fields in the boundary conditions has been created.[8] An excitation source is assumed to enter into this space and the calculations are performed in time steps. These calculations go on until the steady-state condition is approached. Different excitation sources can be used during calculations such as a wide-band source, harmonic waves, or a focused beam. In chapters 5, 6, 8, and 9 applications of Huygens' source were used. Huygens source was applied in order to imitate the excitation with an electron beam. At the application of a Huygens source a plane wave source is used. A secondary wave having a spherical shape is created by each point on a wavefront during illumination. The amplitudes of the spherical waves sum up incoherently giving the total amplitude at the observation plane. The direction of propagation is always forward, there is no backward propagation.[9] The FDTD simulation codes that are used to simulate the structures in this thesis have been written by Nahid Talebi.

References

1. Draine, B.T.; Flatau, P:J: User Guide for the Discrete Dipole Approximation Code DDSCAT 7.0, http://arxiv.org/abs/0809.0337v4, 2008.
2. Nelayah, J.; Kociak, M.; Stephan, O.; Geuquet, N.; Henrard, L.; Garcia de Abajo, F.J.; Pastoriza-Santos, I.; Liz-Marzan, M.; Colliex, C. Two dimensional quasitatic stationary short range surface plasmons in flat nanoprisms, Nano Lett. **10**, 902-907 (2010).
3. Ögüt, B.; Sigle, W.; Koch, C.T.; van Aken, P.A. Study of surface plasmon resonances on rectangular slits in thin Ag films by low-loss EFTEM imaging, MATEMATERIALS IV, 2010, Karlsruhe, Germany.
4. Training Manual An Introduction to HFSS 12.1, ANSYS, Inventory Number: 002843, 2010.
5. Bracken, J.E.; Sun, D.-K.; Cendes, Z. Characterization of electromagnetic devices via reduced order models, *Comput. Methods Appl. Mech. Engrg.* **169**, 311-330, (1999).
6. Taflove, A. Review of the formulation and applications of the finite-difference time-domain method for numerical modeling of electromagnetic wave interactions with arbitrary structures, *Wave Motion*, **10**, 547-582, (1988).
7. Taflove, A.; Hagness, S.C. Computational electrodynamics the finite-difference time-domain method, Artech House, 2005.
8. Fu, Y.; Qiu, M. *Optical properties of nano structures*, Pan Stanford Publishing Pte. Ltd., 2011.
9. Wang, Z.L. *Elastic and inelastic scattering in electron diffraction and imaging*, Plenum Press, 1995.

CHAPTER 4

Hybridized Metal Slit Eigenmodes as an Illustration of Babinet's Principle

Burcu Ögüt[1], Ralf Vogelgesang[2], Wilfried Sigle[1], Nahid Talebi[1,3], Christoph T. Koch[1], and Peter A. van Aken[1]

1. Max Planck Institute for Intelligent Systems, Heisenbergstraße 3, 70569, Stuttgart, Germany
2. Max Planck Institute for Solid State Research, Heisenbergstraße 1, 70569, Stuttgart, Germany
3. Photonics Research Laboratory, Center of Excellence for Applied Electromagnetic Systems, School of Electrical and Computer Engineering, North Kargar Avenue, Tehran, Iran

This chapter contains comprehensive research about the surface plasmon behaviour of single rectangular slits as well as the electromagnetic coupling between two rectangular slits brought into close interaction with each other. EFTEM measurements and HFSS simulations have been performed by Burcu Ögüt. Wilfried Sigle has helped with solving problems during the experimental stage. Christoph T. Koch has written the algorithm that was used for EFTEM acquisition. All of the co-authors have contributed to the interpretation of experimental and simulation results.

Hybridized Metal Slit Eigenmodes as an Illustration of Babinet's Principle

Burcu Ögüt,[†,*] Ralf Vogelgesang,[‡] Wilfried Sigle,[†] Nahid Talebi,[†,§] Christoph T. Koch,[†] and Peter A. van Aken[†]

[†]Max Planck Institute for Intelligent Systems, Heisenbergstrasse 3, 70569 Stuttgart, Germany, [‡]Max Planck Institute for Solid State Research, Heisenbergstrasse 1, 70569 Stuttgart, Germany, and [§]Photonics Research Laboratory, Center of Excellence for Applied Electromagnetic Systems, School of Electrical and Computer Engineering, University of Tehran, North Kargar Avenue, Tehran, Iran

ABSTRACT By energy-filtering transmission electron microscopy (EFTEM), we observe Fabry-Pérot-like surface plasmon resonances (SPRs) along the length of rectangular single and double slits drilled into free-standing thin silver films. These eigenmodes hybridize in closely situated slits. The nature of their lateral coupling is uncovered from finite-element simulations, which show that the symmetry and energy sequence of hybrid modes is governed by Babinet complementarity principles. Interestingly, the modes of a double slit system, being proto-self-complementary, may alternatively be explained by magnetic interactions between slit fields or by electrostatic interactions across the metallic bridge separating the slits.

KEYWORDS: surface plasmon resonances · energy-filtering transmission electron microscopy · finite-element method · Babinet's principle · silver rectangular slits

The rising demand of nanoscale electronic and photonic applications[1,2] has been an impetus for plasmonics to become an emerging field of nanotechnology over the past decade, especially attracting attention in the fields of cancer diagnostics[3] and therapy,[4] surface-enhanced Raman spectroscopy,[5] optical circuitry,[6] and plasmonic computer systems.[7] Since the pioneering studies of Pines and Bohm[8] and Ritchie,[9] it has been known that some part of the energy losses of electrons passing through thin films is due to plasmon excitations, which are coherent collective oscillations of the electron liquid in a conductor intertwined with associated electromagnetic fields. Surface plasmons (SPs) are waves propagating along a metal/dielectric interface, whereas surface plasmon resonances (SPRs) are the corresponding eigenmodes in confined systems.[10] The SPR energy and optical properties, such as scattering and absorption, can be tuned by modifying the geometry.

Surface plasmons[11] can be excited if fast electrons pass a dielectric medium in a transmission electron microscope (TEM)—as first demonstrated in 1982 by Batson.[12] Most importantly, the investigation by fast electrons offers very high spatial resolution in the range of a few nanometers, which is presently not easily achieved with light optical techniques.[13] Not until recently has it become possible to image localized surface plasmon resonances (LSPRs) in the entire wavelength range from far-infrared up to the ultraviolet.[14] In particular, the far-infrared regime has become more readily accessible by the introduction of narrow band-pass electron monochromators. In the work presented here, we make use of an imaging energy filter that allows us to directly acquire images at selected energy losses corresponding to LSPRs. So far, this method has been applied on nanotriangles,[15−17] nanorods,[18] and arrangements of circular nanoholes[19,20] to directly map their plasmonic eigenmodes. Here we apply it to rectangular nanoslits. The advantages of this geometry are (i) that the object is free-standing so that substrate effects do not have to be considered in the analysis and (ii) that the very fine spatial sampling allows wavenumbers of SP modes to be measured directly from the as-acquired raw experimental images.

The main emphasis of this article is how electromagnetic coupling affects the LSPR energies in a slit system. It is well-known that surface plasmon coupling effects can be mediated by both the electric and magnetic field components.[21] Figure 1a(i) shows the charge distribution of a LSPR of a single thin metallic rod with negative real part, ε_1, of the dielectric function. Owing to the negative sign of ε_1 (which is typical for metals in the optical wavelength range), the low-energy mode has the same charges on both sides of the rod. The situation is quite similar in the case of surface plasmons on a thin film.[22] If the film thickness is of similar magnitude as the skin depth, the electric field components on both surfaces interact, leading to the well-known (low-energy) symmetric and (high-energy) antisymmetric surface modes. Magnetic field

* Address correspondence to ogut@is.mpg.de.

Received for review June 17, 2011 and accepted July 15, 2011.

Published online July 15, 2011
10.1021/nn2022414

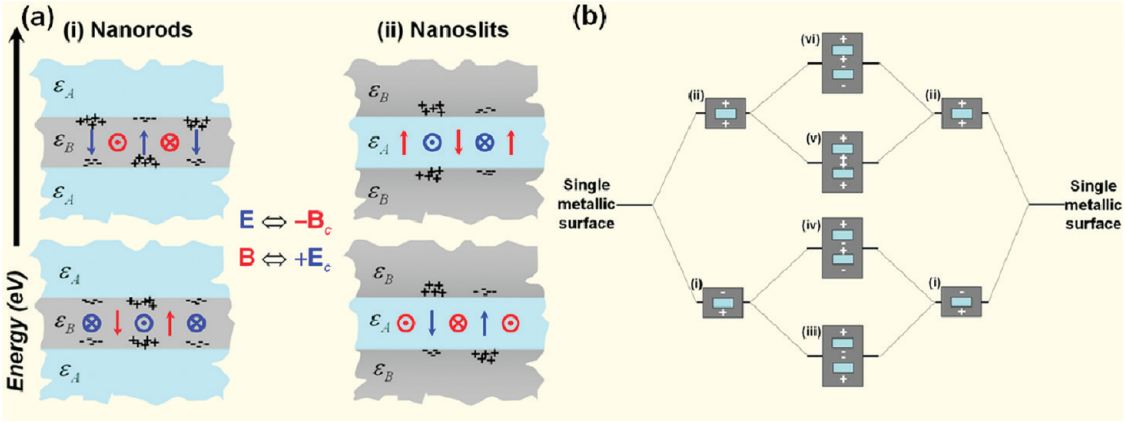

Figure 1. (a) Babinet principle, relating the fields diffracted (or scattered) by (i) nanorods and by (ii) complementary nanoslits. Schematically illustrated here are selected field components in a plane on the "shadow" side close by but not coinciding with the object plane. Blue and red colors indicate electric and magnetic fields, respectively. (b) Expected plasmon hybridization scheme for metallic slits.

components are relatively weak in the case of rods, which explains why the interaction of closely spaced rods can be described in a quasi-static electric picture.[23,24]

If we now look at the complementary system, namely, a slit in a metal film (Figure 1a(ii)), opposite charges on both sides have minimum energy because the medium between the charges is air (or vacuum) with $\varepsilon_1 > 0$. It is obvious that in Figure 1a(ii) there is now a strong magnetic moment in the slit center pointing into and out of the image plane. Therefore, the role of magnetic fields in coupled slits can be expected to be strong. This may also be regarded as a direct consequence of Babinet's principle[25−27] which states that the role of electrical and magnetic fields is interchanged in complementary systems.[21]

The electromagnetic coupling possibilities of two metallic surfaces can be analyzed with a scheme in Figure 1b based on plasmon hybridization theory.[28] As two independent silver surfaces approach each other forming a rectangular slit, the primarily observed electromagnetic surface modes will blend and the antisymmetric (mode i) and symmetric (mode ii) charge distributions will be observed at lower and higher energies, respectively, in agreement with Figure 1a(ii). Two single slits that have antisymmetric charge distributions hybridize in two different manners. The low-energy and high-energy modes are expected to have the charge distributions of $+ - - +$ and $+ - + -$, respectively (modes iii and iv). Hybridization of two single slits with symmetric charge distribution is supposed to form two modes with charge distribution of $+ + + +$ at lower energy and $+ + - -$ at higher energy, respectively (modes v and vi). In principle, symmetric and antisymmetric single slit modes (modes i and ii in Figure 1b) might hybridize, but as their energies are usually far away from each other, hybridization of these two modes with different symmetry configurations is not energetically feasible in practice.[29] We will come back to these considerations about Babinet's principle and plasmon hybridization while discussing the experimental results.

RESULTS AND DISCUSSION

We first discuss results for single slits. In Figures 2 and 3, selected images from the EFTEM series and the corresponding results obtained from the high-frequency structure simulator (HFSS 12) simulations are displayed. Energy-loss probability in the EFTEM images and electrical field magnitude in the simulation results are color-coded in such a way that they increase from blue to yellow color (see color bars). From the electric field divergence extracted from Figures 2c and 3b, we deduce the distribution of charges for the different eigenmodes around the single and double slit configuration; "+" and "−" signs are used in Figures 2 and 3 to mark the central position of the charges.

Pronounced intensity maxima are visible along the long (y) direction in both the experimental EFTEM images and the simulated electric field magnitudes. We start the discussion for the case of the single slit. The experimental data (Figure 2a,b) exhibit maxima at the top and bottom edges of the slit. Their separation is, within the experimental error, equidistant for a given energy loss (or wavelength). The intensity profiles in Figure 2b prove that the number of maxima are two at 1 eV (1.24 μm), three at 1.4 eV (0.89 μm), and four at 1.8 eV (0.69 μm), substantiated with the line profile of the electric field distributions in Figure 2d, as well. (Note that the mode exhibiting only one maximum could not be detected because of its low eigenenergy, which was screened by the tail of the zero-loss peak.) In the following, we denote these modes as α, β, and δ. The electric field distributions obtained from the simulations show the same shape as the experimental data. Figure 2c shows that at 1 eV (1.24 μm), 1.19 eV (1.04 μm), and 1.62 eV (0.76 μm) the electric field vectors oscillate in phase (symmetric) along the x direction, corresponding

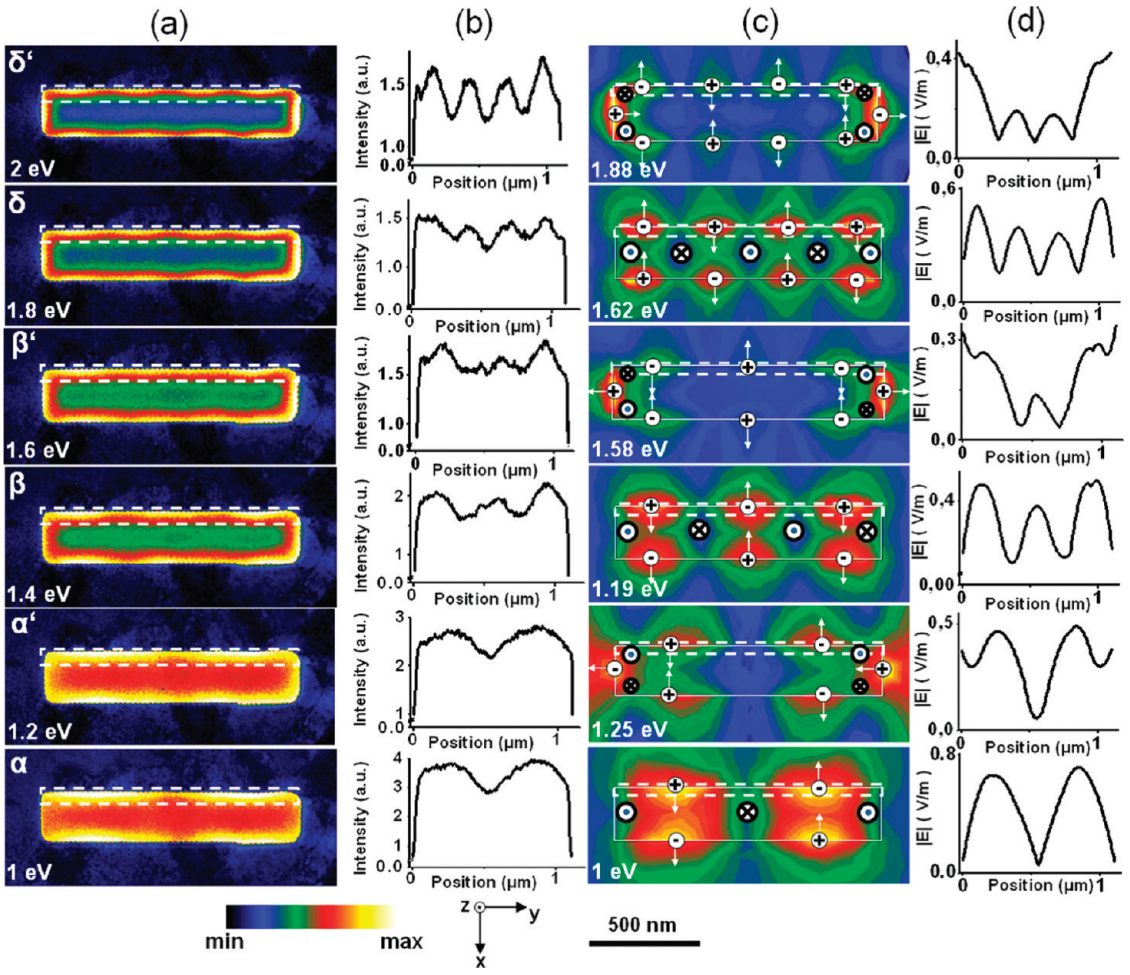

Figure 2. (a) Experimental EFTEM images acquired at the energy-loss range of 1−2 eV; (b) intensity profiles along the regions marked in the EFTEM images; (c) calculated electric field strength |E| vectors (black arrows), charge distributions and magnetic field vectors (pointing into and out of the page assigned by ⊗ and ⊙, respectively) at resonance energies (wavelengths) of 1 eV (1.24 μm), 1.25 eV (0.99 μm), 1.19 eV (1.04 μm), 1.58 eV (0.78 μm), 1.62 eV (0.76 μm), and 1.88 eV (0.66 μm); and (d) calculated electric field profiles along the regions marked in the simulated images for the single slit. The scale bar is also valid for both (a) and (c).

to the accumulation of opposite electrical charges on both sides of the long slit walls, thereby giving rise to a dipolar, capacitor-like behavior.[30] The modes, designated as α', β', and δ' at 1.25 eV (0.99 μm), 1.58 eV (0.78 μm), and 1.88 eV (0.66 μm), respectively, reveal that the same charge distribution is observed along the long slit walls as for the mode α, β, and δ, but that the electric field vectors are oscillating out of phase. These modes are not so visible in the experimental results, due to the fact that these modes are weak. In addition, the experimental energy resolution is limited to 0.2 eV.

We now consider the case of two closely spaced slits (Figure 3a,b). From the experimental data (Figure 3a), we see that the field distribution is not the same along the outer and inner long slit walls, contrary to the case for the single slits—a first indication of strong interaction of the electromagnetic fields of the two slits leading to mode hybridization. Calculated field distributions (Figure 3b) confirm that the equal charges associated with the symmetric electrical field vectors add coherently and cause an electrical field enhancement at the connecting bridge at 0.95 eV (1.29 μm) (mode α*), 1.15 eV (1.08 μm) (mode β*), and 1.58 eV (0.79 μm) (mode δ*). In contrast, at 1.04 eV (1.19 μm) (mode α**), 1.27 eV (0.98 μm) (mode β**), and 1.82 eV (0.68 μm) (mode δ**), the electric field at the bridge is rather weak, in accordance with a cancellation of opposite charges. The electromagnetic field is therefore concentrated along the outer edges of the slits.

Apart from the intriguing contributions of eigenmodes leading to Fabry-Pérot-like standing wave patterns along the length of the nanoslits, notable symmetries emerge in the field patterns across, associated with Babinet complementarity. Whereas a single slit is the unmistakable Babinet complement of a single rod, an infinite number of equally spaced slits/rods (*i.e.*, a grating) forms a self-complementary system. The double slits studied here exhibit features of both extremes because the bridge separating the two slits may also be viewed as a rod, introducing an element of

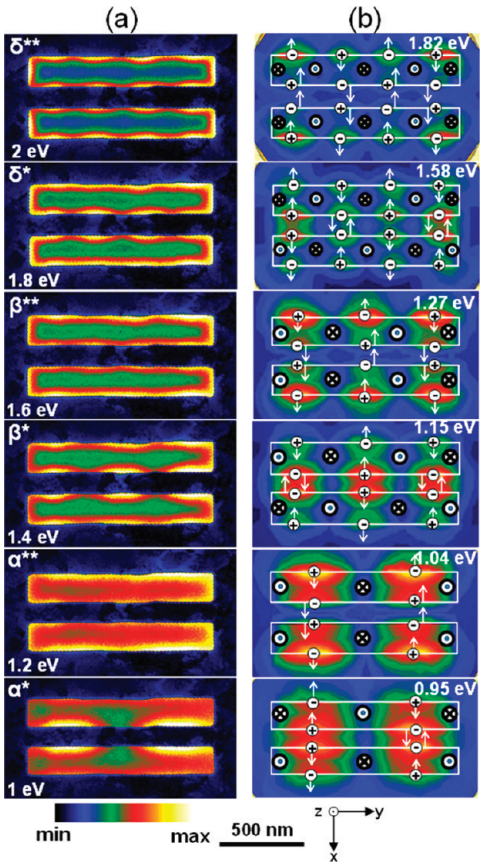

Figure 3. (a) Experimental EFTEM images acquired at energy losses of 1, 1.2, 1.4, 1.6, 1.8, and 2 eV and (b) calculated electric field strength |E|, vectors (black arrows), charge distributions and magnetic field vectors (pointing into and out of the page assigned by ⊗ and ⊙, respectively) at resonance energies (wavelengths) 0.95 eV (1.29 μm), 1.04 eV (1.19 μm), 1.15 eV (1.08 μm), 1.27 eV (0.98 μm), 1.58 eV (0.79 μm), and 1.82 eV (0.68 μm) for the double slit. The scale bar in (a) is also valid for (b).

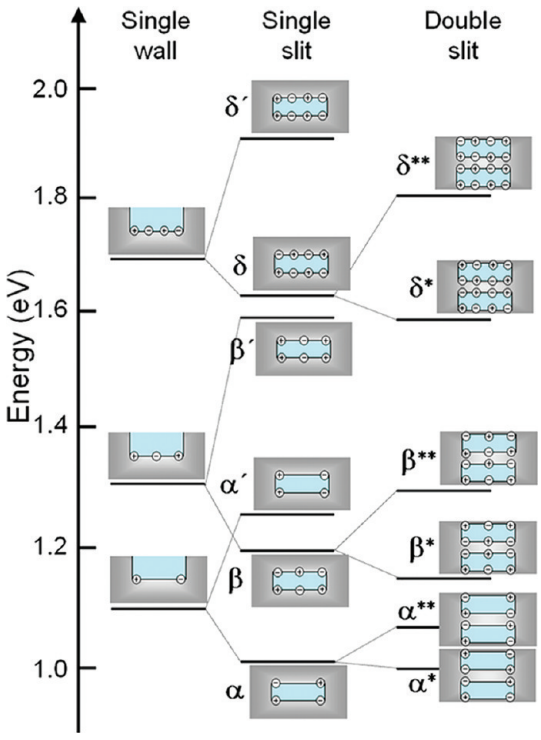

Figure 4. Energy-level diagram of the plasmon resonance modes found in the finite-element simulations for the single and double slits.

self-complementarity. It should as well be noted that Babinet's principle is strictly correct only for infinitely thin films that are perfectly conducting and flat. In real-life situations, the validity of Babinet's principle is approximate.[31] For slits in metal screens, this leads to the possibility of propagating SPs on the film surface, which may couple to and modify the spectral behavior of the LSPRs at the holes. Geometrically, the LSPRs experience effective width and length increases. For slits, this is due to the penetration of the fields into the surrounding metal, in rods due to the complementary penetration into the surrounding dielectric.[32,33]

The low-energy mode α^* has the same charges across the bridge (and opposite charges across the slits), whereas the high-energy mode α^{**} has opposite charges across both the bridge and the slits. If we consider the bridge as a rod-like structure, this is easily understood from Figure 1a. The energetic sequence of the α^* and α^{**} modes can also be shown by looking at the magnetic moments that are schematically shown for the six double slit modes in Figure 3. For the low-energy modes, there are six magnetic moments, and for the high-energy modes, there are 10 magnetic moments. Evidently, in the case of the modes α^*, β^*, and δ^*, the next-nearest magnetic moments have opposite sign and are therefore attractive. For modes α^{**}, β^{**}, and δ^{**}, the magnetic moments on both sides of the bridge are parallel, that is, repulsive. Thus, the double nanoslit system is in perfect Babinet complementarity to the conventional hybridization of direct (double nanorod) plasmonic structures.[28]

Figure 4 exquisitely recapitulates the electromagnetic coupling relations for our structures. HFSS simulations (not shown) validate the existence of two, three, and four E-field maxima at 1.1 eV (1.13 μm), 1.32 eV (0.94 μm), and 1.71 eV (0.73 μm), respectively, on the 1107 nm long single silver surface. The charge distributions and the energies observed for the expected lower and high-energy modes for single and double slits are all in agreement with Babinet's principle and plasmon hybridization theory, except the situation that the expected high-energy modes of double slits with charge distributions $++++$ and $++--$, designated as mode v and vi in Figure 1b, have been observed in neither the experiments nor the simulations.

CONCLUSIONS

EFTEM imaging allows hyperspectral imaging of eigenmodes in plasmonic nanostructures with exquisite spatial resolution in the nanometer range and short acquisition times. Here we apply EFTEM imaging

to SP eigenmodes in single and coupled nanoslits in a thin Ag film. We find close correspondence of experimental data with FEM simulations. We interpret the plasmonic modes as Fabry-Pérot-like SP interferences along the length of the slits. The transverse interactions are interpreted by considerations of Babinet complementarity. We find evidence for magnetic coupling between closely spaced slits ordering the energetic sequence of hybridized modes and note that the very same conclusions also follow from complementary considerations of electric coupling across the rod-like bridge separating the slits. The present results suggest new opportunities to tune resonances and electromagnetic coupling by considering not only the geometry of direct metallic nanostructures but also their Babinet complements.

MATERIALS AND METHODS

Specimen Preparation. A 100 nm thick silver film was deposited on a NaCl crystal (optically polished, Korth Kristalle GmbH, Kiel, Germany, Art. No. 10 40 106) by physical vapor deposition at 200 °C. Subsequently, the silver film was removed from the NaCl crystal by dissolving the substrate in distilled water and then transferring the film to a standard TEM 300 mesh Cu grid. On the grid, the Ag film is free-standing, which is advantageous for the interpretation of the measurements since effects due to the presence of a substrate do not occur. A rectangular single slit (210 nm × 1107 nm) and double slits (180 nm × 1070 nm) with 130 nm slit separation were drilled into the film by a focused ion beam (FIB) (FEI Nova Nano Lab). The thickness of the Ag film has been measured by a log-ratio method based on the comparison of the areas under the zero-loss peak, and the whole total area in an acquired EELS spectrum.[34]

Experimental Method. The experiments were carried out at the sub-electronvolt sub-angstrom microscope (SESAM) (Zeiss, Oberkochen, Germany) operated at 200 kV.[35,36] The SESAM is equipped with a field-emission gun, a symmetric electrostatic Omega-type electron monochromator,[37] and an in-column MANDOLINE filter.[38] The advantages of this combination of electron optical components are a high dispersion of the energy filter of about 6 μm/eV, an energy resolution better than 100 meV, and small non-isochromaticity of only 0.1 meV/nm.[36] The very high dispersion is important to obtain images from very narrow energy-loss ranges; an energy resolution better than 0.2 eV is mandatory especially for the infrared range of the spectrum because of the overlap of spectral features with the elastic zero-loss peak, and the excellent isochromaticity guarantees simple image interpretation over large fields of view. The perforated Ag thin films were investigated with the energy-filtering transmission electron microscopy (EFTEM) imaging technique. Both the monochromator slit and the energy-selecting slit in the energy filter had a width of 0.2 eV. A series of energy-filtered images were recorded in the energy-loss range from 0.4 to 5.0 eV using a step size of 0.2 eV. The images were recorded on a 2k × 2k CCD camera (Ultrascan, Gatan, USA) applying a binning of 4. Because of the variation of electron intensity in different energy-loss ranges, the acquisition time was automatically adjusted for each image. However, the acquisition time was not allowed to exceed 30 s in order to make specimen drift artifacts negligible. In order to eliminate camera artifacts due to scintillator afterglow, we started the image series at an energy loss of 5 eV, where the image intensity is lowest and recorded new dark-reference images after each energy-filtered image. All of the data have been processed using Gatan Digital Micrograph. The specimen drift in the image series was corrected by using a script described elsewhere.[39]

Eigenmode Simulations. In order to calculate the plasmonic eigenmodes of the rectangular slits in the Ag film, we used commercially available software (high-frequency structure simulator, HFSS 12, Ansoft, Inc., USA). This is based on the finite-element method (FEM) to solve Maxwell's equations using an adaptive mesh refinement with tetrahedral mesh units.[40–42]

Rectangular single and double slits (with the same dimensions as in the experiment) in a 100 nm thick silver film (2 μm × 2 μm) were simulated with this method. For the double slit, the distance between the two rectangles was 130 nm. The HFSS eigenmode solver was used to perform the calculations, where a spherical impedance boundary confined the volume around the rectangular hole. The radius of the sphere was chosen large enough not to affect the results of the simulation. We used the optical constants for silver reported in the literature.[43] The (real valued) relative electric permittivity and conductivity were then obtained, respectively, from the relations $\varepsilon_r = n^2 - k^2$ and $\sigma = \omega\varepsilon_0 2nk$, where ω is the angular frequency, n the index of refraction, and k the absorption constant.

Acknowledgment. We thank J. Dorfmüller for helpful discussions, U. Eigenthaler and I. Lakemeyer for specimen preparation, M. Laudien for the support with HFSS simulations. This research has been supported by the European Union under the Framework 6 program under a contract for an Integrated Infrastructure Initiative, Reference 026019 (ESTEEM).

REFERENCES AND NOTES

1. Gramotnev, D. K.; Bozhevolnyi, S.I. N. Plasmonics beyond the Diffraction Limit. *Nat. Photonics* **2010**, *4*, 83–91.
2. Luther, J. M.; Jain, P. K.; Ewers, T.; Alivisatos, A. P. Localized Surface Plasmon Resonances Arising from Free Carriers in Doped Quantum Dots. *Nat. Mater.* **2011**, *10*, 361–366.
3. El-Sayed, I. H.; Huang, X.; El-Sayed, M. A. Surface Plasmon Resonance Scattering and Absorption of Anti-EGFR Antibody Conjugated Gold Nanoparticles in Cancer Diagnostics: Applications in Oral Cancer. *Nano Lett.* **2005**, *5*, 829–834.
4. Lal, S.; Clare, S. E.; Halas, N. J. Nanoshell-Enabled Photothermal Cancer Therapy: Impending Clinical Impact. *Acc. Chem. Res.* **2008**, *41*, 1842–1851.
5. Kneipp, K.; Wang, Y.; Kneipp, H.; Perelmann, L. T.; Itzkani, I.; Dasari, R. R.; Feld, M. Single Molecule Detection Using Surface-Enhanced Raman Scattering. *Phys. Rev. Lett.* **1997**, *78*, 1667–1670.
6. Brongersma, M. L.; Zia, R.; Schuller, J. A. Plasmonics—The Missing Link between Nanoelectronics and Microphotonics. *Appl. Phys. A: Mater. Sci. Process.* **2007**, *89*, 221–223.
7. Zia, R.; Schuller, J. A.; Chandran, A.; Brongersma, M. L. Plasmonics—-The Wave of Chip Scale Device Technologies. *Mater. Today* **2006**, *9*, 20–27.
8. Pines, D.; Bohm, D. A Collective Description of Electron Interactions: II. Collective *vs* Individual Particle Aspects of the Interactions. *Phys. Rev.* **1952**, *85*, 338–353.
9. Ritchie, R. H. Plasma Losses by Fast Electrons in Thin Films. *Phys. Rev.* **1957**, *106*, 874–881.
10. Raether, H. *Surface Plasmons on Smooth and Rough Surfaces and on Gratings*; Springer-Verlag: Berlin, Heidelberg, 1988; pp 4−37.
11. Ebbesen, T. W.; Lezec, H. J.; Ghaemi, H. F.; Thio, T.; Wolff, P. A. Extraordinary Optical Transmission through Sub-wavelength Hole Arrays. *Nature* **1998**, *391*, 667–669.
12. Batson, P. E. Surface Plasmon Coupling in Clusters of Small Spheres. *Phys. Rev. Lett.* **1982**, *49*, 936–940.
13. Vogelgesang, R.; Dmitriev, A. Real-Space Imaging of Nanoplasmonic Resonances. *Analyst* **2010**, *135*, 1175–1181.
14. Nelayah, J.; Kociak, M.; Stephan, O.; Garcia de Abajo, F. J.; Tence, M.; Henrard, L.; Taverna, D.; Pastoriza-Santos, I.;

Liz-Marzan, L. M.; Colliex, C. Mapping Surface Plasmons on a Single Metallic Nanoparticle. *Nat. Phys.* **2007**, *3*, 348–353.
15. Nelayah, J.; Gu, L.; Sigle, W.; Koch, C. T.; Pastoriza-Santos, L.; Liz-Marzan, L. M.; van Aken, P. A. *Proceedings of the 14th European Microscopy Congress 2*; Springer: Berlin, 2008; p 243.
16. Nelayah, J.; Gu, L.; Sigle, W.; Koch, C. T.; Pastoriza-Santos, L.; Liz-Marzan, L. M.; van Aken, P. A. Direct Imaging of Surface Plasmon Resonances on Single Triangular Silver Nanoprisms at Optical Wavelength Using Low-Loss EFTEM Imaging. *Opt. Lett.* **2009**, *34*, 1003–1005.
17. Gu, L.; Sigle, W.; Koch, C. T.; Ögüt, B.; van Aken, P. A.; Talebi, N.; Vogelgesang, R.; Mu, J.; Wen, X.; Mao, J. Resonant Wedge Plasmon Modes in Single-Crystalline Gold Nanoplatelets. *Phys. Rev. B* **2011**, *83*, 195433/1–195433/7.
18. Schaffer, B.; Hohenester, U.; Trügler, A.; Hofer, F. High-Resolution Surface Plasmon Imaging of Gold Nanoparticles by Energy-Filtered Transmission Electron Microscopy. *Phys. Rev. B* **2009**, *79*, 041401/1–041401/4.
19. Sigle, W.; Nelayah, J.; Koch, C. T.; van Aken, P. A. Electron Energy Losses in Ag Nanoholes—From Localized Surface Plasmon Resonances to Rings of Fire. *Opt. Lett.* **2009**, *34*, 2150–2152.
20. Sigle, W.; Nelayah, J.; Koch, C. T.; Ögüt, B.; Gu, L.; van Aken, P. A. EFTEM Study of Surface Plasmon Resonances in Silver Nanoholes. *Ultramicroscopy* **2010**, *110*, 1094–1100.
21. Liu, N.; Giessen, H. Coupling Effects in Optical Metamaterials. *Angew. Chem., Int. Ed.* **2010**, *49*, 9838–9852.
22. Apell, S. P.; Echenique, P. M.; Ritchie, R. H. Sum Rules for Surface Plasmon Frequencies. *Ultramicroscopy* **1996**, *65*, 53–60.
23. Manjavacas, A.; Garcia de Abajo, F. J. Robust Plasmon Waveguides in Strongly Interacting Nanowire Arrays. *Nano Lett.* **2009**, *9*, 1285–1289.
24. Funston, A. M.; Novo, C.; Davis, T. J.; Mulvaney, P. Plasmon Coupling of Gold Nanorods at Short Distances and in Different Geometries. *Nano Lett.* **2009**, *9*, 1651–1658.
25. Merlin, R. Metamaterials and the Landau−Lifshitz Permeability Argument: Large Permittivity Begets High-Frequency Magnetism. *Proc. Natl. Acad. Sci. U.S.A.* **2009**, *106*, 1693–1698.
26. Falcone, F.; Lopetegi, T.; Laso, M. A. G.; Baena, J. D.; Bonache, J.; Beruete, M.; Marqués, R.; Martin, F.; Sorolla, M. Babinet Principle Applied to the Design of Metasurfaces and Metamaterials. *Phys. Rev. Lett.* **2004**, *93*, 197401/1–197401/4.
27. Zentgraf, T.; Meyrath, T. P.; Seidel, A.; Kaiser, S.; Giessen, H. Babinet's Principle for Optical Frequency Metamaterials and Nanoantennas. *Phys. Rev. B* **2007**, *76*, 033407/1–033407/4.
28. Halas, N. J.; Lal, S.; Chang, W. S.; Link, S.; Nordlander, P. Plasmons in Strongly Coupled Metallic Nanostructures. *Chem. Rev.* **2011**, *111*, 3913–3961.
29. Prodan, E.; Nordlander, P. Plasmon Hybridization in Spherical Nanoparticles. *J. Chem. Phys.* **2004**, *120*, 5444–5454.
30. Seo, M. A.; Koo, H. R. S. M.; Park, D. J.; Kang, J. H.; Suwal, O. K.; Choi, S. S.; Planken, P. C. M.; Park, G. S.; Park, N. K.; Park, Q. H. Terahertz Field Enhancement by a Metallic Nanoslit Operating beyond the Skindepth Limit. *Nat. Photonics* **2009**, *3*, 152–156.
31. Jackson, J. D. *Classical Electrodynamics*; John Wiley & Sons: New Jersey, 1999; pp 488−490.
32. Dorfmüller, J.; Vogelgesang, R.; Weitz, R. T.; Rockstuhl, C.; Etrich, C.; Pertsch, P.; Lederer, F.; Kern, K. Fabry-Pérot Resonances in One-Dimensional Plasmonic Nanostructures. *Nano Lett.* **2009**, *9*, 2372–2377.
33. Dorfmüller, J.; Vogelgesang, R.; Khunsin, W.; Rockstuhl, C.; Etrich, C.; Kern, K. Plasmonic Nanowire Antennas: Experiment, Simulation, and Theory. *Nano Lett.* **2010**, *10*, 3596–3603.
34. Egerton, R. F. *Electron Energy-Loss Spectroscopy in the Electron Microscope*; Plenum Press: New York, 1996; pp 302−307.
35. Koch, C. T.; Sigle, W.; Höschen, R.; Rühle, M.; Essers, E.; Benner, G.; Matijevic, M. SESAM: Exploring the Frontiers of Electron Microscopy. *Microsc. Microanal.* **2006**, *12*, 506–514.
36. Essers, E.; Benner, G.; Mandler, T.; Meyer, S.; Mittmann, D.; Schnell, M.; Höschen, R. Energy Resolution of an Omega-Type Monochromator and Imaging Properties of the MANDOLINE Filter. *Ultramicroscopy* **2010**, *110*, 971–980.
37. Kahl, F.; Rose, H. *Proceedings of the 11th European Conference on Electron Microscopy 1* Dublin, 1996; p 478.
38. Uhlemann, S.; Rose, S. MANDOLINE Filter—A New High Performance Imaging Filter for Sub-eV EFTEM. *Optik* **1994**, *96*, 163–178.
39. Schaffer, B.; Grogger, W.; Kothleitner, G. Automated Spatial Drift Correction for EFTEM Image Series. *Ultramicroscopy* **2004**, *102*, 27–36.
40. Parsons, J.; Hendry, E.; Sambles, J. R.; Barnes, W. L. Localized Surface-Plasmon Resonances and Negative Refractive Index in Nanostructured Electromagnetic Metamaterials. *Phys. Rev. B* **2009**, *80*, 245117/1–245117/6.
41. Degiron, A.; Smith, D. R. Numerical Simulations of Long-Range Plasmons. *Opt. Express* **2006**, *14*, 1611–1625.
42. Nemat-Nasser, S. C.; Amirkhizi, A. V.; Padilla, W. J.; Basov, D. N.; Nemat-Nasser, S.; Bruzewicz, D.; Whitesides, G. Terahertz Plasmonic Composites. *Phys. Rev. E* **2007**, *75*, 036614/1–036614/7.
43. Johnson, P. B.; Christy, R. W. Optical Constants of the Noble Metals. *Phys. Rev. B* **1972**, *6*, 4370–4379.

Supplementary Chapter 4

Hybridized Metal Slit Eigenmodes as an Illustration of Babinet's Principle

Burcu Ögüt, Ralf Vogelgesang, Wilfried Sigle, Nahid Talebi, Christoph T. Koch, Peter A. van Aken

Components: 5 Figures

Figure S4.1: Plasmonic eigenmode images simulated with HFSS for a single silver surface at electron energy-loss values of (a) 1.11 eV , (b) 1.32 eV , and (c) 1.71 eV .

Figure S4.2: Inverse periodicity versus number of nodes plotted for the single slit and outer and inner parts of the double slit.

Figure S4.3: Dispersion of plasmons in single slit and inner and outer parts of double slits.

Figure S4.4: (a) – (h) Experimental EFTEM images acquired in the energy-loss range of 0.4 eV– 1.8 eV. (i) - (p) Intensity profiles along the regions marked in the EFTEM images.

Figure S4.5: (a) - (j) Experimental EFTEM images acquired in the energy-loss range of 0.3 eV– 2.1 eV. (i) – (p) Intensity profiles along the regions marked as 1 and 2 in figures S5.a to S5.j in the EFTEM images.

HFSS simulations (figure S4.1) validate the existence of two, three, and four *E*-field maxima at 1.1 eV (figure S4.1.a), 1.32 eV (figure S4.1.b), and 1.71 eV (figure S4.1.c), respectively, on the 1107 nm long single silver surface.

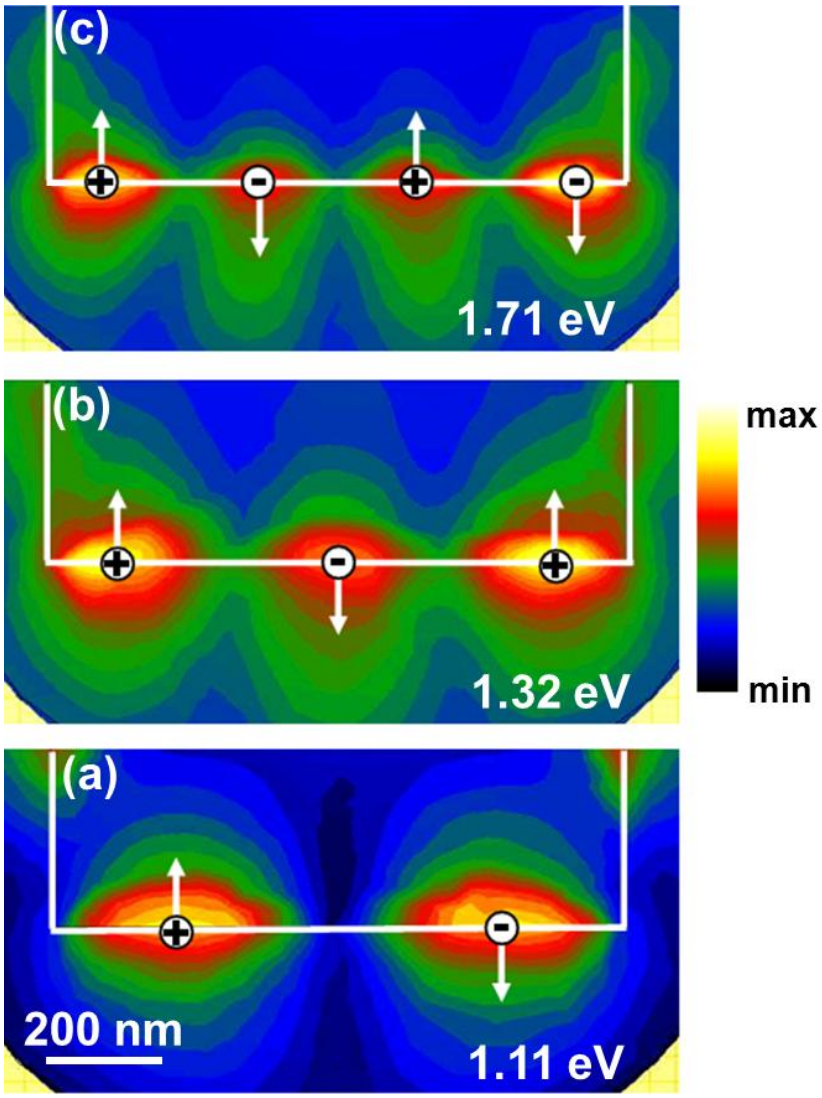

Figure S4.1: Plasmonic eigenmode images simulated with HFSS for a single silver surface at electron energy loss values of (a) 1.11 eV , (b) 1.32 eV , and (c) 1.71 eV .

The reason why these modes found in single and double slits are called Fabry-Pérot-like modes is as follows: The electromagnetic field maxima are confined to the side walls for both, the single and double slits. This is typical for surface plasmons (SPs), because their excitation probability is known to rapidly decrease with increasing distance of the electron beam from the surface. SPs are excited by traversing fast electrons along the side walls. Once the surface plasmon reaches the corner of the slit, it will be partially reflected and interference effects

leading to standing-wave modes will occur, similar as in a Fabry-Pérot resonator formed by terminating a slot waveguide at the two ends without any interaction through free space. As expected from such interferences, the cavity supports eigenmodes of wavelength λ, if the total length of the cavity corresponds to $n \cdot \lambda/2$, where n is a positive integer. $\lambda/2$ is then the separation of neighbouring field maxima. In the case of the single slit, 2, 3, and 4 maxima have been observed. The mode for $n = 1$ occurs at a resonance energy too low to be detectable by the experimental setup.

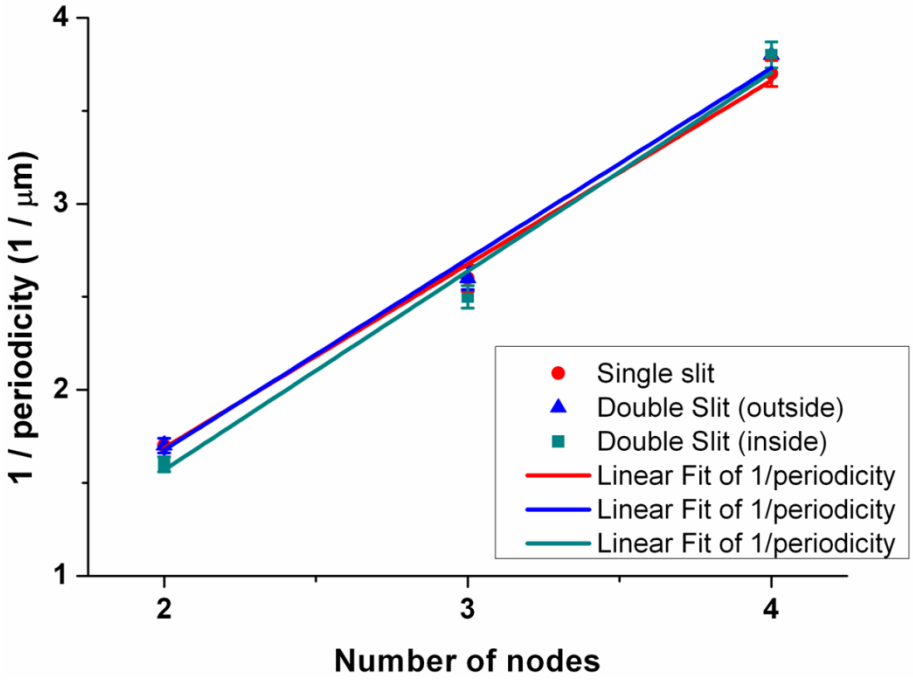

Figure S4.2: Inverse periodicity versus number of nodes plotted for the single slit and outer and inner parts of the double slit. The nearly linear increase is a proof for Fabry-Pérot-like surface plasmon resonances within the slits.

In figure S4.2 the inverse of the maxima periodicity versus the number of nodes is plotted. It can be seen that the inverse periodicity increases almost linearly with the number of nodes, which is evidence of Fabry-Pérot-like SP interferences in a slot waveguide. In addition, the observation of intensity maxima enables to depict the results in a dispersion diagram which is presented in Fig. S4.3 as a plot of the wave vectors versus resonance energies. The black line corresponds to a surface plasmon polariton (SPP) propagating on a free Ag surface in vacuum ($k_{spp} = (2\pi/\lambda)\sqrt{\varepsilon_{Ag}/(1+\varepsilon_{Ag})}$,[1] where ε_{Ag} is the permittivity of Ag). The wave vectors of the resonances found in the experiment are shown as separate data points. They are located at lower

energies than the SPP, i.e. the SP propagation is slower within the single slit (Figure 4.2) than on the free Ag surface. In the case of the double slit (Figure 4.3), the wave vectors of the resonances along the outer slit walls are nearly the same as the wave vectors of the single slits, whereas larger wave vectors were observed along the connecting bridge of the double slits at 1 eV and 1.4 eV, which is closely related to the coupling between the slits.

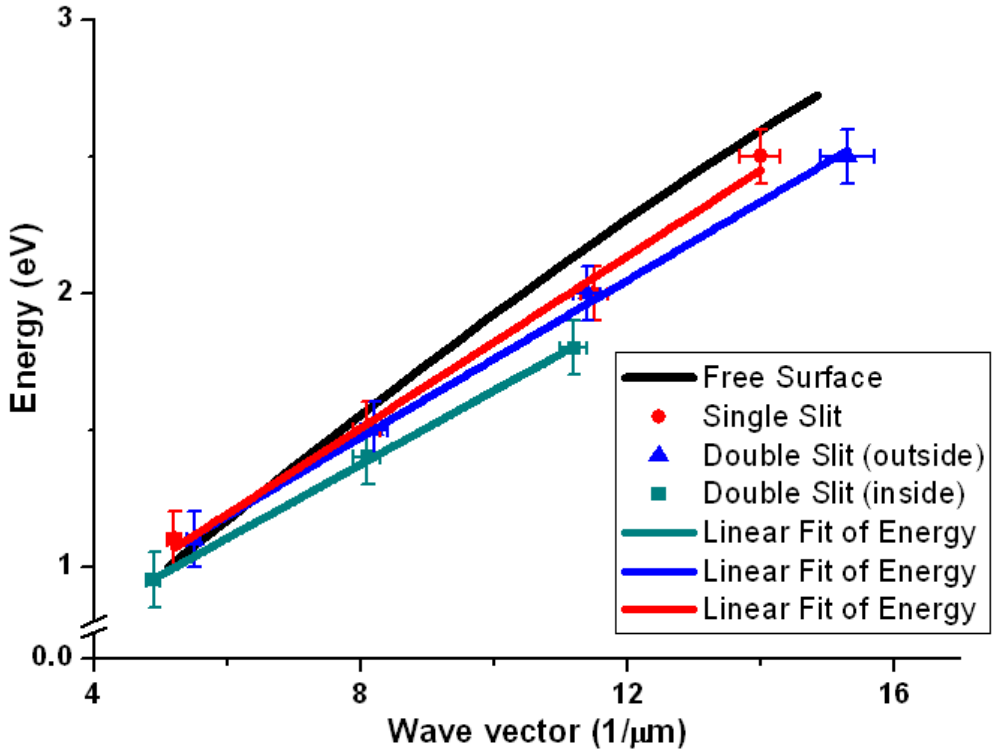

Figure S4.3: Dispersion of plasmons in a single slit and at the inner and outer parts of a double slit. The solid line shows the theoretical dispersion of SPPs on a free silver surface, ($\boldsymbol{k_{spp} = (2\pi/\lambda)\sqrt{\varepsilon_{Ag}/(1+\varepsilon_{Ag})}}$). The lower energy of the SP at the inner edge indicates coupling of SPs on both sides of the connecting bridge.

In order to confirm Babinet's principle experimentally, some experiments were performed on single and double nanorods (figures S4.4 and S4.5) having similar dimensions with the rectangular slits that were investigated. These structures have been manufactured with e-beam nanolithography technique by Dipl.–Ing. Melanie Rohm[2]. A 30 nm thick SiN_4 membrane was used for drawing the structures. Firstly, the membrane was covered with poly(methyl methacrylate) (PMMA) which is the positive electron-sensitive resist. Single and double silver nanorods were drawn on the resist. After the drawing procedure was over, the exposed parts of the resist were dissolved by evaporation of 20 nm thick silver layer. Finally the remaining resist

was dissolved by leaving the printed nanostructures behind. As previously discussed in chapter 4, the complementary structure is supposed to reveal similar response to electron beam excitation according to Babinet's principle. This means that SPRs are expected to be observed along the longer and shorter edges having longitudinal and transverse character[3,4] at similar energies to the ones observed in nanoslits but the spatial symmetry of the resonances are supposed to be reversed as already proven in another reference[5].

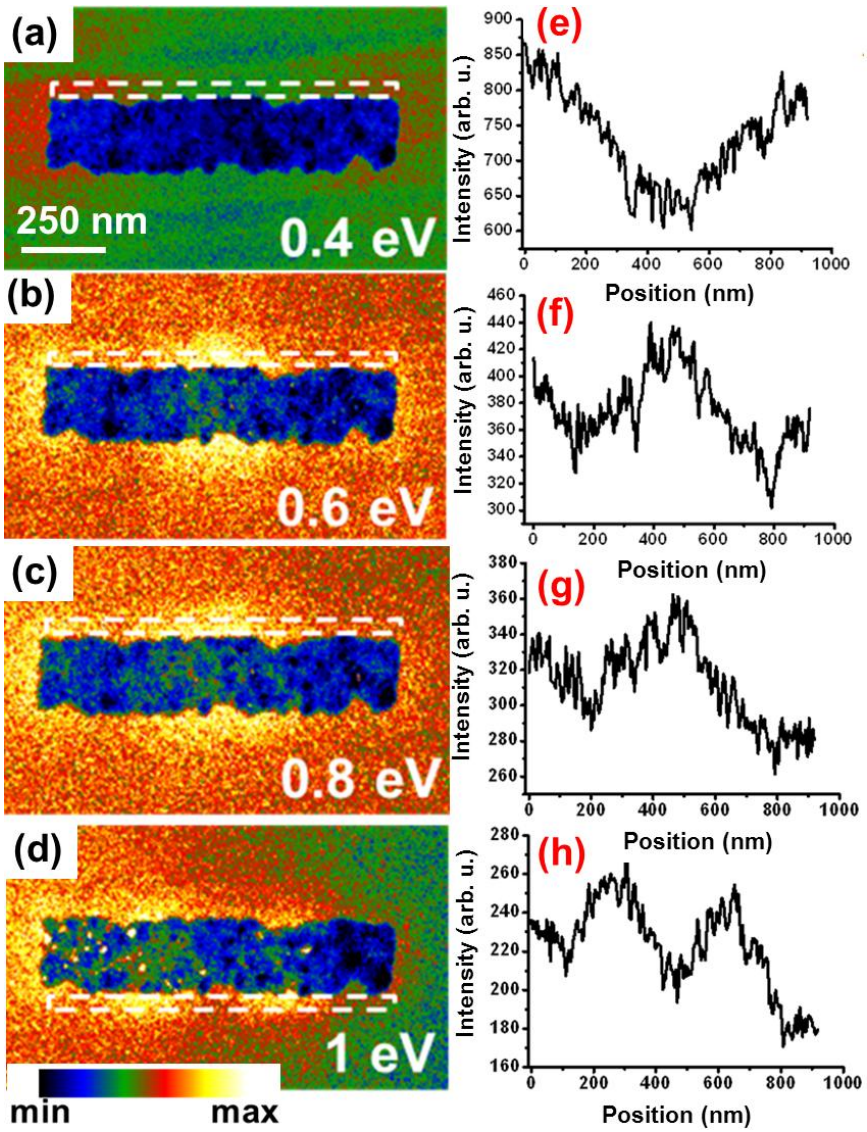

Figure S4.4: (a) - (h) Experimental EFTEM images acquired at the energy-loss range of 0.4 eV-1.8 eV. (i) - (p) Intensity profiles along the regions marked in the EFTEM images.

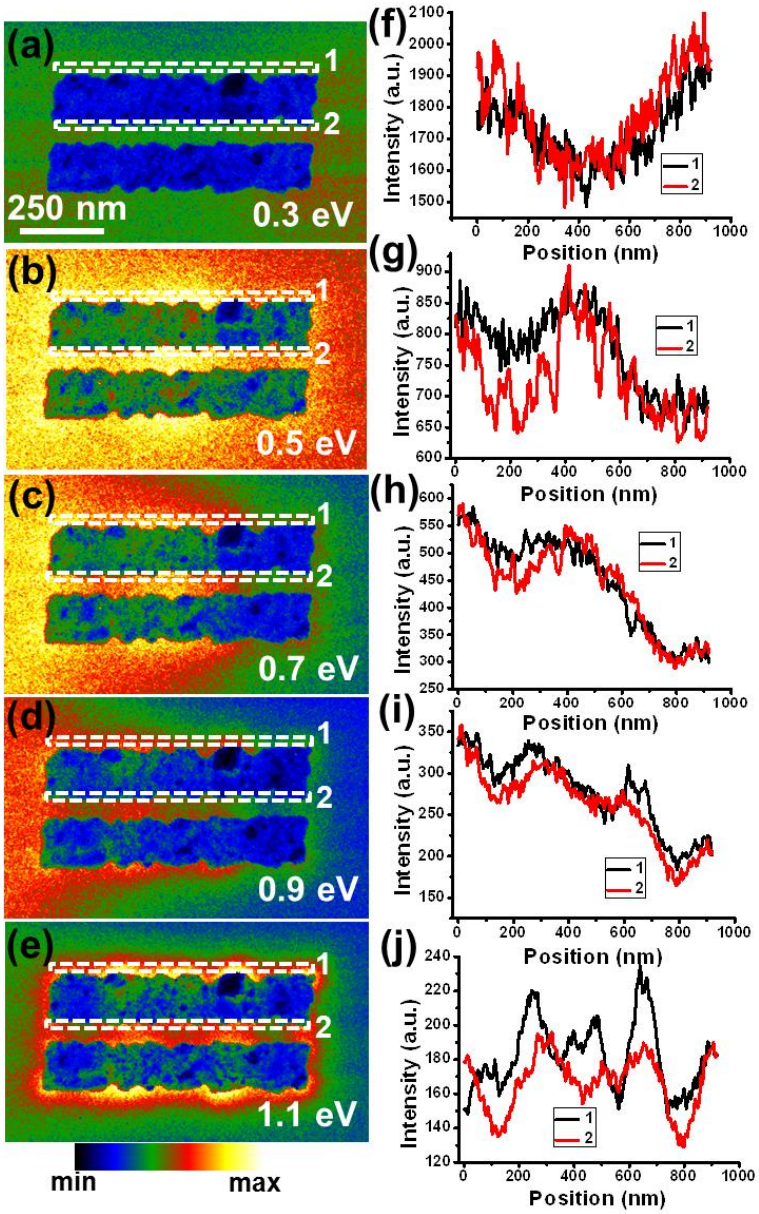

Figure S4.5: (a) – (j) Experimental EFTEM images acquired in the energy-loss range of 0.3 eV–2.1 eV. (i) – (p) Intensity profiles along the regions marked as 1 and 2 in figures S5.a to S5.j in the EFTEM images.

Figure S4.4 shows the experimental EFTEM images acquired at the energy-loss range of 0.4 eV-1 eV. The intensity profiles (figure S4.4.e-h) taken from the marked regions in figures S4.4 (a–d) show that the number of maxima is increasing as the electron energy-loss value increases from 0.4 eV to 1.8 eV, which is in perfect agreement with the theory and the expectations (Figures S4.4 e–h). The primary eigenmode behaviour for the nanoslits could not

have been captured with EFTEM imaging, but is observed at an energy loss value of 0.48 eV via HFSS simulations appearing as one intensity maximum on the long slit wall (figure 2.11 b). In the case of the nanorods, it could be resolved that the intensity maxima are placed at the two tips of the nanorod at 0.4 eV, although this energy loss value is very close to the tail of the zero loss peak. The other eigenmodes show a plasmonic response in agreement with Babinet's principle as well, in comparison to the results that have been shown in figure 2 of chapter 4. For the case of the double nanorods (figure S4.5) the plasmonic behaviour is in agreement with Babinet's principle too.

It could be observed in both types of structures that the surface roughness is quite high in longitudinal direction. The intensity profiles (figure S 4.4 (e-h) & figure S4.5 (f-j)) prove this statement. The positions of the intensity maxima have been measured to be at the expected positions. However, roughness causes some additional hot spots to occur, which makes it hard to distinguish the real surface plasmon peaks from the hot spots along the edges due to surface roughness. Therefore, the other higher order plasmonic eigenmodes of the nanorods, which are expected to reveal complementary behaviour to the plasmonic eigenmodes in nanoslits having more than two nodes in longitudinal direction, could not be distinguished due to high roughness.

The main important point to be concluded from these images is that surface roughness plays a crucial role at the interpretation stage, as it can directly affect the number and even hinder the appearance of intense maxima of a plasmonic eigenmode, clearly observable in all energy losses in figure S4.5. On the other hand, roughness could be used as an advantage to create new eigenmodes that are desired for various applications. Chapters 8 and 9 give deeper insight into the plasmonic eigenmodes of nanoparticles with smoother edges having different shapes, such as hexagons, triangles, and truncated triangles.

References

1. Raether, H. *Excitations of plasmons and interband transitions by electrons*, 1980, Springer-Verlag, Berlin, Heidelberg, New York.
2. Rohm, M., Reindl, T.; Sigle, W.; Ögüt, B.; Talebi, N.; Vogelgesang, R.; van Aken, P.A. Surface plasmon coupling in split-ring resonator dimers, Abstract for the 12th International Conference on near-field optics, nanophotonics and related techniques, NFO 2012, (2012) San Sebastian, Spain.
3. Alber, I.; Sigle, W.; Demming-Janssen, F.; Neumann, R.; Trautmann, C.; van Aken, P.A.; Toimil-Molares, M.E. Multipole surface plasmon resonances in conductively coupled metal nanowire dimers, *ACS Nano*, **6**, 9711-9717, (2012).
4. Alber, I.; Sigle, W.; Müller, S.; Neumann, R.; Picht, O.; Rauber, M.; van Aken, P.A.; Toimil-Molares, M.E. Visualization of multipolar longitudinal and transversal surface plasmon modes in nanowire dimers, *ACS Nano* **5**, 9845-9853, (2011).
5. Rossouw, D.; Botton, G.A. Resonant optical excitations in complementary plasmonic nanostructures, *Optics Express* **20**, 6968-6973, (2012).

CHAPTER 5

Toroidal Plasmonic Eigenmodes in Oligomer Nanocavities for the Visible

Burcu Ögüt[1], Nahid Talebi[1], Ralf Vogelgesang[2], Wilfried Sigle[1], and Peter A. van Aken[1]

1. Max Planck Institute for Intelligent Systems, Heisenbergstraße 3, 70569, Stuttgart, Germany
2. Max Planck Institute for Solid State Research, Heisenbergstraße 1, 70569, Stuttgart, Germany

Circular holes arranged in a plasmonic heptamer configuration have been examined. The existence of toroidal moments at optical wavelengths was proven by EFTEM imaging. The experiments were supported by FDTD simulations. Burcu Ögüt has done the microscopy work and Nahid Talebi performed the simulations. Ralf Vogelgesang has drawn the illustrations in the figures. All of the co-authors have contributed to the interpretation of experimental and simulation results.

NANO LETTERS

Letter

pubs.acs.org/NanoLett

Toroidal Plasmonic Eigenmodes in Oligomer Nanocavities for the Visible

Burcu Ögüt,*[,†] Nahid Talebi,[†] Ralf Vogelgesang,[‡] Wilfried Sigle,[†] and Peter A. van Aken[†]

[†]Max Planck Institute for Intelligent Systems, Heisenbergstraße 3, 70569 Stuttgart, Germany

[‡]Max Planck Institute for Solid State Research, Heisenbergstraße 1, 70569 Stuttgart, Germany

Supporting Information

ABSTRACT: Plasmonics has become one of the most vibrant areas in research with technological innovations impacting fields from telecommunications to medicine. Many fascinating applications of plasmonic nanostructures employ electric dipole and higher-order multipole resonances. Also magnetic multipole resonances are recognized for their unique properties. Besides these multipolar modes that easily radiate into free space, other types of electromagnetic resonances exist, so-called toroidal eigenmodes, which have been largely overlooked historically. They are strongly bound to material structures and their peculiar spatial structure renders them practically invisible to conventional optical microscopy techniques. In this Letter, we demonstrate toroidal modes in a metal ring formed by an oligomer of holes. Combined energy-filtering transmission electron microscopy and three-dimensional finite difference time domain analysis reveal their distinct features. For the study of these modes that cannot be excited by optical far-field spectroscopy, energy-filtering transmission electron microscopy emerges as the method of choice. Toroidal moments bear great potential for novel applications, for example, in the engineering of Purcell factors of quantum-optical emitters inside toroidal cavities.

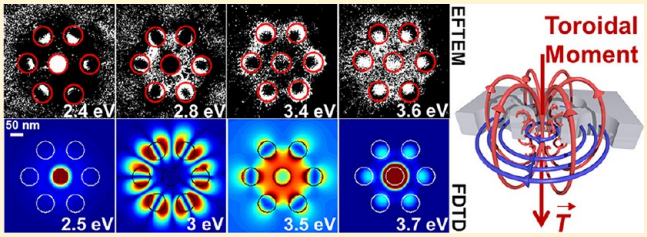

KEYWORDS: *Energy-filtering TEM, 3D finite-difference time-domain, toroidal eigenmodes, oligomers, plasmonics, nanocavities*

The inevitable trend of miniaturization in electronic devices has introduced an epoch for the young field of plasmonics, holding the attention of biological[1,2] and chemical[3] research, surface enhanced Raman Spectroscopy,[4] solar energy,[5] telecommunication technology,[6] and transformation optics.[7] It has become a vital issue to visualize and understand how the avant-garde class of materials designed for these applications behave electromagnetically in terms of electromagnetic field concentration and coupling in the optical wavelength regime. Therefore different imaging techniques[8] have been applied to nanoparticles and nanoholes[9] with different geometrical shapes, such as triangles,[10] spheres,[11,12] rods,[13] or split-rings.[14] Predominantly, electrical and magnetic dipolar and higher order resonances have been taken into consideration while studying these structures. However, toroidal moments represent a category of magnetoelectric moments by themselves, which are mostly disregarded as they are not so straightforward to detect, especially in nanoscale structures.

Starting from the late 1950s,[15] toroidal moments $\vec{T}$ have been studied at first in nuclear physics.[16] They are characterized by rings of radial electric field loops, $\vec{E}$, as depicted in Figure 1g, which is in contrast to the azimuthal field loop that generates the magnetic field component $\vec{H}$ of a simple ring. Toroidal polarizations are rare but possible in the solid state, as well. Recently, multiferroic materials have been discovered that even support ferrotoroidic domains.[17] A key feature in all occurrences of toroidal moments is space−time symmetry. Electric dipoles ($\vec{P} = \sum_i q_i \vec{r}_i$) change their sign only with space inversion ($\vec{r} \rightarrow -\vec{r}$) and magnetic dipoles ($\vec{m} = \sum_i q_i \vec{r}_i \times d\vec{r}_i/dt$) change their sign only with time reversal ($t \rightarrow -t$). Toroidal moments

$$\vec{T} = \sum_i q_i \vec{r}_i \times \left(\vec{r}_i \times \frac{d\vec{r}_i}{dt} \right) \quad (1)$$

however, swap their sign under either spatial inversion or time reversal.[18] A well-known example of a structure exhibiting a toroidal moment is a solenoid that is bent into a ring, or equivalently, a closed loop of azimuthally oriented magnetic moments. This behavior hints at an intricate coupling between ordinary electric and magnetic dipoles, as is indeed the case in the magnetoelectric effect. The hybrid nature of toroidal moments introduces options to influence magnetic polarization by electric fields and vice versa.[19]

Even though toroidal moments have been discussed for decades, only recently there is a marked interest in their characteristics,[18,20−22] and the design of proper structures that can sustain them under electromagnetic excitation.[23−25] Partly this is due to the weak far-field optical signatures of toroidal resonances. Usually, they do not radiate or their contribution is

Received: June 29, 2012
Revised: August 27, 2012
Published: August 30, 2012

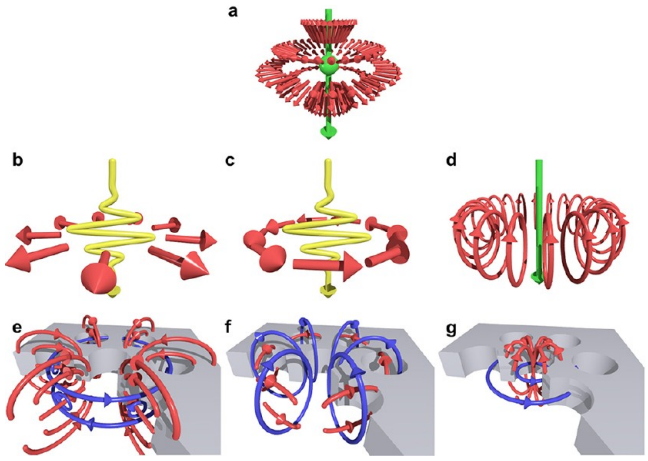

Figure 1. For excitation, we use (a) the relativistic field attached to the relativistic electrons in TEM and (b–d) optical excitations in FDTD: (b) radially and (c) azimuthally polarized far-field radiation, and (d) radiation emitted by an electric dipole placed in the central hole. The main classes of response fields sustained by the 6-fold torus are (e) radial electric dipolar and (f) radial magnetic dipolar, as well as (g) toroidal modes. Electric (magnetic) fields are indicated by red (blue) arrows.

masked by conventional multipolar far-field radiation.[26] In this context it is noteworthy that Kaelberer et al.[27] succeeded in observing toroidal moments using microwave split ring resonators, and Huang et al.[28] proposed an alternative structure which makes the toroidal resonances prominent at optical frequencies.

In this Letter, we present experimental and theoretical evidence for toroidal modes at visible frequencies, using energy-filtering transmission electron microscopy (EFTEM) and three-dimensional finite-difference time-domain analysis (3D-FDTD) of near- and far-field excitations. Our investigated structure consists of seven round holes of 60 nm diameter, drilled in a free-standing 60 nm thick silver film. First, silver discs with 3 mm diameter were punched from cold-rolled and annealed silver film. Afterwards the discs were electropolished in a Struers-Tenupol 5 by using a cyanide-free solution[29] until a hole was visible in the center of the disk. Voltage, current, and the light sensitivity value were set to 4 V, 25 mA, and 100, respectively. Finally the specimen was ion-milled at the Low-Angle Ion Milling & Polishing system (FISCHIONE Instruments-Model 1010) for final cleaning for an hour in total (at 2 kV for 30 min, at 0.5 kV for 30 min). A double beam was used at a milling angle of 12°. Both upper and lower sources were set to a current of 5 mA. The final thickness of the specimen was 60 ± 10 nm. The thickness measurement was done by comparing the areas below the zero loss peak and the total area in an electron energy-loss spectrum, namely the log–ratio method.[30]

The heptamer nanoholes consisting of seven circular holes (diameter = 60 nm) were drilled into the film by a focused ion beam (FIB) (FEI Nova NANOLAB 60) at 30 kV near the rim of the perforated area. The sub-electronvolt sub-angstrom microscope (SESAM, Zeiss, Oberkochen, Germany), operated at 200 kV, was used to implement the EFTEM experiments on the heptamer nanoholes. EFTEM is a technique based on electron energy-loss spectroscopy (EELS) and allows obtaining images formed by electrons having suffered specific energy losses in the material. The MANDOLINE energy filter and a symmetric electrostatic omega-type electron monochromator provide an energy resolution better than 100 meV, a high dispersion of the energy-loss spectrum (~6 μm/eV), and a small nonisochromaticity of 0.1 meV/nm.[31,32] During the EFTEM imaging procedure both the monochromator slit and energy filter slit had a width of 0.2 eV. Energy-filtered images were acquired at an energy loss step of 0.2 eV between 0 and 7 eV, and recorded on a $2k \times 2k$ CCD camera (Ultrascan, Gatan, USA) with a binning of 4. In order to exclude the camera artifacts due to scintillator afterglow, image acquisition was started from 7 eV, where the intensity is lowest, and was stopped at a value just below the intense zero-loss peak. In addition, a new dark reference was acquired after each energy-filtered image. The acquisition time was set automatically for each image with the constraint of a maximum time of 30 s to minimize image blurring stemming from specimen drift. The specimen drift between individual images was corrected by application of a script described in ref 33. The weighted principal component analysis (PCA) has been applied on the structure by selecting 14 components in order to reduce noise. To identify the exact energy positions of the weak spectral peaks in the data cube a peak-finding algorithm was written with Digital Micrograph scripting language. This is an essential tool for mapping the positions in the low-energy-loss region since there is no background function available for this energy region.[34] A bright-field image of the investigated structure is displayed in the Supporting Information Figure 1.

The 3D-FDTD method was used to simulate the electromagnetic behavior of heptamer holes. Yee's mesh was imposed on the structure and the edge length of the cubic cells used in order to discretize the structure was 2 nm. The dispersion of silver was based on a Drude model with two critical point functions. A Ricker wavelet was introduced as the temporal dependence of the incident beam for visualizing the plasmonic eigenmodes at different energies, as a Huygens source introduced in a plane 500 nm above the structure. For the spatial distribution of the excitation, different functions were used to efficiently decompose the symmetry of various modes. Near-field simulations were performed by placing an electric or magnetic dipole at the central hole in the structure to see the electrical and magnetic field distribution.

Our investigated structure consists of seven circular holes; a central hole is surrounded by a six-membered ring of holes. As this structure shares the D_{6h} symmetry[35] class with the benzene molecule and similar artificial plasmonic particle oligomers,[36–38] the group theoretical mode spectrum is the same in all cases. However, the topology of an oligomer of holes (a 6-fold toroid) is distinctly different from that of the complementary oligomer of separate particles. This promises an opportunity to discover eigenmodes in the toroidal system whose spatial structure does not resemble any mode of the discrete particle system.

EELS[10,39–42] and EFTEM[43–46] are quite advantageous in the study of plasmonic eigenmodes thanks to the unique spatial structure of the electromagnetic field attached to its relativistic electron probe, as illustrated in Figure 1a, acting as a near-field excitation source. It shares certain features, but is never identical, with various optical excitation field geometries (radial and azimuthal far-field, and dipolar near-field; Figure 1b–d). Using the varying degrees of overlap between electronic and optical excitations, their combined study yields a comprehensive understanding of a sample's eigenmodes. The principal resonances that can be observed with these excitation types are

dx.doi.org/10.1021/nl302418n | Nano Lett. 2012, 12, 5239–5244

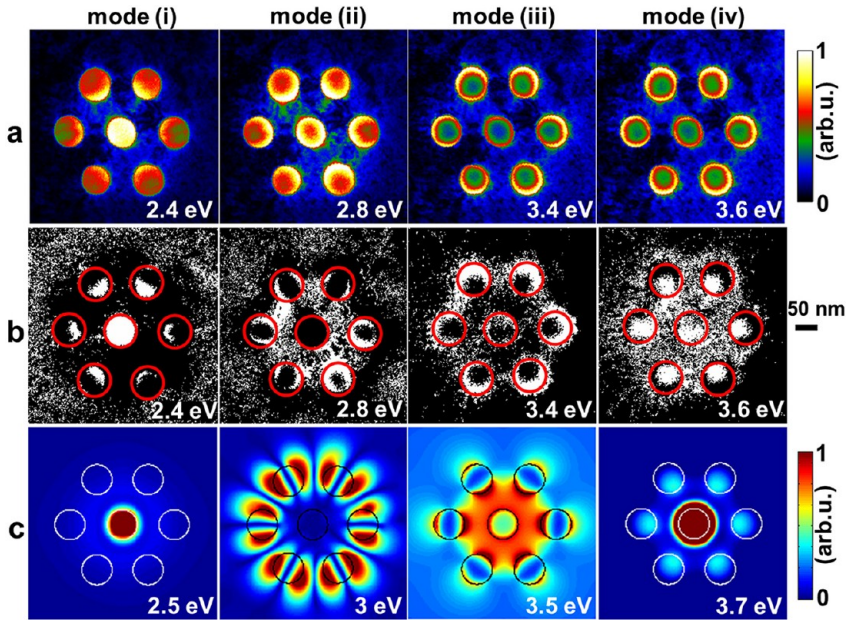

Figure 2. (a) Collection of modes acquired in EFTEM experiment at energy losses of (i) 2.4, (ii) 2.8, (iii) 3.4, and (iv) 3.6 eV. (b) Peak maps obtained from the acquired images in (a). (c) Simulated modes with FDTD. Displayed is the modulus of the electric field ($|E_z|$) at (i) 2.5, (ii) 3, (iii) 3.5, and (iv) 3.7 eV. The scale bar applies to all images.

illustrated in Figure 1e–g. Of particular interest in the present context are the toroidal modes, Figure 1g. Their weakly radiative character makes a near-field optical source compulsory, such as a vertical electric dipole emitter centered in the middle hole (Figure 1d). The simultaneous absence of near-field excitable resonances in far-field excited simulations is a fingerprint signature of toroidal modes, whose traces can be recognized in EFTEM experiments.

In Figure 2, we display EFTEM images (Figure 2a), corresponding peak maps (Figure 2b), and images from FDTD analysis (Figure 2c). Colors in Figure 2a represent the energy-loss probability, which is a measure of the *z*-component of the excited electric field, E_z. At an energy loss of 2.4 eV (mode (i)), intensity maxima are mainly concentrated in the central hole and along the inner rims of the surrounding holes indicating electromagnetic interaction in radial direction. At 2.8 eV (mode (ii)), electromagnetic interaction is observed between the surrounding holes in azimuthal direction. At 3.4 eV (mode (iii)) and 3.6 eV (mode (iv)), high field strengths are mainly observed along the outer rims of the surrounding holes. To unravel the symmetries of these resonances, peak maps (Figure 2b) are extracted from the EFTEM data cube (Figure 2a). Whereas EFTEM images show the E_z component at single energy slices, peak maps highlight the spatial distribution of spectral peaks, thus reducing the monotonous spectral tails of resonances at other energies. The peak maps of mode (i) and mode (iii) affirm the raw EFTEM images, indicating strong eigenmodes that are spectrally well isolated. In contrast, the peak maps at modes (ii) and (iv) differ noticeably from the corresponding EFTEM images. Associated resonances are relatively weaker and/or spectrally closer to other eigenmodes. The peak map of mode (ii) reveals clearly that the electromagnetic interaction between the surrounding holes is more pronounced in the azimuthal direction than in radial direction. The peak map of mode (iv) uncovers a shape that is not discernible in the corresponding EFTEM image, comprising peaks concentrated in the central hole and at the inner part of the surrounding holes. The resonance widths of modes (i) and (iv) are (0.4 ± 0.05) and (0.3 ± 0.05) eV, respectively.

Figure 2c highlights simulated images of the $|E_z|$ field component, obtained with different optical excitations as specified below. The spatial field distribution and the resonance energies are in very good agreement with experimental results (Figure 2a,b), lending assurance that FDTD calculations may be used to interpret mode structure. Most importantly, we will show in the following that the simulated modes (i) and (iv), observed at energy losses of 2.5 and 3.7 eV, respectively, are indeed toroidal resonances. In contrast, modes (ii) (at 3.0 eV) and (iii) (at 3.5 eV) are of prevailingly magnetic and electric dipolar nature, respectively.

Far-field simulations with radially polarized excitation reveal two prominent multipolar resonances at energies of 2.7 and 3.5 eV, respectively, shown in Figure 3. On the surface of the sample structure, electric field components oscillate in predominantly radial direction, accumulating opposite electrical charges on the inner and outer rim of the surrounding holes, which thus tend to behave like capacitors. Correspondingly, magnetic field vectors whirl in mostly azimuthal direction. Mode symmetry and energy identify the 3.5 eV resonance as mode (iii) from the EFTEM results (Figure 2a), whereas the calculated 2.7 eV mode appears to be masked in EFTEM by the eigenmode measured at 2.8 eV (Figure 2a). The reason for this suppression becomes clear, when the cross sectional symmetry is considered. As can be observed in Figure 3b, in the case of the 2.7 eV resonance the electric fields flip sign between the upper and lower substrate surfaces, giving rise to a quadrupolar plasmon mode.[47] At 3.5 eV, the electric fields do not differ in direction on the upper and lower surfaces (Figure 3e), giving this resonance a more easily excitable dipolar character.

An electromagnetically dual azimuthally polarized far-field excitation is introduced as well. The dominant response is found at 3 eV, as displayed in Figure 4, and can be associated with the EFTEM mode (ii) of Figure 2a. As expected, magnetic field components are aligned in radial direction. The electric

dx.doi.org/10.1021/nl302418n | *Nano Lett.* 2012, 12, 5239–5244

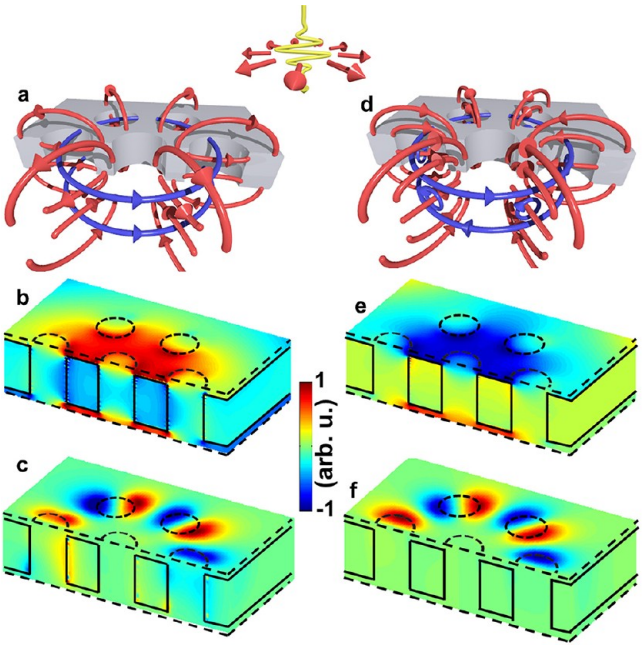

Figure 3. (a) Illustration of electric (red) and magnetic (blue) field lines, (b) instantaneous electric (E_z) and (c) instantaneous magnetic field strength (H_z) of the quadrupolar mode at 2.7 eV. (d) Illustration of field lines, (e) electric and (f) magnetic field strength of the dipolar mode at 3.5 eV. The color bar in the middle applies to (b,c,e,f). Field evaluations above and below the sample are done 4 nm away from the surface.

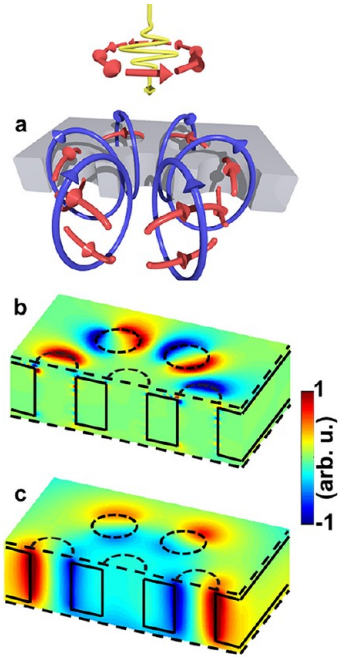

Figure 4. (a) Illustration of electric (red) and magnetic (blue) field lines, (b) instantaneous electric (E_z) and (c) instantaneous magnetic field strength (H_z) of the magnetic dipolar mode at 3 eV. The color bar applies to (b,c). Field evaluations above and below the sample are done 4 nm away from the surface.

fields point in preferentially azimuthal direction, but without *z*-components, which provide strong coupling to the traversing electron in EFTEM.

The simulations above were carried out with far-field excitations and did not trigger any observable toroidal resonances in the heptamer. In the main, the structure's far-field excitable resonances are rather mundane. They may be likened to a ring resonator exhibiting longitudinal and transverse modes in a chain of holes, much like the well-known Babinet complementary chain of particles.[48] However, modes (i) and (iv), which are clearly observed in EFTEM, are conspicuously missing in all the far-field simulations discussed so far. To explore these modes further, we introduce a near-field source for the FDTD simulations. An efficient excitation is provided by coupling a vertical dipole emitter in the middle of the central hole to the structure, as demonstrated in Figure 5.

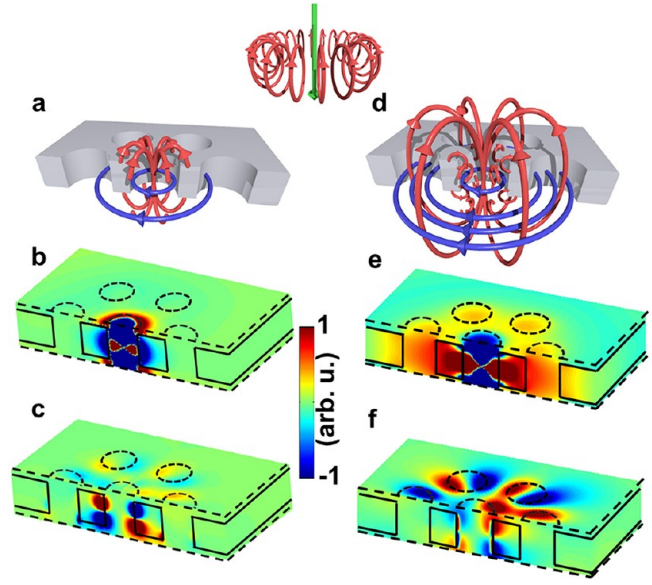

Figure 5. An electric dipole excitation was placed in the central hole. (a) Illustration of electric (red) and magnetic (blue) field lines, (b) instantaneous electric (E_z), and (c) instantaneous magnetic field strength (H_z) of the fundamental toroidal mode at 2.5 eV. (d) Illustration of field lines, (e) electric and (f) magnetic field strength of the second order toroidal mode at 3.7 eV. The color bar in the middle applies to (b,c,e,f). Field evaluations above and below the sample are done 4 nm away from the surface.

Our simulations with near-field excitation indeed verify resonances in the heptamer of holes at 2.5 and 3.7 eV, which is in excellent agreement with the experimentally found modes (i) and (iv) of Figure 2. Simulated near-field profile approves these resonances at 2.5 and 3.7 eV, also (Supporting Information Figure 2). The detailed analysis of field lines reveals a clearly toroidal character for both modes, illustrated in Figure 5a,d. The sample volume between the central and surrounding holes acts as a ring, around which toroidal moments can build up. The spokes that connect the ring to the outer bulk of the substrate evidently do not disrupt the topologically protected toroidal behavior. Magnetic field distributions (Figure 5c,f) encircle the central hole and electric fields flow in radial loops between the central and surrounding holes. The resonance at 3.7 eV is a higher-order toroidal mode. To illuminate further the toroidal character of these modes, we display in Figure 6 the optical currents extracted from our FDTD results. In both cases (Figure 6d,e), a cylindrical sheet of dipole moments is found to oscillate parallel to the symmetry axis of the sample. The currents are mostly concentrated in the supported silver ring

dx.doi.org/10.1021/nl302418n | *Nano Lett.* 2012, 12, 5239−5244

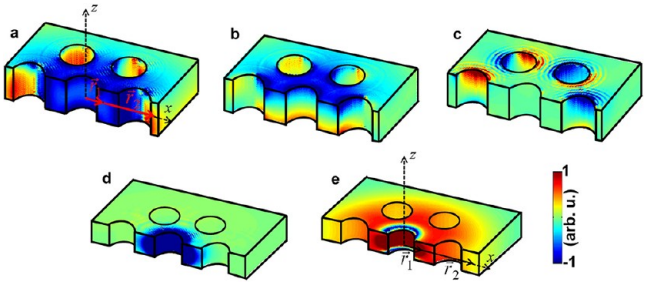

Figure 6. Moduli of the electric currents ($\vec{J}_z$) that build up the different modes at the energies of (a) E = 2.7 eV, (b) E = 3.5 eV, (c) E = 3 eV, (d) E = 2.5 eV, and (e) E = 3.7 eV, corresponding to quadrupolar radial, dipolar radial, azimuthal radial, and first and second toroidal modes, respectively.

surrounding the central hole, which results in strong toroidal moments, according to eq 1. It is evident why the azimuthal and radial electric dipole modes cannot result in a toroidal moment. The oscillation of the dephased currents violates the existence of a toroidal moment in z-direction. The resonance at E = 2.7 eV supports only a negligible toroidal moment, since $\vec{r}_1 \times (\vec{r}_1 \times \vec{J}(\vec{r}_1)) + \vec{r}_2 \times (\vec{r}_2 \times \vec{J}(\vec{r}_2)) \approx 0$ (see Figure 6). In contrast to the quadrupolar resonance, the toroidal resonances at E = 2.5 eV and E = 3.7 eV sustain a longitudinal current, localized at the silver ring separating the central hole from the other holes. For this reason, we believe that the distance between the central and the surrounding holes as well as the thickness of the silver film play an important role on the quality factor and resonance energy of the indicated toroidal mode.

The simulations above thus explain nicely all features observed in EFTEM. In addition, we have also considered the case of a dual[26] magnetic toroidal moment, which may be excitable by a magnetic dipole in the central hole instead of an electric dipole. The structure is expected to act in a complementary way, as if E and H are converted to H and $-E$, respectively.[49] Simulations revealed a possible resonance of such symmetry at 3.8 eV. However, at 3.8 eV the volume plasmon energy of silver dominates the spectral response making this toroidal mode experimentally inaccessible.

In summary, we have demonstrated the occurrence of toroidal moments at optical wavelengths for the first time experimentally. We have applied EFTEM imaging to a heptamer of circular holes in a silver film, arranged in such a way that between a central one and six surrounding holes a supported silver ring is formed. Thanks to the power of EFTEM, a number of eigenmodes of this ring structure could be visualized with nanometer spatial and a few tens of millielectronvolts spectral resolution. In particular, we observed radiation-free near-field optical features of two optically completely dark modes. FDTD simulations with a suitable near-field source revealed them to be toroidal resonances. Besides the fundamental toroidal mode at 2.4 eV also a higher order mode was found at 3.6 eV. Additional bright eigenmodes at 2.8 and 3.6 eV have multipolar characters.

Our present results demonstrate distinct toroidal resonances in the visible to ultraviolet spectral ranges. They are easily scalable to longer wavelengths, and we expect them to find many novel applications through innovative near-field optical engineering. For example, novel approaches to Fano spectral engineering by coupling toroidal dark and bright modes. This can be achieved, for example, by breaking the symmetry of the induced longitudinal currents by adding a substrate, or by breaking the azimuthal symmetry by altering the geometry of one of the outer holes.[50] A linear sequence of toroidal systems may constitute novel approaches to waveguides and resonators. Particle heptamers can be used to produce multiheptamer waveguide structures, along which magnetic plasmons propagate.[51] Also, coupling of single quantum systems to the near-fields of toroidal cavities should provide options for pronounced lifetime engineering via the Purcell-effect,[52−54] with implications for instance in quantum information storage and processing.[55−57]

■ ASSOCIATED CONTENT

Ⓢ Supporting Information

Additional figures. This material is available free of charge via the Internet at http://pubs.acs.org.

■ AUTHOR INFORMATION

Corresponding Author

*E-mail: ogut@is.mpg.de. Telephone: (711) 689-3637.

Notes

The authors declare no competing financial interest.

■ ACKNOWLEDGMENTS

We thank U. Eigenthaler and I. Lakemeyer for the support during the specimen preparation, C.T. Koch for writing the scripts regarding EFTEM acquisition and peak finding algorithm, and V. Fedotov for the fruitful discussions. N. Talebi gratefully acknowledges the Alexander-von-Humboldt foundation for financial support.

■ REFERENCES

(1) Anker, J. N.; Hall, W. P.; Lyandres, O.; Shah, N. C.; Zhao, J.; Van Duyne, R. P. *Nat. Mater.* **2008**, *7* (6), 442−453.
(2) Bardhan, R.; Lal, S.; Joshi, A.; Halas, N. J. *Acc. Chem. Res.* **2011**, *44* (10), 936−946.
(3) Tittl, A.; Mai, P.; Taubert, R.; Dregely, D.; Liu, N.; Giessen, H. *Nano Lett.* **2011**, *11* (10), 4366−4369.
(4) Lim, D.-K.; Jeon, K.-S.; Hwang, J.-H.; Kim, H.; Kwon, S.; Suh, Y. D.; Nam, J.-M. *Nat. Nanotechnol.* **2011**, *6* (7), 452−460.
(5) Linic, S.; Christopher, P.; Ingram, D. B. *Nat. Mater.* **2011**, *10* (12), 911−921.
(6) MacDonald, K. F.; Samson, Z. L.; Stockman, M. I.; Zheludev, N. I. *Nat. Photonics* **2009**, *3* (1), 55−58.
(7) Pendry, J. B.; Schurig, D.; Smith, D. R. *Science* **2006**, *312* (5781), 1780−1782.
(8) Vogelgesang, R.; Dmitriev, A. *Analyst* **2010**, *135* (6), 1175−1181.
(9) García de Abajo, F. J. *Rev. Mod. Phys.* **2007**, *79* (4), 1267−1290.
(10) Nelayah, J.; Kociak, M.; Stephan, O.; Garcia de Abajo, F. J.; Tence, M.; Henrard, L.; Taverna, D.; Pastoriza-Santos, I.; Liz-Marzan, L. M.; Colliex, C. *Nat. Phys.* **2007**, *3* (5), 348−353.
(11) Scholl, J. A.; Koh, A. L.; Dionne, J. A. *Nature* **2012**, *483* (7390), 421−427.
(12) Sonnefraud, Y.; Leen Koh, A.; McComb, D. W.; Maier, S. A. *Laser Photonics Rev.* **2011**, *6* (3), 277−295.
(13) Dorfmüller, J.; Vogelgesang, R.; Khunsin, W.; Rockstuhl, C.; Etrich, C.; Kern, K. *Nano Lett.* **2010**, *10* (9), 3596−3603.
(14) Liu, N.; Liu, H.; Zhu, S.; Giessen, H. *Nat. Photonics* **2009**, *3* (3), 157−162.
(15) Zel'dovich, I. B. *Sov. Phys. JETP* **1958**, *6*, 1184.
(16) Wood, C. S.; Bennett, S. C.; Cho, D.; Masterson, B. P.; Roberts, J. L.; Tanner, C. E.; Wieman, C. E. *Science* **1997**, *275* (5307), 1759−1763.
(17) Van Aken, B. B.; Rivera, J.-P.; Schmid, H.; Fiebig, M. *Nature* **2007**, *449* (7163), 702−705.

(18) Dubovik, V. M.; Tugushev, V. V. *Phys. Rep.* **1990**, *187* (4), 145–202.
(19) Spaldin, N. A.; Fiebig, M.; Mostovoy, M. *J. Phys.: Condens. Matter* **2008**, *20* (43), 434203.
(20) Radescu, E. E.; Vlad, D. H. *Phys. Rev. E* **1998**, *57* (5), 6030–6037.
(21) Radescu, E. E.; Vaman, G. *Phys. Rev. E* **2002**, *65* (4), 046609.
(22) Ederer, C.; Spaldin, N. A. *Phys. Rev. B* **2007**, *76* (21), 214404.
(23) Boardman, A. D.; Marinov, K.; Zheludev, N.; Fedotov, V. A. *Phys. Rev. E.* **2005**, *72* (1–6), 036603.
(24) Marinov, K.; Boardman, A. D.; Fedotov, V. A.; Zheludev, N. *New J. Phys.* **2007**, *9* (9), 324.
(25) Mary, A.; Dereux, A.; Ferrell, T. L. *Phys. Rev. B* **2005**, *72* (15), 155426.
(26) Jackson, J. D. *Classical Electrodynamics*; Wiley: New York, 1999.
(27) Kaelberer, T.; Fedotov, V. A.; Papasimakis, N.; Tsai, D. P.; Zheludev, N. I. *Science* **2010**, *330* (6010), 1510–1512.
(28) Huang, Y.-W.; Chen, W. T.; Wu, P. C.; Fedotov, V.; Savinov, V.; Ho, Y. Z.; Chau, Y.-F.; Zheludev, N. I.; Tsai, D. P. *Opt. Express* **2012**, *20* (2), 1760–1768.
(29) Lyles, R. L., Jr.; Rothman, S. J.; Jäger, W. *Metallography* **1978**, *11* (3), 361–363.
(30) Egerton, R. F. *Electron Energy-Loss Spectroscopy in the Electron Microscope*; Springer: New York, 2011.
(31) Koch, C. T.; Sigle, W.; Höschen, R.; Rühle, M.; Essers, E.; Benner, G.; Matijevic, M. *Microsc. Microanal.* **2006**, *12* (06), 506–514.
(32) Essers, E.; Benner, G.; Mandler, T.; Meyer, S.; Mittmann, D.; Schnell, M.; Höschen, R. *Ultramicroscopy* **2010**, *110* (8), 971–980.
(33) Schaffer, B.; Grogger, W.; Kothleitner, G. *Ultramicroscopy* **2004**, *102* (1), 27–36.
(34) Talebi, N.; Sigle, W.; Vogelgesang, R.; Koch, C. T.; Fernandez-Lopez, C.; Liz-Marzan, L. M.; Ögüt, B.; Rohm, M.; van Aken, P. A. *Langmuir* **2012**, *28* (24), 8867–8873.
(35) Hiberty, P. C.; Danovich, D.; Shurki, A.; Shaik, S. *J. Am. Chem. Soc.* **1995**, *117* (29), 7760–7768.
(36) Fan, J. A.; Wu, C.; Bao, K.; Bao, J.; Bardhan, R.; Halas, N. J.; Manoharan, V. N.; Nordlander, P.; Shvets, G.; Capasso, F. *Science* **2010**, *328* (5982), 1135–1138.
(37) Hentschel, M.; Saliba, M.; Vogelgesang, R.; Giessen, H.; Alivisatos, A. P.; Liu, N. *Nano Lett.* **2010**, *10* (7), 2721–2726.
(38) Liu, N.; Mukherjee, S.; Bao, K.; Brown, L. V.; Dorfmüller, J.; Nordlander, P.; Halas, N. J. *Nano Lett.* **2012**, *12* (1), 364–369.
(39) Batson, P. E. *Phys. Rev. Lett.* **1982**, *49* (13), 936–940.
(40) Rossouw, D.; Couillard, M.; Vickery, J.; Kumacheva, E.; Botton, G. A. *Nano Lett.* **2011**, *11* (4), 1499–1504.
(41) Liang, H.; Zhao, H.; Rossouw, D.; Wang, W.; Xu, H.; Botton, G. A.; Ma, D. *Chem. Mater.* **2012**, *24* (12), 2339–2346.
(42) von Cube, F.; Irsen, S.; Niegemann, J.; Matyssek, C.; Hergert, W.; Busch, K.; Linden, S. *Opt. Mater. Express* **2011**, *1* (5), 1009–1018.
(43) Nelayah, J.; Gu, L.; Sigle, W.; Koch, C. T.; Pastoriza-Santos, I.; Liz-Marzan, L. M.; van Aken, P. A. *Opt. Lett.* **2009**, *34*, 1003–1005.
(44) Schaffer, B.; Hohenester, U.; Trügler, A.; Hofer, F. *Phys. Rev. B* **2009**, *79*, 041401–1–4.
(45) Gu, L.; Sigle, W.; Koch, C. T.; Ögüt, B.; van Aken, P. A.; Talebi, N.; Vogelgesang, R.; Mu, J.; Wen, X.; Mao, J. *Phys. Rev. B* **2011**, *83*, 195433–1–7.
(46) Nicoletti, O.; Wubs, M.; Mortensen, N. A.; Sigle, W.; van Aken, P. A.; Midgley, P. A. *Opt. Express* **2011**, *19* (16), 15371–15379.
(47) Habteyes, T. G.; Dhuey, S.; Cabrini, S.; Schuck, P. J.; Leone, S. R. *Nano Lett.* **2011**, *11* (4), 1819–1825.
(48) Talebi, N.; Mahjoubfar, A.; Shahabadi, M. *J. Opt. Soc. Am. B* **2008**, *25* (12), 2116–2122.
(49) Harrington, R. F. *Time-harmonic electromagnetic fields*; McGraw-Hill: New York, 1961.
(50) Hentschel, M.; Dregely, D.; Vogelgesang, R.; Giessen, H.; Liu, N. *ACS Nano* **2011**, *5* (3), 2042–2050.
(51) Liu, N.; Mukherjee, S.; Bao, K.; Li, Y.; Brown, L. V.; Nordlander, P.; Halas, N. J. *ACS Nano* **2012**, *6* (6), 5482–5488.
(52) Altug, H.; Englund, D.; Vuckovic, J. *Nat. Phys.* **2006**, *2* (7), 484–488.
(53) Vahala, K. J. *Nature* **2003**, *424* (6950), 839–846.
(54) Koenderink, A. F. *Opt. Lett.* **2010**, *35* (24), 4208–4210.
(55) Choi, K. S.; Deng, H.; Laurat, J.; Kimble, H. J. *Nature* **2008**, *452* (7183), 67–71.
(56) Strauf, S.; Stoltz, N. G.; Rakher, M. T.; Coldren, L. A.; Petroff, P. M.; Bouwmeester, D. *Nat. Photonics* **2007**, *1* (12), 704–708.
(57) Hadfield, R. H. *Nat. Photonics* **2009**, *3* (12), 696–705.

Supplementary Chapter 5

Toroidal Plasmonic Eigenmodes in Oligomer Nanocavities for the Visible

Burcu Ögüt, Nahid Talebi, Ralf Vogelgesang, Wilfried Sigle, and Peter A. van Aken

Components: 2 Figures

Figure S5.1: Bright-field transmission electron microscope (TEM) image of the six-fold torus.

Figure S5.2: Near-field intensity profiles.

A bright-field transmission electron microscopy (TEM) image of the investigated structure is displayed in figure S5.1. The structure consists of 7 holes with circular shape drilled onto a free-standing silver film. Their diameters of the holes and the thickness of the silver film are 60 nm, both. The holes were drilled by using a focused ion beam (FIB) instrument (FEI Nova NANOLAB) at 30 kV. The silver film region which is left between the central and surrounding holes behaves like a torus. Therefore it enables the possibility to observe the toroidal resonances by using an electron beam in the optical wavelength region as it is discussed in detail in chapter 5.

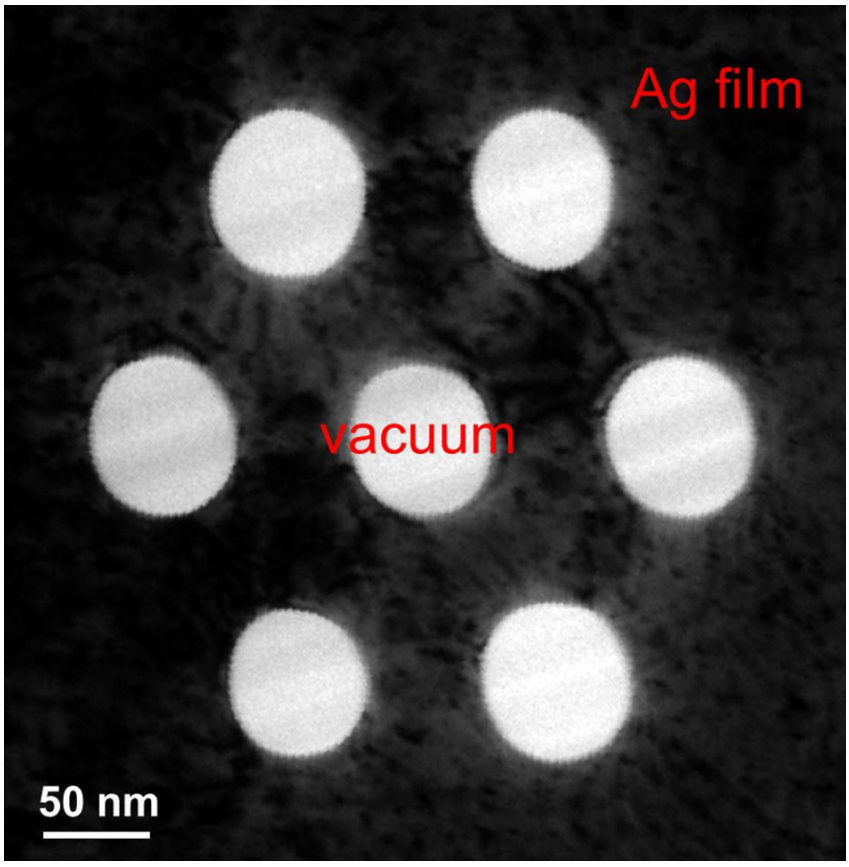

Figure S5.1: Bright-field transmission electron microscope (TEM) image of the oligomer structure consisting of seven holes with six-fold symmetry, drilled into a free-standing silver (Ag) film by a focused ion beam (FIB).

The eigenmodes observed experimentally at 2.5 eV and 3.7 eV (figure 2), have been confirmed to have a toroidal character by 3D-FDTD simulations. An electric dipole excitation was placed in the central hole of the heptamer structure (figure S5.1). The resulting alignments of the electric and magnetic field vectors verify the toroidal character at energy loss values of 2.5 eV and 3.7 eV, as shown in figure 5 in chapter 5. In order to verify the toroidal behaviour the near field intensity profile has been drawn as displayed in figure S5.2. The intensity profiles belong to the electromagnetic behaviour just above the structure. The modes denoted as T1, T2, QR, DA and DR correspond to the first and second toroidal, quadrupolar, dipolar radial and dipolar azimuthal mode, respectively. The corresponding energy values are in perfect agreement with the experimental results.

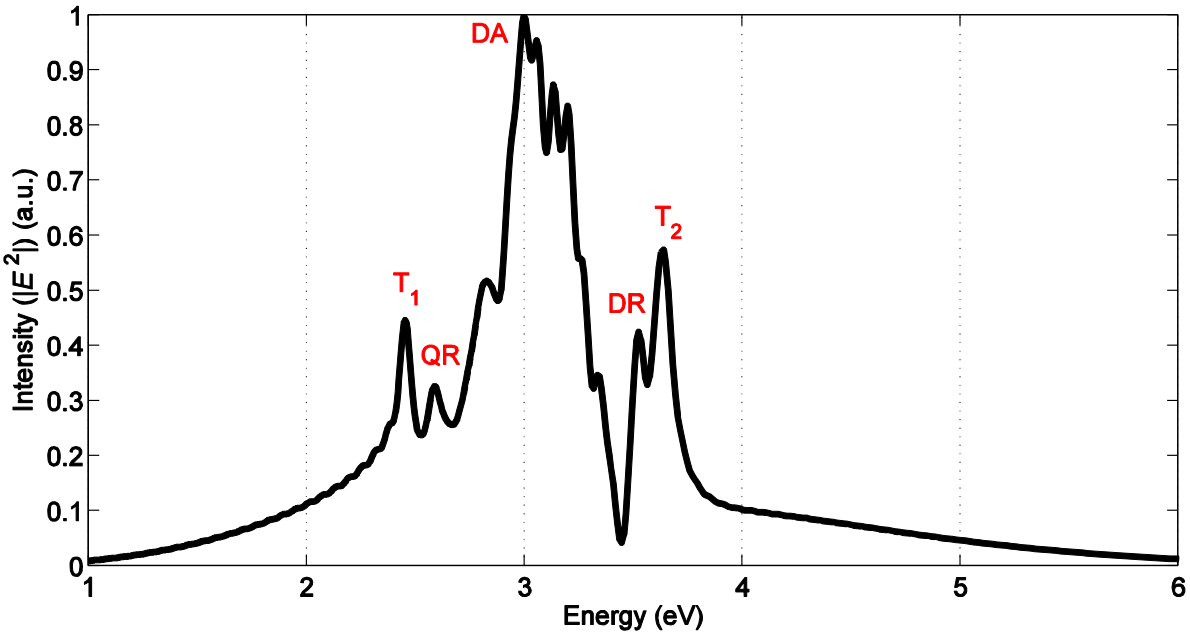

Figure S5.2: Near-field intensity profiles as calculated by FDTD.
Normalized near-field intensity of the electric field just above the structure, when it is excited with an electric dipole located at the central hole. Several resonances of the structure are clearly discernible: T1 and T2 are the first and second toroidal modes, QR and DR stand for quadrupolar and dipolar radial modes, respectively, and DA stands for dipolar azimuthal mode.

CHAPTER 6

Visualization of Plasmonic Eigenmodes in Hexamer and Pentamer Nanocavities

Burcu Ögüt[1], Nahid Talebi[1], Ralf Vogelgesang[2], Wilfried Sigle[1], and Peter A. van Aken[1]

1. Max Planck Institute for Intelligent Systems, Heisenbergstraße 3, 70569, Stuttgart, Germany
2. Max Planck Institute for Solid State Research, Heisenbergstraße 1, 70569, Stuttgart, Germany

Manuscript 2012

Corresponding author: ogut@is.mpg.de

The changes in the plasmonic behaviours of oligomer nanocavities were studied by modifying the number of surrounding holes or the central hole. The EFTEM experiments were performed by Burcu Ögüt and FDTD simulations were conducted by Nahid Talebi. All of the co-authors have contributed to the interpretation of the experimental and simulation results.

Abstract

Plasmonics, which is expected to play one of the leading roles in nanotechnology, has been offering fascinating alternatives in engineering and medical science nowadays. Most of the plasmonic phenomena are governed by the electric and magnetic resonances. Toroidal resonances have been discovered to be another candidate for innovating plasmonic devices in the optical wavelength regime via the investigations of plasmonic heptamer nanocavities. In this chapter, the toroidal resonances have been analyzed further in oligomeric hexamer and pentamer nanocavities using energy-filtering transmission electron microscopy (EFTEM) supported with three-dimensional finite-difference time-domain simulations (3D-FDTD) at optical wavelengths. As discussed throughout the chapter, using an electron beam is the only way to excite these optically ultra-dark modes. Changing the number of the surrounding holes and the disappearance of the central hole has significant effects on the toroidal character. Even if the central hole is removed, the toroidal resonances are still visible in 3D-FDTD simulations as well as in the experimental EELS spectra, however these modes are weaker.

6.1. Introduction

Plasmonics has become a popular field of research after it was realized that light could actually be trapped into very small sizes at the nanoscale, which has opened different avenues in the various fields of nanoscience, such as, electronics, biology, and solar cell applications.[1]

Since this discovery, a lot of research has been done on metallic structures having different geometric shapes like triangles[2], rods[3,4], stars[5]…etc. In addition, the electromagnetic coupling phenomena of the closely spaced structures have been studied in the framework of plasmonic hybridization theory[6] with optical[7] or electron microscopy[8] techniques. Among these techniques, EELS[9] and EFTEM[10] are superior compared to the methods that use light. These two techniques are capable of capturing the optically dark plasmonic eigenmodes by using fast electron beam excitation.[11]

A toroidal plasmonic eigenmode, being a nearly radiation-free and optically ultra-dark mode, is a perfect example for this situation. A toroidal plasmon resonance is characterized by a magnetic field current creating a closed loop in azimuthal direction, and an electric field current whirling in radial direction.[12] This situation is analogous to electromagnetic fields of a toroid in the macroscale, which is a proof of Ampere's law[13]. Kaelberer[14] et al could show the occurence

of toroidal resonances in the microwave region for the first time. The existence of toroidal resonances in the optical wavelength region could be proven in our previous publication (chapter 5), where a plasmonic oligomer nanocavity system which is composed of seven circular nanoholes arranged in heptamer configuration was analyzed.[15]

Previously, there have been several publications about different aspects of nanoparticles arranged in oligomeric configuration by application of optical microscopy techniques.[16-18] Optical techniques could show the optically dark modes only via Fano resonances.[19] Fano resonances are the indirect manifestations of optically dark modes due to the reason that they occur with the destructive interference of bright and dark resonances.[20] The effect of central particle removal or changes in the number of surrounding particles on Fano resonances were studied comprehensively.[21]

The same concept has been applied on the nanocavity oligomers in this chapter. The motivation is to understand how the toroidal plasmonic eigenmode behaviour is modified in different oligomer configurations (hexamer or pentamer configurations) created by changing the number and arrangement of holes in the oligomer system from the results of EFTEM experiments combined with 3D-FDTD simulations.

6.2. Materials & Methods

Specimen preparation: The recipe described in another reference[22] has been used to electropolish the punched Ag discs having 3 mm diameter at Struers Tenupol until a hole was visible at the center at Struers-Tenupol 5. Voltage, beam current and light sensitivity values were set as 4 V, 25 mA, and 100. Subsequently, a FIB instrument (FEI Nova Nano Lab) was used in order to drill three sets of holes in pentamer and hexamer configuration into Ag films, respectively. Low-angle ion milling and polishing system (FISCHIONE Instruments-Model 1010) was used for final thinning and cleaning. The experimental conditions that have been applied for electropolishing, drilling holes, and final ion milling are the same as those having been specified in the previous chapter. The final thicknesses of the films around pentamer and hexamer structures are ca. 60 ± 10 nm, and 70 ± 10 nm, respectively, which have been measured by the log-ratio method (see chapter 2 for the details of this method). The TEM bright field-images of the prepared specimens are depicted in figure 6.1.

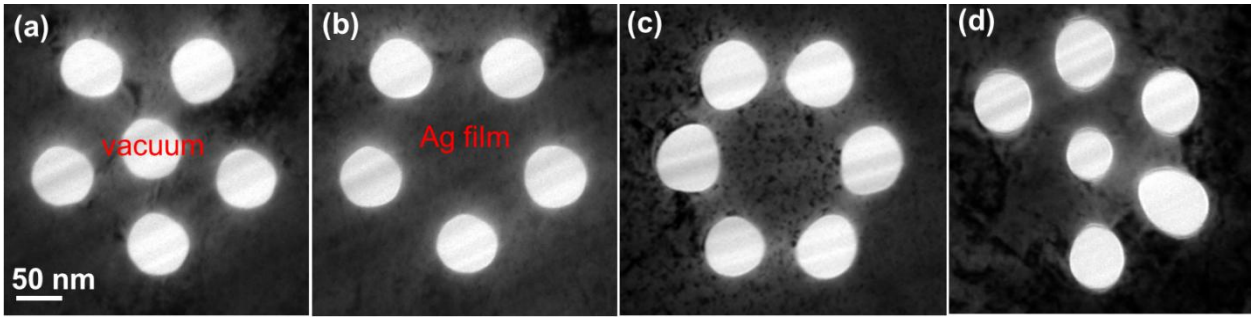

Figure 6.1: Bright-field transmission electron microscope (TEM) images of the (a) five-fold hexamer with central hole, (b) five-fold pentamer, (c) six-fold hexamer without central hole, (d) hexamer nanocavity structure formed by removing one surrounding hole from the heptamer nanocavity system discussed in chapter 5. The images show the collection of holes with cyclic symmetry, drilled on a free-standing silver (Ag) film by a focused ion beam (FIB). The scale bar is valid for all images.

Experimental procedure: EFTEM experiments were performed in the Zeiss SESAM[23,24]in the energy-loss interval of 0–7 eV, starting from high energy going down to lower energies in order to minimize afterglow effects of the CCD camera. During the experiment both, the energy-filter and monochromator slits had a width of 0.2 eV. The other experimental conditions were identical to the conditions previously explained in chapter 5. Afterwards, PCA analysis has been applied on the acquired data using 14 components for the case of the five-fold hexamer with central hole, using 9 components for the case of the six-fold hexamer without a central hole and of the pentamer structures, and using 11 components for the hexamer structure formed by removing one surrounding hole from the heptamer nanocavity system. The decision on the number of components was taken according to the situation where one could get the highest amount of information with the least amount of noise. As there is no proper background subtraction function for the energy-loss region that was studied, a peak mapping algorithm was written to uncover the hidden eigenmodes in the EFTEM images.

Simulation Procedure: The 3D-FDTD simulations were performed by using a Huygens source, where a Ricker wavelet was introduced for this purpose 500 nm above the structures. Yee's meshes had 2 nm edge size in order to discretize the structure. Near-field simulations were achieved by either placing an electric dipole only into the central hole in the case of six-fold hexamer, and into all of the existing holes for the case of the pentamer and six-fold hexamer structures.

6.3. Results & Discussion

Using an electron beam is advantageous in plasmonics research in terms of exciting eigenmodes having different characteristics all at once. The so obtained eigenmodes excited can be excited with optical techniques only under specific geometries, such as near-field excitation or far-field excitation with different polarizations (e.g. azimuthal and radial) (figure 5.1). It was already proven that a heptamer nanocavity system sustains a toroidal mode.[15] Here, changes in the toroidal, azimuthal, radial mode behaviours are investigated by either changing the number of surrounding holes or removing the central hole from the oligomer nanocavity system and applying EFTEM imaging combined with 3D-FDTD simulations.

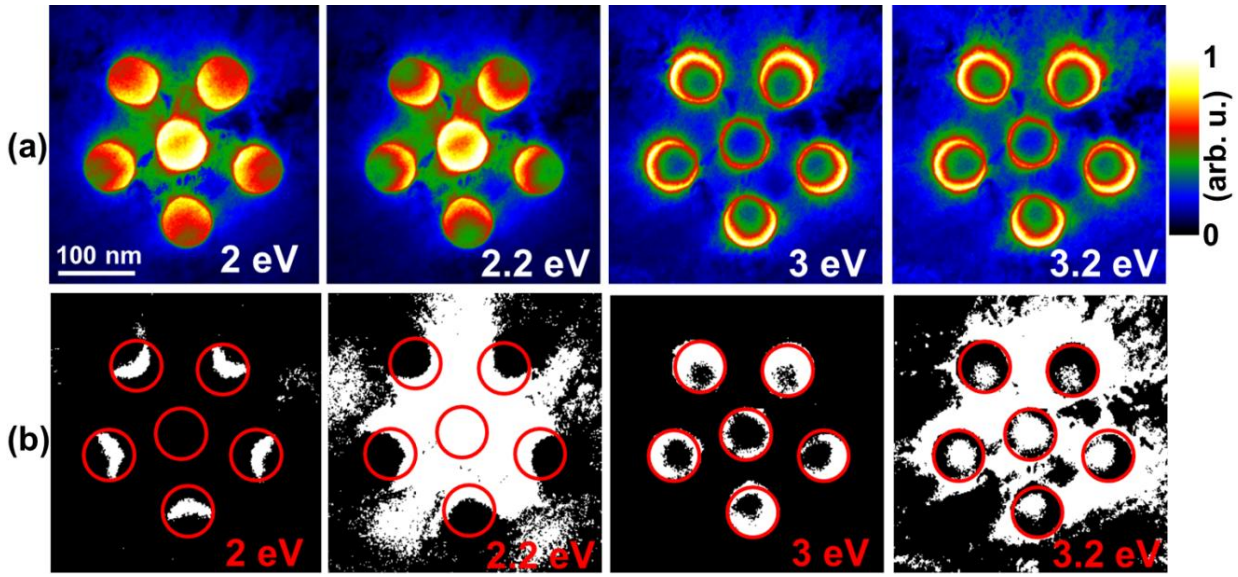

Figure 6.2: (a) Collection of plasmonic eigenmodes acquired with EFTEM imaging, and (b) the peak maps obtained from the acquired images at energy losses of 2 eV, 2.2 eV, 3 eV, and 3.2 eV of the five-fold hexamer. The scale bar applies to all images. The red circles in (b) indicate the positions of the holes.

Discussions of the results start with investigations of five-fold hexamer system (figure 6.2) formed by decreasing the surrounding hole number from 6 to 5. The EFTEM images (figure 6.2a) and the peak maps (figure 6.2b) prove that all of the modes previously observed in a heptamer structure are preserved in a five-fold hexamer nanocavity system, too (figure 5.2). The eigenmode captured at 2.2 eV is the hybridization of the toroidal mode (figure 5.5) and azimuthal mode (figure 5.4) that have been previously observed in a heptamer system. The term azimuthal mode refers to the plasmonic eigenmode where electric and magnetic field vectors are

whirling in the azimuthal and radial direction, respectively Furthermore, the electromagnetic field concentration is at the outer rim of the surrounding holes at 3 eV, which is a sign that the electric field is aligned in the radial direction like the condition previously observed in our previous publication[15]. The peak map observed at 3.2 eV is nearly the same as the situation observed at 3.6 eV in heptamer oligomers, which gives a hint about toroidal mode behaviour.

Removal of one surrounding hole without modifying the positions of the remaining holes leads neither to a breakdown of the toroidal modes nor to a collapse of the azimuthal or radial modes (figure 6.3). The peak map (figure 6.3b) that was obtained from the EFTEM image (figure 6.3a) at 2.2 eV shows that the electromagnetic field concentration is high at the silver film left between the central and surrounding holes giving a hint for a toroidal mode. At 2.6 eV, the intensity maxima are high at the rims of the surrounding holes. The mode at 3.2 eV shows that the intensity is highest at the outer rims of the surrounding holes which is a sign that the electric field vectors are aligned in the radial direction.

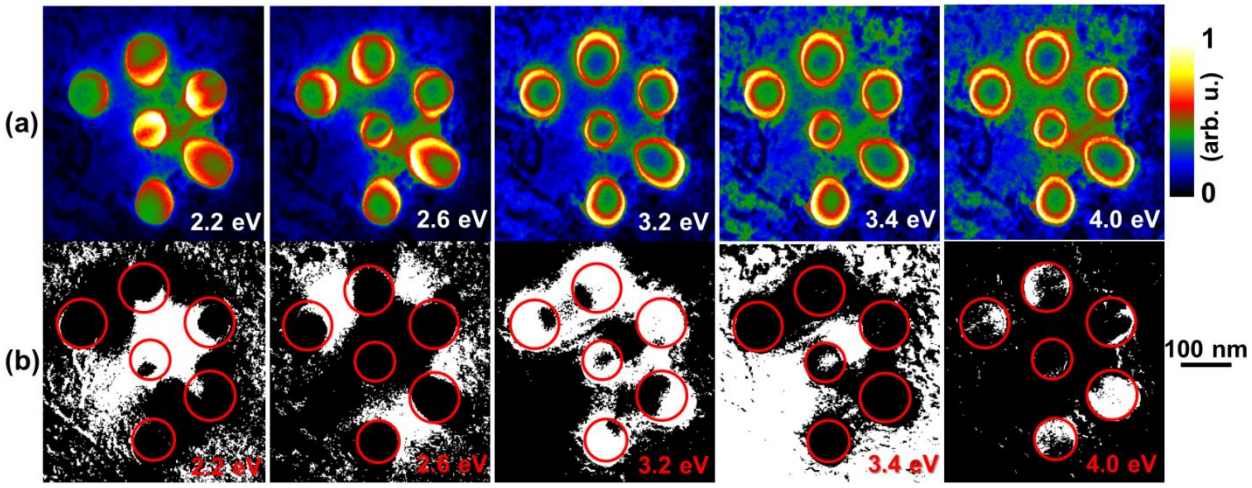

Figure 6.3: (a) Collection of plasmonic eigenmodes acquired with EFTEM imaging, and (b) the peak maps obtained from the acquired images at energy losses of 2.2 eV, 2.6 eV, 3.2 eV, 3.4 eV, and 4 eV after removal of one surrounding hole from the heptamer nanocavity system. The scale bar applies to all images. The red circles in (b) indicate the positions of the holes.

The 3D-FDTD simulations (figure 6.4) approve the EFTEM investigations (figure 6.3). Figure 6.4a shows the modulus of the z component of the electric field ($|E_z|$), and figures 6.4b to 6.4f show the real component of the electric field at energy losses of 2.6 eV, 3.1 eV, 3.6 eV, 3.8 eV, and 4.1 eV. The modes observed at 2.6 eV, 3.1 eV, and 3.6 eV were calculated with exploitation of azimuthally polarized far-field radiation, radially polarized far-field radiation, and

near-field radiation by placing a dipole into the central hole, respectively. The result of azimuthal polarization leads to a ring resonator behaviour as shown figure 6.4b, where the electric field vectors are running in azimuthal direction. Opposite charges are accumulated on the rims of the surrounding holes indicated by red (plus charge) and blue colours (minus charge) in perfect agreement with the mode observed at 2.6 eV in EFTEM images (figure 6.3). The mode observed at 3.1 eV has been calculated with radially polarized far-field excitation (figure 6.4c). In the resulting simulated eigenmode the electric field is concentrated at the outer rims of the surrounding holes, meaning that electric field vectors are pointing in the radial direction. The other simulated images from 3.6 eV-4.1 eV were excited with near-field radiation by inserting a dipole into the central hole (figure 6.4 d-f). All of these modes possess a toroidal character, but the modes that were simulated at energy loss values of 3.8 eV and 4.1 eV could not be totally approved by the EFTEM images, since the volume plasmon gets dominant at this energy region.

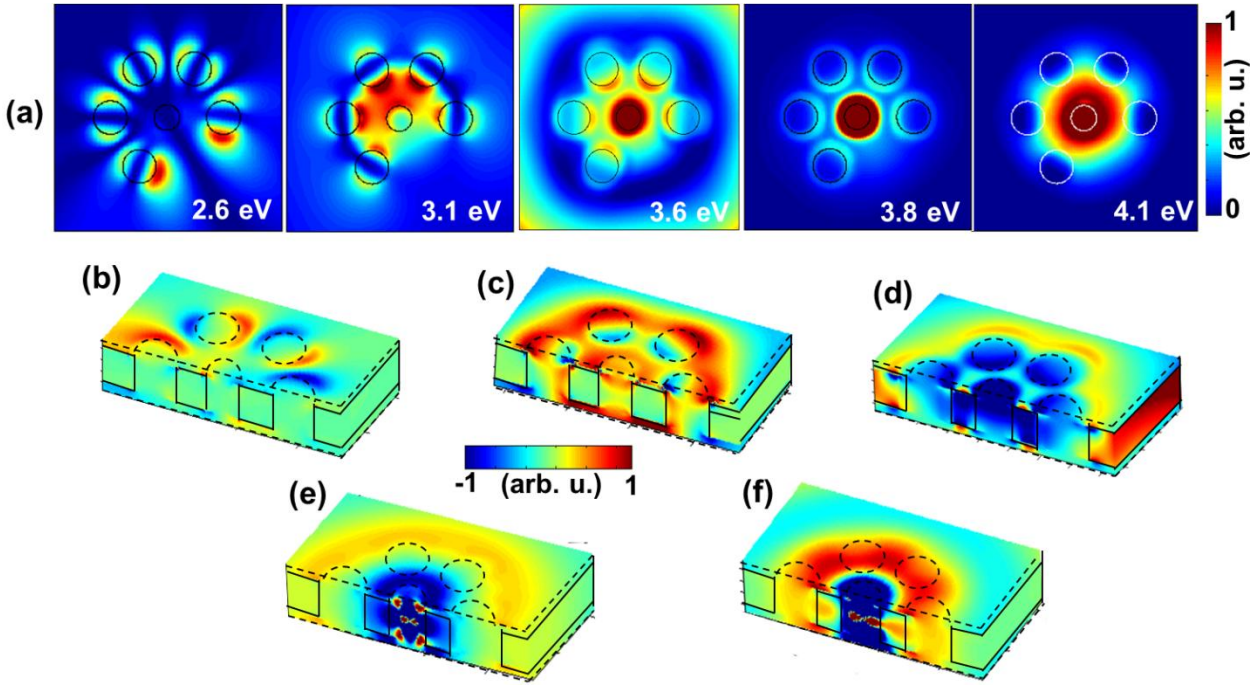

Figure 6.4: The simulated modes with FDTD. (a) the modulus of the electric field ($|\boldsymbol{E_z}|$) at 2.6 eV, 3.1 eV, 3.6 eV, 3.8 eV, 4.1 eV, and the real component of E_z simulated at energy loss values of (b) 2.6 eV, (c) 3.1 eV, (d) 3.6 eV, (e) 3.8 eV, and (f) 4.1 eV.

From this point on, the discussions of the results proceed with the examination of central hole's role on the appearance of plasmonic eigenmodes having toroidal, azimuthal, and radial nature. Figure 6.5 displays how the plasmonic eigenmode behaviour is modified when the central

hole is removed while keeping the number of surrounding holes unchanged. From EFTEM images (figure 6.5a) and peak maps (figure 6.5b), it is visible that the electromagnetic field strength is concentrated at the center. At energy loss values of 2.6 eV and 2.8 eV, the intensities are high between the surrounding holes, which conveys that they couple with each other in the azimuthal direction. Moreover, the electromagnetic field gets concentrated at the outer rims at 3.4 eV energy loss.

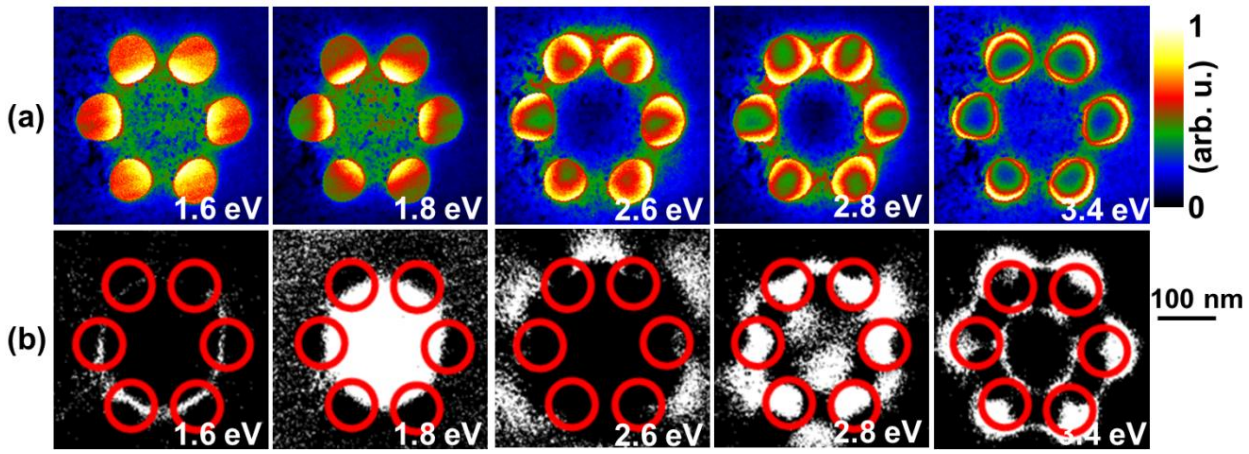

Figure 6.5: (a) Collection of plasmonic eigenmodes acquired with EFTEM, and (b) peak maps at energy losses of 1.6 eV, 1.8 eV, 2.6 eV, 2.8 eV, and 3.4 eV of the six-fold hexamer. The scale bar applies to all images. The red circles in (b) indicate the positions of the holes.

The 3D-FDTD simulation results exhibit the absolute and real components of E_z in figures 6.6.a and figure 6.6.b, respectively. The eigenmode captured at 1.8 eV energy loss shows that the electric field is maximized in the inner rims of the holes and the central part of the structure. The modes observed at 2.7 eV and 2.9 eV were simulated by applying an azimuthally polarized far-field radiation source. The electric field vectors whirl in the azimuthal direction in both cases. The difference between these two modes is based on the electrical charge distribution. At 2.9 eV the structure behaves like a ring resonator which gives an antisymmetric electrical charge distribution. Differently, at 2.7 eV the electric field vectors flip their sign during the tour around and give a symmetric behaviour with respect to plane a, and an antisymmetric behaviour with respect to plane b, as shown in figure 6.6 b. In the case of the mode simulated at 3.4 eV energy loss, a radially polarized far field excitation source was exploited. The electromagnetic field strength is high in the inner and outer rims of the holes, which proves that

electric field vectors are pointing in the radial direction. The eigenmode which has been simulated at 3.8 eV could not be seen in the experiments as the bulk plasmon mode is dominant at this energy region around 3.8 eV. Actually, it is the longitudinal current in z direction, which gives rise to the toroidal moments at around 3.8 eV. These toroidal moments are basically the volume plasmons that are excited inside the metal around the central hole in figure 6.4, 6.6, and figure 5 of previous chapter. Therefore, independent from the configuration of the holes, this mode is always observed at 3.8 eV, which is the volume plasmon energy for silver.

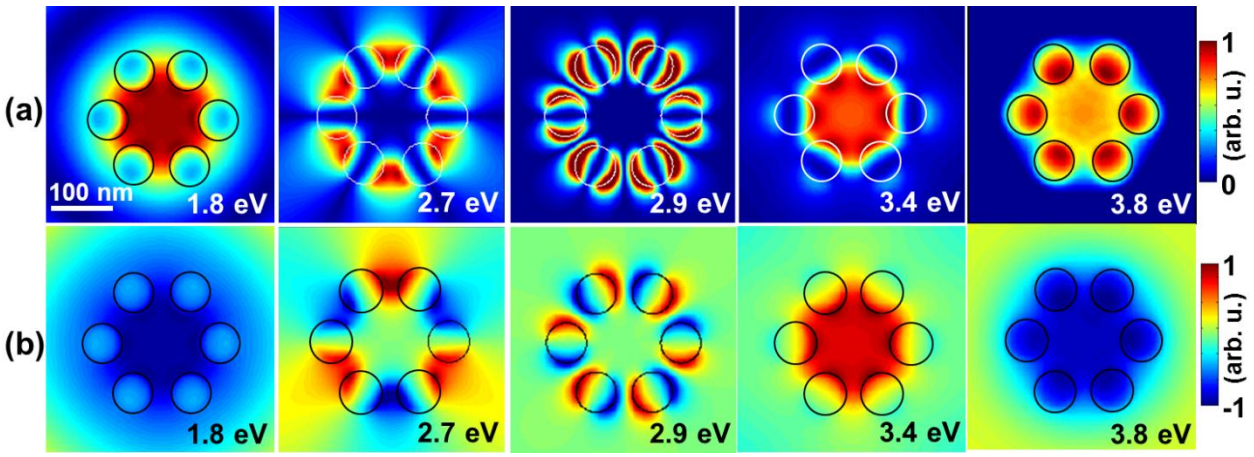

Figure 6.6: The simulated images using FDTD simulations showing (a) the $|\boldsymbol{E_z}|$ modulus and (b) the real component of E_z for a six-fold hexamer for the energies indicated in the figure. The scale bar is valid for all images.

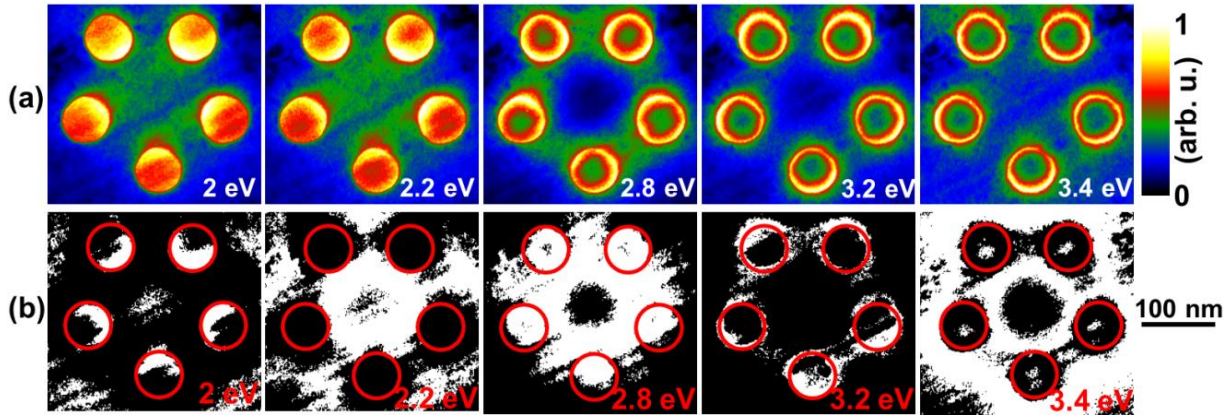

Figure 6.7: (a) Collection of plasmonic eigenmodes acquired with EFTEM, and (b) peak maps at energy losses of 2 eV, 2.2 eV, 2.8 eV, 3.2 eV, and 3.4 eV of the five-fold pentamer. The scale bar applies to all images. The red circles in (b) indicate the positions of the holes

In figure 6.7, the total number of holes is decreased from six to five. The experimental results of the pentamer nanocavities (figure 6.7) are similar to the experimental results on the

hexamer nanocavities (figure 6.5). From this, one can conclude that changing the number of surrounding holes has smaller effect on the observed eigenmodes compared to the appearance/disappearance of the central hole.

The FDTD simulations for the pentamer structure (figure 6.8) shows similar behaviour but the mode that has been observed at 2.7 eV in figure 6.6 is impossible to excite in the pentamer structure due to symmetry reasons. The same situation holds for the structure shown in figures 6.3 and figure 6.4 as well. The hexamer structure (figure 6.5 & 6.6) has six symmetry planes but whereas the pentamer structure has only five symmetry planes as displayed with a dashed line in figure 6.8b. Therefore it is not possible to excite such an electromagnetic field configuration in pentamer nanocavities.

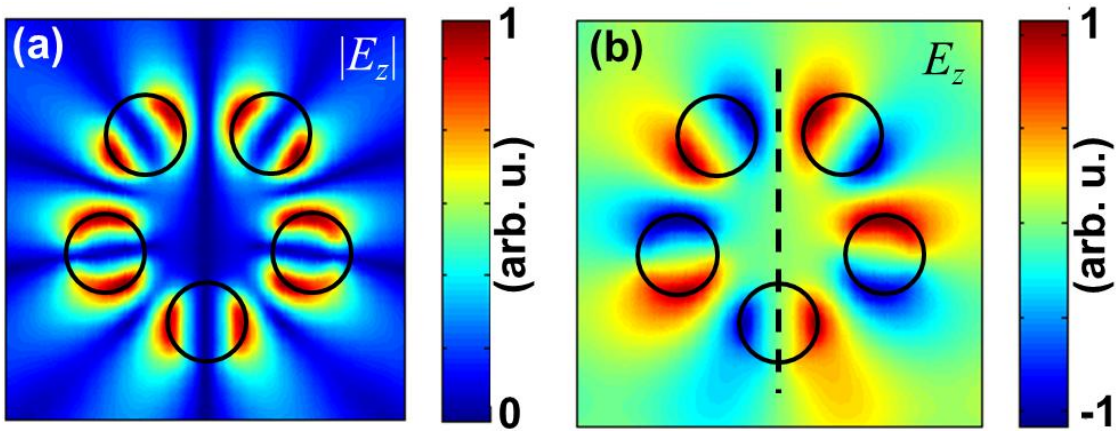

Figure 6.8: The simulated images using FDTD simulations showing (a) the $|E_z|$ modulus and (b) the real component of E_z for a five-fold pentamer for the energy loss values indicated in the figure. The scale bar is valid for all images.

Figure 6.9 gives a brief summary about the plasmonic behaviour in heptamer (structure i), hexamer (structure ii), five-fold hexamer (structure iii), and pentamer (structure iv) nanocavity systems by extracting EELS spectra from the positions marked as 1, 2, 3, and 4 on these four structures. Figures 6.9a compares the EELS spectra extracted from the positions marked as 1 in the four structures. The energy loss peaks observed at 2.4 eV (structure i), 1.8 eV (structure ii), 2.2 eV (structure iii & iv) correspond to the toroidal contribution. It can be observed that when the central hole is removed (structure ii and iv), the intensity of the plasmon peak is much lower compared to the cases when the central holes exist (structures i and iii). From this behaviour one can conclude that removal of the central hole plays a big role in the decrease of the toroidal mode strength. The additional secondary peaks that appear around 3.5 eV belong to the toroidal

contribution as well, but the peaks corresponding to structures ii and iv are much weaker in comparison to the others. This second toroidal eigenmode was imaged only in heptamer and five-fold hexamer structures, where the central hole exists. In hexamer and pentamer structures this mode was not observed in the EFTEM image series at around these energy loss values.

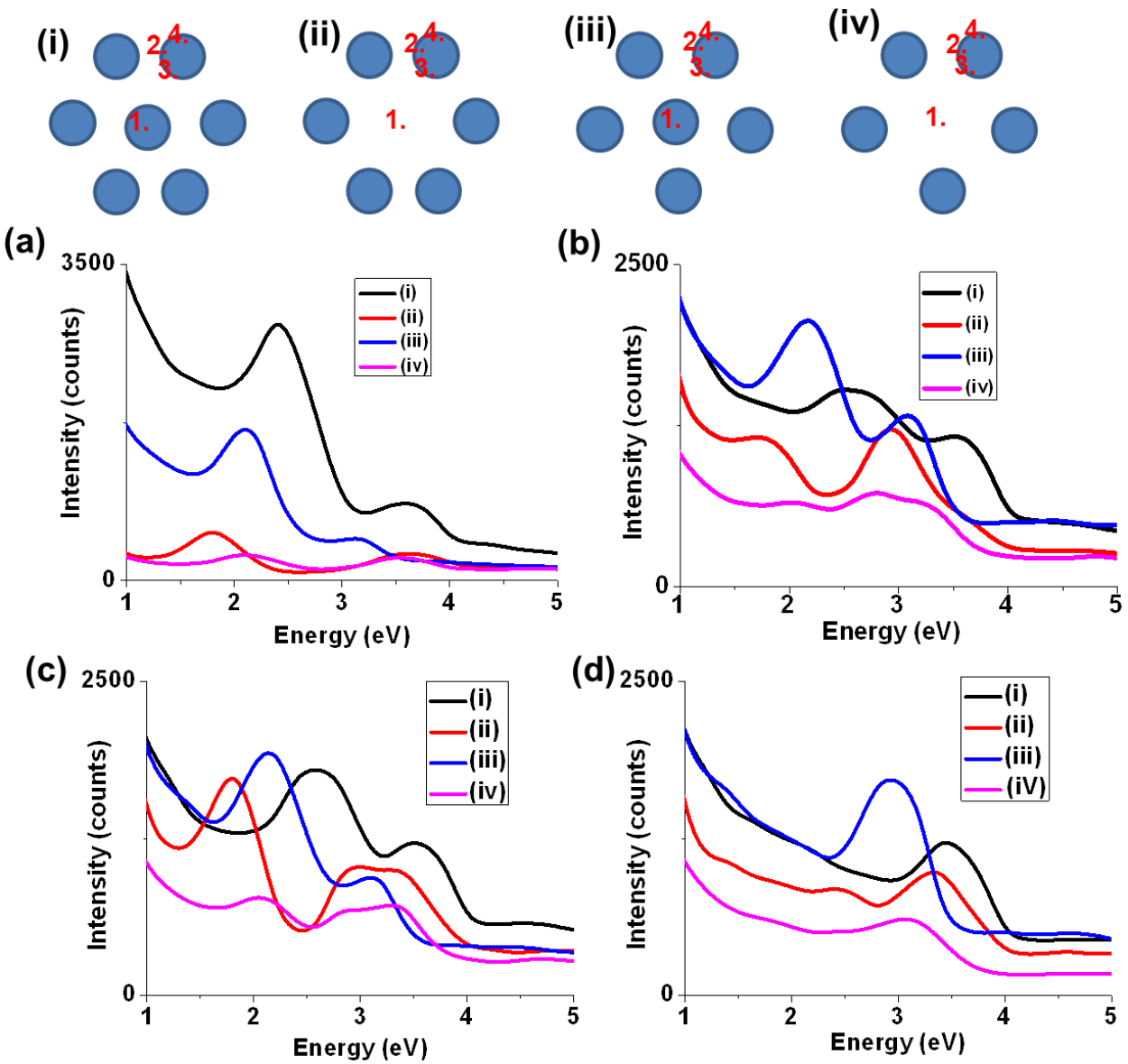

Figure 6.9: EELS spectra extracted from EFTEM data cube of the heptamer, hexamer, five-fold hexamer, and pentamer nanocavity systems. The EELS spectra in (a), (b), (c), and (d) correspond to the spectra extracted from the positions marked 1, 2, 3, and 4, respectively in the four structures (i) to (iv).

Figure 6.9b compares the EELS spectra extracted from the positions marked with number 2 at the rims of the surrounding holes of the four structures illustrated in figure 6.9. As it was

previously shown, the surrounding holes couple with each other for the azimuthal polarization condition. Therefore, the peaks that are observed in the EELS spectra from these positions are attributed to azimuthal modes. The peaks that are observed at around 3 eV are showing the azimuthal contribution. The effect of the toroidal modes (maxima at around 2 eV) and the radial modes (maxima at around 3.5 eV) are still visible.

The EELS spectra extracted from position 3 (figure 6.9c) show both the toroidal and radial contribution. As it was previously explained, toroidal modes are characterized by the electric field vectors whirling in the radial direction at the cross section of the oligomer system causing a coupling between the central hole and surrounding holes, where electromagnetic field maxima are visible in the central hole and inner rims of the surrounding holes. In the case of the radial contribution, intense field maxima are observed in the inner and outer rims of the surrounding holes. The energy loss positions of the first peaks observed in figure 6.9c are nearly the same as the ones that are observed in figure 6.9a, which could indicate that they might be belonging to the toroidal mode contribution. The second peaks that are between 3 eV and 3.5 eV belong to the radial contribution, which are approved by the EELS spectra shown in figure 6.9 d belonging to purely radial contribution.

6.4. Conclusions

The role of the central and surrounding holes on the plasmonic mode formation in an oligomer nancavity system was systematically studied. It has been shown that the plasmonic eigenmode behaviour can be manipulated by varying the configuration and number of holes. It has been realized that the central hole acts partly like a switch on/off button for the toroidal modes, as the toroidal mode strength decreases significantly when the central hole vanishes. In addition, as long as the central hole exists, the toroidal mode is preserved independent of the number or configuration of the surrounding holes. Using this information retrieved from this study, devices based on these oligomer nanocavities can be produced for biosensing purposes[25]. In addition, structures produced in three dimensions can find application areas in solar cell technology[26] and Fano engineering[27].

Acknowledgements

We thank U. Eigenthaler and I. Lakemeyer for the support during the specimen preparation, C.T. Koch for writing the scripts regarding EFTEM acquisition and peak finding algorithm. N. Talebi gratefully acknowledges the Alexander-von-Humboldt foundation for financial support.

References

1. Ozbay, E. Plasmonics: Merging photonics and electronics at nanoscale dimensions, *Science*, **311**, 189-193, (2006).
2. Nelayah, J.; Kociak, M.; Stephan, O.; Garcia de Abajo, F.J.; Tence, M.; Henrard, L.; Taverna, D.; Pastoriza-Santos, I.; Liz-Marzan, L.M.; Colliex, C. Mapping plasmons on a single metallic nanoparticle, *Nat. Phys.* **3**, 348-353, (2007).
3. Alber, I.; Sigle, W.; Müller, S.; Neumann, R.; Picht, O.; Rauber, M.; van Aken, P.A.; Toimil-Molares, M.E. Visualization of multipolar longitudinal and transversal surface plasmon modes in nanowire dimers, *ACS Nano*, **5**, 9845-9853, (2011).
4. Rossouw, D.; Couillard, M.; Vickery, J.; Kumacheva, E.; Botton, G.A. Multipolar plasmonic resonances in silver nanowire antennas imaged with a subnanometer electron probe, *Nano Lett.* **11**, 1499-1504, (2011).
5. Hao, F.; Nehl, C.L.; Hafner, J.; Nordlander, P. Plasmon resonances of a gold nanostar, *Nano Lett.*, **7**, 729-732, (2007).
6. Prodan, E.; Radloff, C.; Halas, N.J.; Nordlander, P. A hybridization model for the plasmon response of complex nanostructures, *Science*, **302**, 419-422, (2003).
7. Nordlander, P.; Oubre, C.; Prodan, E.; Li, K.; Stockman, M.I. Plasmon hybridization in nanoparticle dimers, *Nano Lett.* **4**, 899-903, (2004).
8. Koh, A.L.; Bao, K.; Khan, I.; Smith, W.E.; Kothleitner, G.; Nordlander, P.; Maier, S.; McComb, D.W. Electron energy-loss spectroscopy of surface plasmons in single silver nanoparticles and dimers: influence of beam damage and mapping of dark modes, *ACS Nano*, **3**, 3015-3022, (2009).
9. Batson, P.E. Surface plasmon coupling in clusters of small spheres, *Phys. Rev. Lett.* **49**, 936-940, (1982).
10. Sigle, W.; Nelayah, J.; Koch, C.T.; van Aken, P.A. Electron energy losses in Ag nanoholes-from localized surface plasmon resonances to rings of fire, *Opt. Lett.*, **34**, 2150-2152, (2009).
11. Garcia de Abajo, F.J. *Rev. Mod. Phys.* **82**, 209-275 (2010).
12. Dubovik, V.M.; Tugushev, V.V. Toroid moments in electrodynamics and solid-state physics, *Phys. Rep.* **187**, 145-202, (1990).
13. Jackson, J.D. *Classical Electrodynamics*, 1999, John Wiley & Sons, New Jersey.

14. Kaelberer, T., Fedotov, V. A.; Papasimakis, N.; Tsai, D.P.; Zheludev, N.I. Toroidal dipolar response in a metamaterial, *Science* **330**, 1510-1512, (2010).
15. Ögüt, B.; Talebi, N.; Vogelgesang, R.; Sigle, W.; van Aken, P. A. Toroidal plasmonic eigenmodes in oligomer nanocavities for the visible, *Nano Lett.*, **12**, 5239-5244, (2012).
16. Hentschel, M.; Saliba, M.; Vogelgesang, R.; Giessen, H.; Alivisatos, A.P.; Liu, N. Transition from isolated to collective modes in plasmonic oligomers, *Nano Lett.* **10**, 2721-2726, (2010).
17. Fang, Z.; Wang, Y.; Liu, Z.; Schlater, A.; Ajayan, P.M.; Koppens, F.H.L.; Nordlander, P.; Halas, N.J. Plasmon induced doping of graphene, *ACS Nano* **6**, 10222-10228, (2012).
18. Pasquale, A.J.; Reinhard, B.M.; Dal Negro, L. Engineering photonic-plasmonic coupling in metal nanoparticle necklaces, *ACS Nano*, **5**, 6578-6585, (2011).
19. Rahmani, M.; Luk'yanchuk, B.; Hong, M. Fano resonance in novel plasmonic nanostructures, Laser & Photon. Rev. Doi: 10.1002/lpor.201200021.
20. Luk'yanchuk, B.; Zheludev, N.I.; Maier, S.A.; Halas, N.J.; Nordlander, P.; Giessen, H.; Chong, C.T.; The fano resonance in plasmonic nanostructures and metamaterials, *Nature Mater.* **9**, 707-715, (2010).
21. Hentschel, M.; Dregely, D.; Vogelgesang, R.; Giessen, H.; Liu, N. Plasmonic oligomers: the role of individual particles in collective behaviour, *ACS Nano*, **5**, 2042-2050, (2011).
22. Lyles Jr, R. L.; Rothman, S. J.; Jäger, W. A cyanide free solution for electropolishing silver, *Metallography* **11**, 361-363, (1978).
23. Koch, C. T.; Sigle, W.; Höschen, R.; Rühle, M.; Essers, E.; Benner, G.; Matijevic, M. SESAM: Exploring the frontiers of electron microscopy, *Microsc. Microanal.* **12**, 506-514, (2006).
24. Essers, E.; Benner, G.; Mandler, T.; Meyer, S.; Mittmann, D.; Schnell, M.; Höschen, R. Energy resolution of an Omega-type monochromator and imaging properties of the MANDOLINE filter, *Ultramicroscopy* **110**, 971-980, (2010).
25. Eftekhari, F.; Escobedo, C.; Ferreira, J.; Duan, X.; Girotto, E.M.; Brolo, A.G.; Gordon, R.; Sinton, D. Nanoholes as nanochannels: flow-through plasmonic sensing, *Anal. Chem.* **81**, 4308-4311, (2009).
26. Vahala, K.J. Optical microcavities, *Nature* **424**, 839-846, (2003).

27. Miroshinichenko, A. E.; Kivshar, Y. S. Engineering fano resonances in discrete arrays, *Phys. Rev. E* **72**, 056611, (2005).

CHAPTER 7

EFTEM Study of Surface Plasmon Resonances in Silver Nanoholes

Wilfried Sigle, Jaysen Nelayah, Christoph T. Koch, Burcu Ögüt, Lin Gu, Peter A. van Aken

Max Planck Institute for Intelligent Systems, Heisenbergstraße 3, 70569, Stuttgart, Germany

Using energy-filtering transmission electron microscopy localized plasmon resonances in nine nanoholes, six of which are arranged in a way forming a grape-like structure, referred to as a plasmonic grape, and three of which exist as single nanoholes, have been analyzed. The experimental results have been supported with DDSCAT simulations. Wilfried Sigle has performed the EFTEM measurements, and Jaysen Nelayah has performed the simulations using DDSCAT. All co-authors contributed to the data interpretation.

Ultramicroscopy 110 (2010) 1094–1100

Contents lists available at ScienceDirect

Ultramicroscopy

journal homepage: www.elsevier.com/locate/ultramic

EFTEM study of surface plasmon resonances in silver nanoholes

W. Sigle *, J. Nelayah, C.T. Koch, B. Ögüt, L. Gu, P.A. van Aken

Max Planck Institute for Metals Research, Heisenbergstraße 3, D-70569 Stuttgart, Germany

ARTICLE INFO

Keywords:
EFTEM
Surface plasmon resonances

ABSTRACT

Using energy-filtering transmission electron microscopy we observe localized plasmon resonances in nanoholes of silver. We find two resonances that are typical for single, isolated holes. A comparison with calculations based on the discrete dipole approximation shows that these are dipolar and quadrupolar resonances. In case of the close vicinity of holes we observe modes at lower energies that are ascribed to coupling effects between holes. We propose a hybridization scheme for the case of three collinear holes.

1. Introduction

The response of a dielectric medium to the influence of an electromagnetic wave or an electron is a polarization of the medium. On free surfaces this can lead to the excitation of surface plasmons (SPs) [1,2]. In the case of a spatially confined system SPs cannot propagate as on a free surface, but have to fulfill boundary conditions on the borders of the system. This leads to the formation of resonant eigenmodes which are associated with surface charges and electromagnetic fields surrounding the system. The strength and shape of this field not only strongly depends on particle shape and size, but also on the material. If nanoparticles approach each other, a coupling of the fields occurs leading to very strong field localization between the nanoobjects, so-called hot spots [3,4]. These effects are of great interest in the field of plasmonics where SPs are used for technological applications [5]. For example, single molecules can be detected by Raman spectroscopy if they are located in a hot-spot [4,6]. This is known as surface-enhanced Raman spectroscopy (SERS). In information technology SPs are of interest because the plasmon wavelength is well below the wavelength of light. By converting optical signals into SPs (and vice versa), information can therefore be transported on small length scales. For the design of such devices it is crucial to understand the SP behaviour, in particular techniques are required that allow visualization of SP fields on a nanometer scale. One such technique is scanning near-field-optical microscopy (SNOM) [7]. It has a spatial resolution of the order of a few 10 nanometers. As an optical technique it offers the advantage of being sensitive to the polarization direction of the exciting light. The 2-dimensional mapping of SPs by electron energy-loss spectroscopy (EELS) is a complementary technique, because it offers substantially better spatial resolution but is lacking the sensitivity on polarization. In fact, EELS techniques probe the local photonic density of states projected along the propagation direction of the fast electron [8]. EELS mapping of surface plasmons was pioneered by Batson [9] using a scanning transmission electron microscope (STEM). He made use of the good energy resolution offered by the cold field emitter of about 0.3 eV which is necessary for the detection of surface plasmon losses. Batson detected energy losses near Al spheres that were almost touching and ascribed them to the coupling of surface plasmons. Later on Wang and Cowley [10] and Ugarte et al. [11] performed STEM mapping of surface plasmons in Al and Si/SiO_2 particles, respectively. The recent success in synthesizing metallic nanoparticles has launched a series of papers showing surface plasmon mapping by EELS techniques. Some of the studies were performed in the STEM [12–14], but energy-filtering TEM (EFTEM) is now being used for this purpose as well [15–19]. The use of EFTEM for the study of SPs has become possible because the combination of Schottky field emitters with electron monochromators is now delivering a collimated electron beam with an energy resolution better than that achieved by cold field emitters. Excellent energy resolution is of paramount importance because surface plasmon energies are typically in the range of 0.5–4 eV in noble metals such as Au or Ag, i.e. the energy-loss features are superimposed on the strong tail of the elastic zero-loss peak. This tail is reduced in intensity by at least a factor of 1000 at an energy loss of 1 eV using monochromation. The two EELS techniques are again complementary in the sense that the STEM technique offers good spectral sampling whereas EFTEM allows a better spatial sampling. The latter is of particular importance for the study of complex structures because EFTEM gives an immediate view of

* Corresponding author.
E-mail address: sigle@mf.mpg.de (W. Sigle).

0304-3991/$ - see front matter © 2010 Elsevier B.V. All rights reserved.
doi:10.1016/j.ultramic.2010.03.009

the plasmonic resonances of large areas without additional data processing. Both EFTEM and STEM are sensitive to a wide range of energy losses, covering the whole range from infrared to far-UV. This is an advantage over optical methods, which are usually restricted to a rather limited energy range.

EELS measurements were only performed on nanoparticles till now. Here we use the complementary system of nanoholes in a free-standing Ag foil. This has the advantages that no substrate is used which can influence the SP resonance, and that nanoholes can be produced in very well-defined configurations which is usually not easy in the case of nanoparticles. Sub-wavelength-sized holes in thin films have recently been studied extensively by light-optical techniques triggered by the observation of abnormal transmission of light through periodic hole arrays [20,21]. In a recent report we showed a variety of SP resonances in a perforated Ag film using the EFTEM technique [19]. Here we report on a more detailed analysis of these resonances. First, we compare our experimental results of single holes with calculations based on the discrete dipole approximation (DDA) and we ascribe the hole resonances to dipolar and multipolar excitations. In a second step we apply the hybridization model in order to identify the eigenmodes of coupled holes to the experimentally observed eigenvalues. To the best of our knowledge this is the first time that this model is used for coupled nanoholes.

2. Experimental

2.1. Nanohole preparation

Silver of 6N purity was cold-rolled and annealed. After annealing the grain size of the polycrystalline sheet was several 100 μm. 3 mm diameter disks were punched out. The central part of the disks was electropolished until perforation using a Struers Tenupol. After transfer to a focused ion beam (FIB) instrument (FEI Nova NanoLab 600), 9 holes were drilled by the Ga ion beam at an accelerating voltage of 30 keV near the edge of the perforation. In this area the thickness of the Ag film was (100 ± 20) nm, i.e. the area was electron-transparent. The hole diameters are between 160 and 200 nm giving an aspect ratio of about 0.5–0.6. Influences of grain boundaries on the surface plasmon propagation [22] can be ignored since the grain size of the polycrystalline material is very large compared to the diameter of the holes. After FIB preparation the hole walls were found to be covered by a 13 nm thick amorphous carbon film. This contamination is assumed not to affect our spectroscopic results because carbon does not show spectral excitations below 5 eV [14,23]. However, the carbon film may cause an energy offset of several tenths electronvolts of the spectral features observed.

2.2. Transmission electron microscopy

The hole pattern was illuminated by a parallel electron beam in the Zeiss SESAM microscope [24]. This microscope incorporates the MANDOLINE filter [25,26], which creates a highly dispersive spectrum of energy losses suffered by the electrons when passing the specimen. Using a mechanical slit, a narrow energy range (0.2 eV) was selected and, using only these inelastically scattered electrons, an image is formed on a CCD detector. By varying the high tension of the TEM, the energy-loss range selected by the slit was varied from 0.4 up to 3.5 eV in steps of 0.2 eV. Recording an image for every energy-loss results in an EFTEM image stack. By using an objective aperture the maximum electron scattering angle was limited to 6 mrad. The acquisition time per image was 30 s. The images have a 256×256 spatial sampling ($8 \times$ binning of the 2048×2048 pixel CCD). One of the unique characteristics of the MANDOLINE filter is its excellent isochromaticity. This means that a large area, covering the entire 9-hole pattern, can be imaged with an energy-loss variation of less than 0.1 eV across the entire image area, even though the energy slit is narrow. The EFTEM image stack was analyzed within the DigitalMicrograph software (Gatan Inc., Pleasanton, USA). One of the advantages of the EFTEM technique is that shifts between individual images (caused by specimen drift) can easily be corrected with sub-pixel accuracy [27]. From the drift-corrected stack of inelastic images electron energy-loss spectra can be extracted from any user-defined area with an energy sampling corresponding to the energy-loss steps used for acquisition, which is 0.2 eV in our case. The thickness of the TEM foil was measured using the log-ratio method [28].

2.3. Calculations in the framework of the discrete dipole approximation

For the calculation we used the code DDSCAT 6.0 [29]. The applicability of this code for the interpretation of EELS results was recently reported by Geuquet and Henrard [30]. For the DDA calculations, three systems were considered with different thicknesses, t, of the Ag slab: 15, 30, and 60 nm, respectively. The hole diameter, D, of 100 nm was kept fixed. Note that the specimen thickness in the experiment was larger than the ones used in the calculations. Here we make use of the fact that the resonance energies scale with the aspect ratio t/D rather than with the absolute values of the thickness [31]. The total numbers of dipoles were 64 950, 133 300, and 2 690 400, respectively, which were found to be sufficient to make numerical error negligible. In the discrete dipole approximation, the studied nanosystem is replaced by a cubic arrangement of interacting dipoles and under an external linearly polarized electromagnetic excitation the local polarization of each elementary dipole can be determined. From the knowledge of the local polarizations, the global extinction, scattering and absorption of the nanosystem can be computed. The light wavelength was varied between 100 and 2000 nm. The character of the different modes was determined by plotting the amplitude and direction of the dipoles after energy minimization.

3. Results and discussion

A bright-field image of the arrangement of holes, using only elastically scattered electrons, is shown in Fig. 1.

The holes were prepared in such a way that a variety of different configurations are present which are expected to display different spectral behaviour. The upper three holes are sufficiently remote from each other to ensure that no coupling of the electromagnetic fields associated with the individual holes is expected. Coupling effects occur if the hole separation is comparable to the range of the evanescent field of single-hole modes, which is of the order of a few 10 nanometers. The separation of the three holes in the centre of the structure is only about 10 nm for which we expect strong coupling of adjacent holes. A linescan of the Ag slab thickness through these three holes is shown in Fig. 2. The thickness of the original Ag film is about 100 nm. This is large compared to the typical skin depth in Ag so that coupling of the SPs on the top and bottom surfaces (leading to symmetric and antisymmetric SP modes) is negligible. Significant top–bottom coupling is expected at the two ligaments where the thickness of the Ag slab amounts to only about 30 nm.

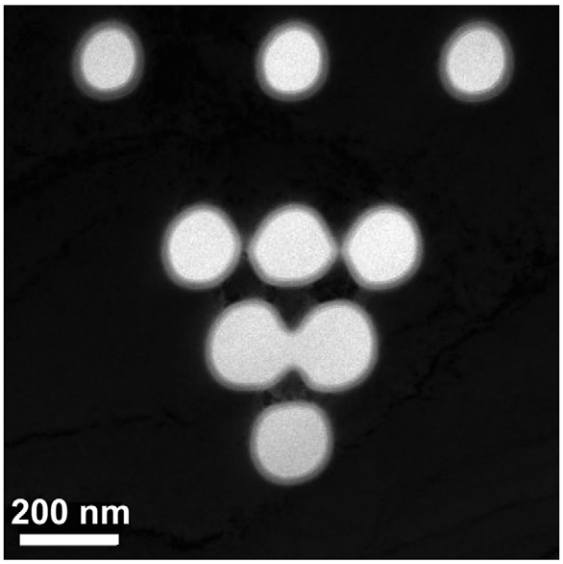

Fig. 1. Bright-field image of the nine holes drilled by a focused ion beam.

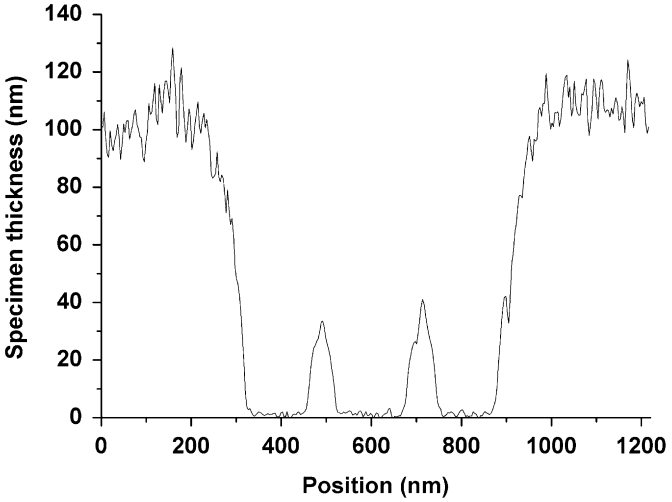

Fig. 2. Thickness of the Ag slab across the central three holes in Fig. 1 as determined by EELS (see text).

The two holes in the second row from the bottom are connected. All 6 holes in the lower part of the pattern are close enough to allow coupling of two and more holes.

Energy-filtered images obtained at energy losses of 0.6 ± 0.1, 1.0 ± 0.1, 1.4 ± 0.1 and 2.4 ± 0.1 eV are shown in the left column of Fig. 3.

As expected, there are very pronounced intensity maxima visible in the image series. Note that the length scale of some features is as small as 10–20 nm, which can presently not be imaged by other techniques. Average EELS spectra were extracted from the EFTEM data stack from "hot-spot" areas (marked by squares in Fig. 3) where the energy-loss signal is particularly strong (Fig. 3). The SP losses are superimposed on the tail of the zero-loss peak which was not subtracted because of insufficient knowledge of its shape. Resonances 4 and 5 exhibit a circular shape and are present in single isolated holes as well as in all other holes. All other resonances are due to coupling effects among neighbouring holes. The low-energy resonances are located at triple points, whereas resonance 3 is located between two holes. Note that the circular resonances 4 and 5 are absent at positions where coupling effects dominate. This can be ascribed to the Begrenzungs effect [1], which states that the probability for the excitation of one plasmon resonance is reduced in the presence of another resonance.

Resonances 4 and 5 are present in well-separated holes indicating that they are fundamental SP resonance features of single holes. In order to verify this we did DDA calculations of holes with 3 different aspect ratios. For all three aspect ratios the optical absorption shows two maxima (Fig. 4), similar to the experimental spectrum in Fig. 3.

In Fig. 5 the positions of these maxima are displayed versus the inverse aspect ratio. The resonance energies decrease with increasing width of the hole because of geometrical reasons, i.e. the wavelength of the plasmon resonance scales with the size of the hole. The experimental data (symbols with error bars) fit very well with the calculations, which is a strong evidence for the calculations to reflect the observed energy losses.

In Fig. 6 the distribution of the polarization of the dipoles is shown for the two peaks of the absorption spectra. The origin of the speckle may have its origin from the finite size of the simulation cell. The low-energy peak shows high electric field intensity on two opposite sides of the hole (red colour) which is typical for a dipolar field distribution, whereas the high-energy peak shows high intensity of the y-component $|E_y|^2$ (green) as well as the x-component $|E_x|^2$ (red) of the electric field in the perpendicular direction, which we interpret as a quadrupolar excitation of the hole. We conclude that these are the two basic resonance modes of singular holes in a silver film.

The symmetry of the modes is not visible in the EFTEM images because the momentum transfer of an electron moving along the z direction shows no azimuthal dependence in the x–y plane. This makes both dipolar and quadrupolar modes appear as circular rings. In Fig. 7 the energy-loss spectra extracted from different positions within an isolated hole are shown. The dipolar and quadrupolar resonances are both visible in the spectra close to the rim of the hole, but not in the hole centre (not shown). The ratio of dipolar to quadrupolar resonance is higher and more remote from the rim. This is in accordance with theory which predicts stronger field localization with increasing mode number [32]. As a side note, we mention that higher-order multipolar modes can in principle be excited by electrons, but their excitation probability is lower.

We now turn from single-hole resonances to resonances involving several holes. The resonances due to coupling of holes are located at lower energies than the single-hole resonances. We find that the larger the area is that contributes to the resonance, the lower is the resonance energy, which we ascribe to the geometry effect. The low-energy resonances 1 and 2 show approximately trigonal symmetry. For a discussion of plasmon resonances in such structures we refer to the paper of Alegret et al. [33]. Here we concentrate more closely on the linear 3-hole resonance 3 which is shown enlarged in Fig. 8. Hot spots are visible on the two ligaments. This is because the near-field interaction scales with the third power of the ligament width, which means that the field strength becomes very strong at such narrow ligaments. The situation is similar as for two almost touching spheres [34]. At large separation the dipole response of each particle is visible whereas for approaching particles the field between the particles becomes strong and the dipolar character of each individual particle gets lost. The importance of the ligament width is supported by the observation that no strong resonances are visible in the two linear 3-hole structures inclined by about 60°. This is most likely due to the wider ligament widths for these inclined 3-hole structures. An interesting feature is found from spectra extracted from single image pixels from the centre of the ligaments (red colour) and more remote (black colour) towards the hole centres (Fig. 8).

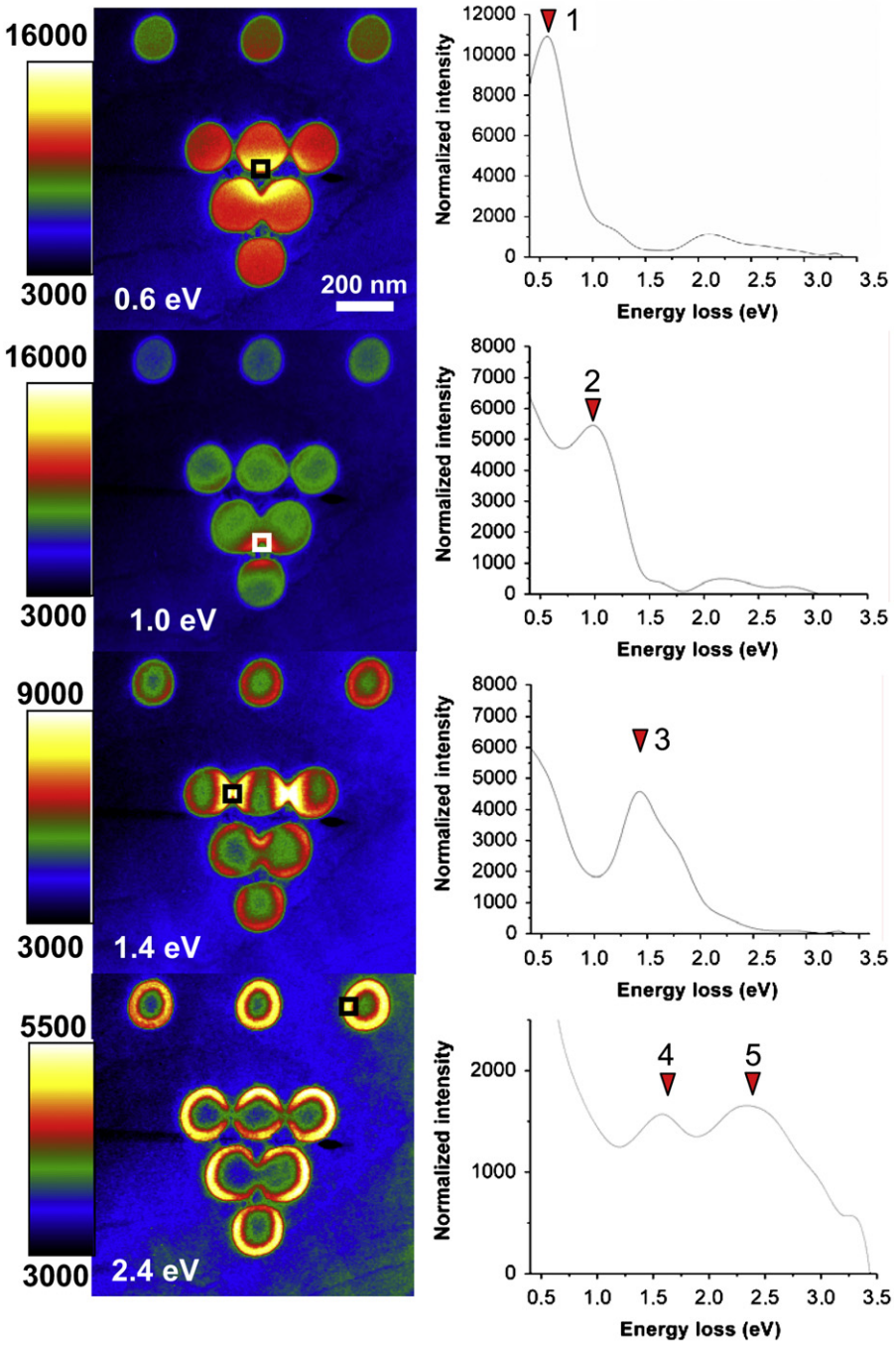

Fig. 3. Energy-filtered images at 4 different energy losses. The respective energy-loss spectra extracted from the marked regions are shown on the right side. Because of the strong variation of the resonance intensities the scaling is different in the 4 images (see scale bar on the left).

The red spectrum shows an additional peak blue-shifted by about 0.4 eV. For the discussion of the possible origin of this peak we apply the hybridization model developed by Prodan et al. [35]. This model describes the electromagnetic behaviour of a coupled system analogous to molecular orbital theory. It gives a qualitative picture of possible eigenmodes of a coupled system the energies of which are assigned by a comparison with experimentally observed resonances. This approach does not aim at a quantitative comparison which can be achieved only by a solution of Maxwells' equations and which is numerically demanding for such a large system. We consider the linear 3-hole system as a coupled system. Because the resonant features are found along the long (horizontal) axis of this system, 6 charges along this axis are taken into account located at positions where the horizontal axis cuts the hole edges (Fig. 9). There can be positive or negative charges at these positions. This leads to 64 possible configurations. It is important to emphasize that there is no need for equal numbers of positive and negative charges because the holes are connected by bulk material which can carry AC currents. This is different in case of coupled spheres in a non-conducting environment [34]. For simplicity, we restrict the number of equal charges in a row to four which reduces the configuration number to 50. Six equal charges are physically impossible and five equal charges are less probable due to

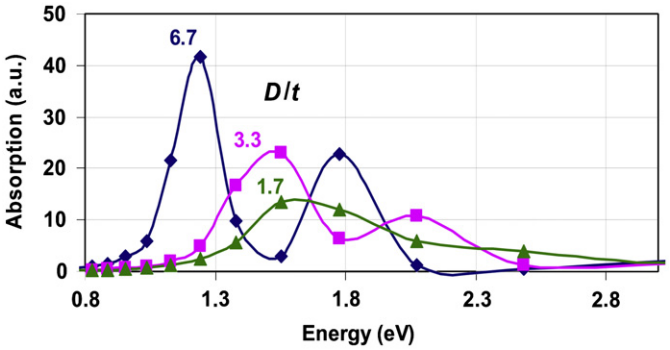

Fig. 4. Light absorption as obtained from DDA calculations of a nanohole for three different ratios of hole diameter D to slab thickness t. The lines are splines to guide the eye.

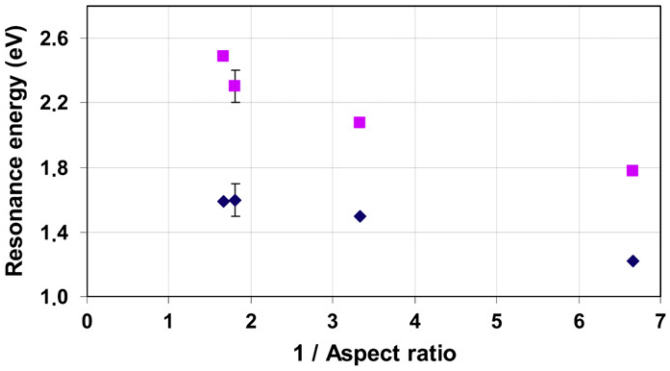

Fig. 5. Resonance peak positions (grey squares and diamonds) obtained by DDA as a function of inverse aspect ratio. The symbols with error bars show the experimental peak positions (see Fig. 3, bottom).

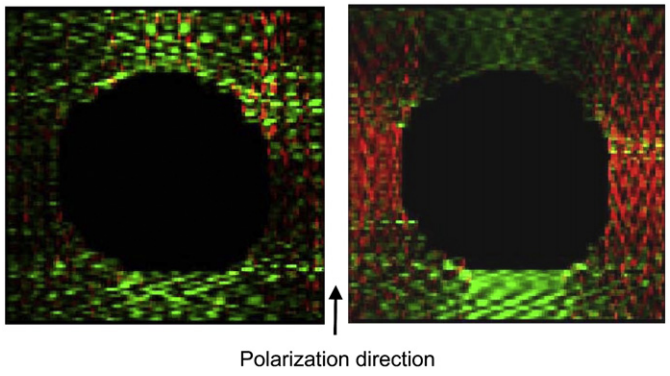

Fig. 6. Distributions of the intensity of the x- (red) and y-component (green) of the electric field for the low-energy (left) and high-energy (right) peaks shown in Fig. 4. The left distribution shows dipolar, the right one quadrupolar symmetry. (For interpretation of the references to colour in this figure legend, the reader is referred to the web version of this article.)

complicated paths of the AC currents. Taking into account symmetry operations the configuration number is further reduced to 28. In order to estimate the electrostatic energy we assume that the electrostatic interaction across the two thin ligaments is stronger than the interaction of charges within the holes. This is justified because the ligament width is much smaller than the hole diameter. Under these assumptions we find that the 28 configurations can be divided into 11 groups with different electrostatic energies. From each group one configuration is plotted in Fig. 9. Low-energy configurations are shown on bottom, high-energy ones on top.

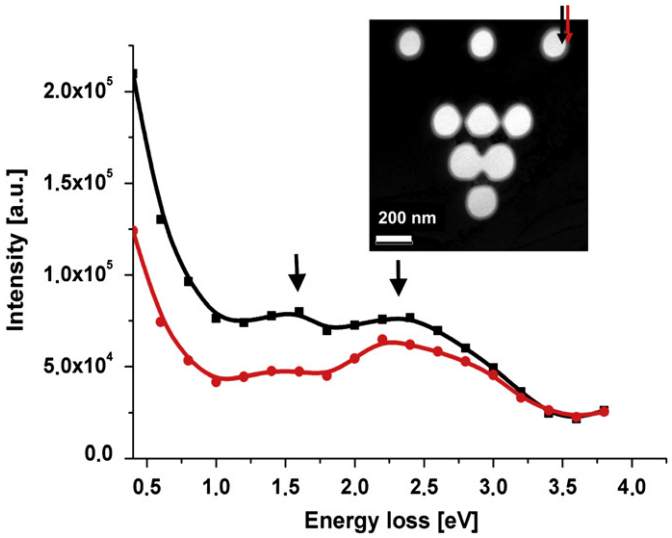

Fig. 7. Energy-loss spectra extracted from positions close to the rim (red) and more remote from the rim (black) of an isolated hole. (For interpretation of the references to colour in this figure legend, the reader is referred to the web version of this article.)

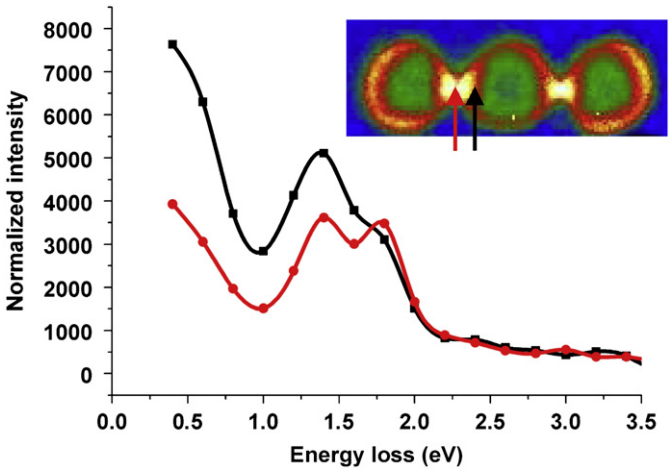

Fig. 8. Spectra from two different positions of resonance 3. The spectra are from single image pixels at positions indicated by arrows.

Red circles in Fig. 9 mark ligament positions with equal charges on both sides. Not surprisingly, the two configurations with highest energy have equal charges on both sides of the ligaments while the low-energy configurations have opposite charges at these positions. Configurations with only one ligament with equal charges have intermediate energies. For the interpretation of the blue-shifted peak found for electrons passing through the ligaments it is important to note that only the modes marked by red circles can be excited in this case because the electron cannot induce opposite charges on the two sides of its trajectory [36]. Therefore we ascribe the blue-shifted peak at 1.8 eV (Fig. 8) to these configurations. The low-energy peak at 1.3 eV is then due to the configurations shown on bottom of Fig. 9. We suspect that the other configurations have intermediate energies and that these merge with the two main peaks. The resulting energy-level diagram is shown in Fig. 10.

In order to shed some light on the coupling mechanism between the charge accumulations on the two ligaments we measured the decay length, ρ, of the intensity into the hole. For

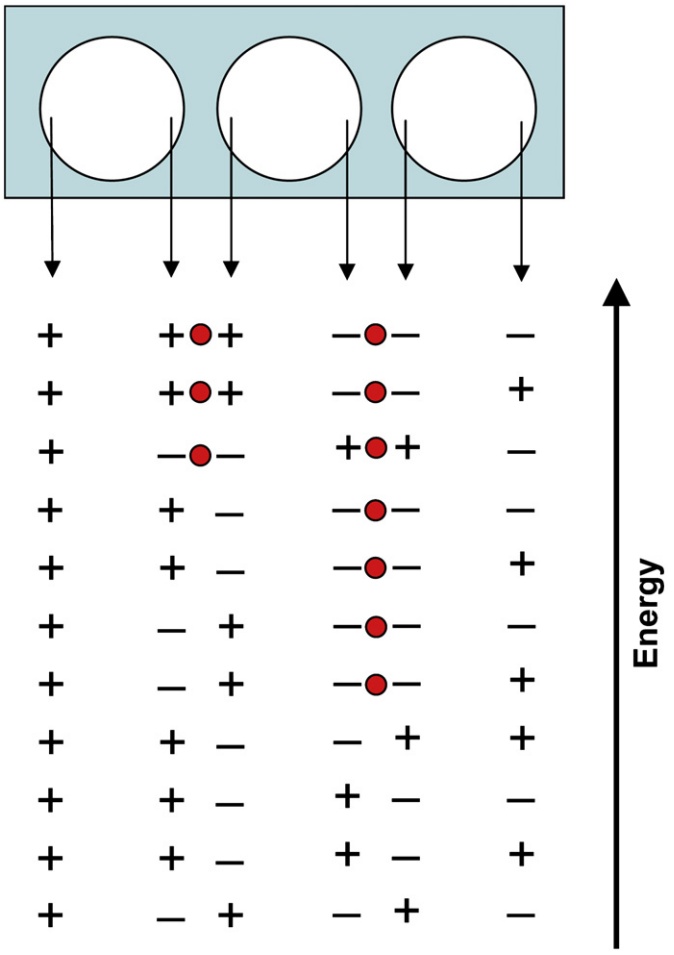

Fig. 9. Possible arrangement of 6 charges in a linear 3-hole system. The charges are concentrated in the area around the arrow origins. The red dots mark positions where equal charges are present on both sides of the ligament. The configurations are arranged according to their electrostatic energy. (For interpretation of the references to colour in this figure legend, the reader is referred to the web version of this article.)

this we extracted intensity linescans along the horizontal axis and fitted exponential functions $I=I_0\exp(-r/\rho)$ to the data (Table 1).

The decay lengths are in the range of 25–45 nm, which is in accordance with results from Rindzevicius et al. [37]. Because this is well below the hole diameter we believe that direct coupling via the electromagnetic dipole fields is less likely than coupling mediated by SPs propagating along the inner walls of the nanoholes.

4. Conclusions

We have shown a variety of resonant surface plasmon features in a perforated Ag slab. Apart from single-hole dipolar and quadrupolar resonances, coupling effects between adjacent holes were
observed. These results demonstrate the power of EFTEM for the study of surface plasmon resonances. The spatial distribution of the resonances is directly obtained by the EFTEM technique, in fact in situ during the measurement which took about 7.5 min in the example shown here. This is of particular importance for the identification of surface plasmon resonances in complex structures where it is by no means obvious at which positions "hot spots" occur. Once these spots are identified it is also possible to obtain high-quality EELS spectra from these locations. It is likely

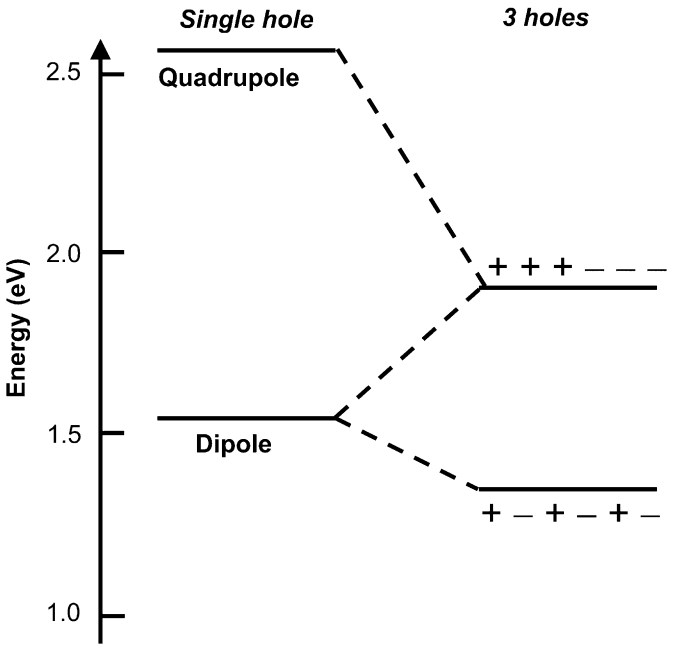

Fig. 10. Energy-level diagram of the two single-hole resonances and the 3-hole resonances.

Table 1
Energy dependence of the decay length of resonances 3 (Fig. 3) along the horizontal axis.

Energy loss (eV)	Decay length (nm)
1.4	44
1.6	38
1.8	25

that this technique will play an important role for the design of optical components used in plasmonic circuits, but also for the optimization of surface structures used for SERS. This could lead to a significant improvement of the efficiency in the identification of single molecules.

Acknowledgments

The preparation of the holes by U. Eigenthaler using focused ion beam is greatly appreciated. We thank Prof. F. J. García de Abajo, Prof. M. I. Stockman, Dr. M. Kociak, and Dr. L. Henrard for helpful discussions. The authors acknowledge financial support from the European Union under the Framework 6 program under a contract for an Integrated Infrastructure Initiative. Reference 026019 ESTEEM.

References

[1] R.H. Ritchie, Phys. Rev. B 106 (1957) 874–881.
[2] H. Raether, in: Excitation of Plasmons and Interband Transitions by Electrons, Springer-Verlag, Berlin, Heidelberg, New York, 1982.
[3] M.I. Stockman, Phys. Rev. Lett. 79 (1997) 4562–4565.
[4] S.M. Nie., S.R. Emory, Science 275 (1997) 1102–1106.
[5] S.A. Maier, H.A. Atwater, J. Appl. Phys. 98 (2005) 011101-1–10.
[6] K. Kneipp, Y. Wang, H. Kneipp, L.T. Perelman, I. Itzkan, R.R. Dasari, M.S. Feld, Phys. Rev. Lett. 78 (1997) 1667–1670.
[7] R. Esteban, R. Vogelgesang, J. Dorfmüller, A. Dmitriev, C. Rockstuhl, C. Etrich, K. Kern, Nano Lett. 8 (2009) 3155–3159.
[8] F.J. García de Abajo, M. Kociak, Phys. Rev. Lett. 100 (2008) 106804-1–4.
[9] P. Batson, Phys. Rev. Lett. 49 (1982) 936–940.
[10] Z.L. Wang, J.M. Cowley, Ultramicroscopy 23 (1987) 97–108.

[11] D. Ugarte, C. Colliex, P. Trebbia, Phys. Rev. B 45 (1992) 4332–4343.
[12] J. Nelayah, M. Kociak, O. Stéphan, F.J. García de Abajo, M. Tencé, L. Henrard, D. Taverna, I. Pastoriza-Santos, L.M. Liz-Marzan, C. Colliex, Nat. Phys. 3 (2007) 348–353.
[13] M. Bosman, V.J. Keast, M. Watanabe, A.I. Maaroof, M.B. Cortie, Nanotechnology 18 (2007) 1–5.
[14] M.-W. Chu, V. Myroshnychenko, C.H. Chen, J.P. Deng, C.Y. Mou, F.J. García de Abajo, Nano Lett. 9 (2009) 399–404.
[15] J. Nelayah, L. Gu, W. Sigle, C.T. Koch, I. Pastoriza-Santos, L.M. Liz-Marzan, P.A. van Aken, in: in: S. Richter, A. Schwedt (Eds.), Proc. 14th European Microscopy Congress, Aachen, vol. 2, Springer, Berlin, 2008, pp. 243–244.
[16] B. Schaffer, K. Riegler, W. Grogger, F. Hofer, Micron 40 (2009) 269–273.
[17] J. Nelayah, L. Gu, W. Sigle, C.T. Koch, I. Pastoriza-Santos, L.M. Liz-Marzan, P.A. van Aken, Opt. Lett. 34 (2009) 1003–1005.
[18] B. Schaffer, U. Hohenester, A. Trügler, F. Hofer, Phys. Rev. B 79 (2009) 041401-1–4.
[19] W. Sigle, J. Nelayah, C.T. Koch, P.A. van Aken, Opt. Lett. 34 (2009) 2150–2152.
[20] T.W. Ebbesen, H.J. Lezec, H.F. Ghaemi, T. Thio, P.A. Wolff, Nature 391 (1998) 667–669.
[21] P.B. Catrysse, S.H. Fan, J. Nanophotonics 2 (2008) 021790-1–20.
[22] F. Moresco, M. Rocca, T. Hildebrandt, M. Henzler, Phys. Rev. Lett. 83 (1999) 2238–2241.
[23] F. Ouyang, M. Isaacson, Ultramicroscopy 31 (1989) 345–350.
[24] C.T. Koch, W. Sigle, R. Höschen, M. Rühle, E. Essers, G. Benner, M. Matijevic, Microsc. Microanal. 12 (2006) 506–514.
[25] S. Uhlemann, H. Rose, Optik 96 (1994) 163–178.
[26] E. Essers, G. Benner, T. Mandler, S. Meyer, D. Mittmann, M. Schnell, R. Höschen, Ultramicroscopy (2010), this issue, doi: 10.1016/j.ultramic.2010.02.009.
[27] B. Schaffer, W. Grogger, G. Kothleitner, Ultramicroscopy 102 (2004) 27–36.
[28] R. Egerton, in: Electron Energy-Loss Spectroscopy in the Electron Microscope, second ed., Plenum Press, New York, 1996.
[29] B.T. Draine, P.J. Flatau, User guide for the discrete dipole approximation code DDSCAT.6.0, 〈http://arxiv.org/abs/astro-ph/0309069〉, 2003.
[30] N. Geuquet, L. Henrard, Ultramicroscopy, (2010), this issue, doi:10.1016/j.ultramic.2010.01.013.
[31] J. Nelayah, Ph.D. Thesis, Université Paris-Sud XI UFR Scientifique d'Orsay, 2007.
[32] K.L. Kelly, E. Coronado, L.L. Zhao, G.C. Schatz, J. Phys. Chem. B 107 (2003) 668–677.
[33] J. Alegret, T. Rindzevicius, T. Pakizeh, Y. Alaverdyan, L. Gunnarsson, M. Käll, J. Phys. Chem. C 112 (2008) 14313–14317.
[34] I. Romero, J. Aizpurua, G.W. Bryant, F.J. García de Abajo, Opt. Express 14 (2006) 9988–9999.
[35] E. Prodan, C. Radloff, N.J. Halas, P. Nordlander, Science 302 (2003) 419–422.
[36] M.-W. Chu, V. Myroshnychenko, C.H. Chen, J.-P. Deng, C.-Y. Mou, F.J. Garcia de Abajo, Nanoletters 9 (2009) 399–404.
[37] T. Rindzevicius, Y. Alaverdyan, B. Sepulveda, T. Pakizeh, M. Käll, R. Hillenbrand, J. Aizpurua, F.J. García de Abajo, J. Phys. Chem. C 111 (2007) 1207–1212.

CHAPTER 8

Resonant wedge-plasmon modes in single crystalline gold nanoplatelets

Lin Gu[1], Wilfried Sigle[1], Christoph T. Koch[1], Burcu Ögüt[1], Peter A. van Aken[1], Nahid Talebi[1,2], Ralf Vogelgesang[3], Jianlin Mu[4], Xiaogang Wen[4], and Jian Mao[4]

1. Max Planck Institute for Metals Research, Heisenbergstraße 3, 70569, Stuttgart, Germany
2. Photonics Research Laboratory, Center of Excellence for Applied Electromagnetic Systems, School of Electrical and Computer Engineering, University of Tehran, North Kargar Ave., Tehran, Iran
3. Max Planck Institute for Solid State Research, Heisenbergstraße 1, 70569, Stuttgart, Germany
4. School of Material Science and Engineering, Sichuan University, 610065 Chengdu, People's Republic of China

Surface plasmon resonances of gold nanoplatelets with hexagonal, triangular and truncated triangular shapes have been measured using the EFTEM imaging technique by Lin Gu. The experimental results have been confirmed through FDTD simulations performed by Nahid Talebi. Jianlin Mu, Xiaogang Wen and Jian Mao have provided the specimens. All co-authors have contributed to the data interpretation.

Resonant wedge-plasmon modes in single-crystalline gold nanoplatelets

Lin Gu,[1,*] Wilfried Sigle,[1,†] Christoph T. Koch,[1] Burcu Ögüt,[1] Peter A. van Aken,[1] Nahid Talebi,[1,2] Ralf Vogelgesang,[3] Jianlin Mu,[4] Xiaogang Wen,[4] and Jian Mao[4]

[1]*Max Planck Institute for Metals Research, Heisenbergstraße 3, D-70569 Stuttgart, Germany*

[2]*Photonics Research Laboratory, Center of Excellence for Applied Electromagnetic Systems, School of Electrical and Computer Engineering, University of Tehran, North Kargar Ave., Tehran, Iran*

[3]*Max Planck Institute for Solid State Research, Heisenbergstraße 1, D-70569 Stuttgart, Germany*

[4]*School of Material Science and Engineering, Sichuan University, 610065 Chengdu, People's Republic of China*

(Received 22 December 2010; revised manuscript received 1 March 2011; published 24 May 2011)

Using energy-filtered transmission electron microscopy we measured surface-plasmon resonances of gold nanoplatelets with different shapes and edge lengths at high spatial resolution. We find equidistant maxima of the energy-loss probability along the platelet edges. The plasmon dispersion of the different geometries is very similar, i.e., hardly dependent on specimen shape. The experimental results are verified by means of finite-difference time-domain calculations which reveal the presence of wedge-plasmon polaritons propagating along the platelet edges. At platelet corners, apart from radiative losses, wedge-plasmon polaritons are partially reflected or transmitted to neighboring edges. The interference of all these contributions leads to the observed plasmon resonance modes. This is an essential step towards a thorough understanding of plasmon eigenmodes in prismatic nanoplatelets.

DOI: 10.1103/PhysRevB.83.195433 PACS number(s): 73.20.Mf, 68.37.Lp, 79.20.Uv

I. INTRODUCTION

Coherent oscillations of electrons at metal surfaces excited by external electromagnetic radiation are called surface plasmons. A condition for the occurrence of surface plasmons is that at the frequency ω of the exciting radiation the dielectric function of the material satisfies the condition $\mathrm{Im}[\varepsilon(\omega)] \ll \mathrm{Re}[-\varepsilon(\omega)]$.[1] In the case of confined surfaces, as is the case for small metal particles, surface-plasmon resonances (SPRs) may occur, the shape and resonance frequency of which are also defined by the particle geometry. Noble metal nanoparticles with sizes smaller than the wavelength of the excited radiation can support localized surface-plasmon resonances and exhibit optical properties enabling a variety of applications, including surface-enhanced Raman spectroscopy (SERS),[2,3] chemical and biological sensing,[4,5] lithographic fabrication,[6,7] plasmonic waveguides,[8] and second-harmonic generation.[9] Recent investigations in the field of plasmonics have focused on metal nanostructures substantially smaller than the wavelength of light. Consequently, the optical response reflects the properties of the local electric field at the particle and has a predominantly dipole character which can be optimized by manipulating the system geometry.[10–12] By increasing the particle size, the optical excitation of higher-order harmonics, i.e., multipolar plasmon resonances, becomes possible and significantly modifies the optical properties.[13,14] Multipolar surface-plasmon modes were demonstrated spectrally in the visible and near-infrared regions;[15,16] meanwhile, correlated theoretical approaches were developed.[17,18] In the long-wavelength regime where the surface-plasmon dispersion is close to the light line, the combined excitation consisting of a surface plasmon and an electromagnetic wave is called a surface-plasmon polariton (SPP).[19–21] SPPs have attracted considerable attention due to their potential applications in optical circuits and optical computers.

Surface-plasmon resonance phenomena have been widely studied using optical approaches such as scanning near-field optical microscopy and dark-field spectroscopy.[12,22] Measuring small energy losses of fast electrons in a transmission electron microscope (TEM) provides an alternative access to investigate local SPRs with high spatial resolution by using a focused electron beam.[23–25] The combination of scanning transmission electron microscopy (STEM) with electron-energy-loss spectroscopy (EELS) allows plasmon mapping at a spatial resolution better than $\lambda/40$. With the advent of high-performance electron monochromators and in-column energy filters, energy-filtering transmission electron microscopy (EFTEM) utilizing a broad electron beam and parallel acquisition in the low energy-loss range, has emerged as a technique that offers rapid data collection and outstanding spatial sampling.[26–28]

Here we demonstrate mapping of plasmon resonances at the surfaces of ~70-nm-thick single-crystalline gold nanoplatelets fabricated by a solution-phase microwave-mediated method using the EFTEM approach. The spatial distribution of the resonances up to fourth order was revealed on triangular, truncated-triangular, and hexagonal nanoplatelets. We found that the dispersion relationships for the different geometries are very similar and depend mainly on the length of the platelet sides. Finite-difference time-domain (FDTD) calculations show that this is due to the occurrence of wedge plasmons along the nanoparticle rim.

II. EXPERIMENT

Triangular noble metal nanoplatelets and snipped triangular nanoplatelets were prepared by either solution-phase light-mediated syntheses or thermal growth techniques.[29–33] Here we use the fabrication of Au nanoplatelets and truncated nanoplatelets by a microwave-mediated method. 0.5 ml of 0.1 M $HAuCl_4$ (chloroauric acid) aqueous solution was prepared in a teflon bottle followed by adding 0.144 g of glucose and 0.03 g of polyvinylpyrrolidone (PVP, molecular weight

≈ 30 000) to the solution. The mixture was dissolved in 15 ml of EG (ethylene glycol) solution and stirred for 5 min to form a solution yellowish in color. The solution was subsequently exposed to microwave irradiation in a household microwave oven (Galanz: G80D23CSL-Q6). The total reaction time was 10 min at an average power of 250 W. After the process, the color of the solution had noticeably changed to reddish-brown. The final product solution was then centrifuged at 13 000 rpm for 10 min before washing three times in distilled water and ethanol, consecutively.

Specimens of single-crystalline Au nanoplatelets for TEM investigation were drop coated on 30-nm-thick silicon nitride membranes. EFTEM and EELS experiments were performed using the Zeiss Sub-eV-Sub-Ångstrom-Microscope (SESAM) (Carl Zeiss, Oberkochen, Germany) equipped with an electrostatic Ω-type monochromator and an in-column MANDOLINE filter offering very high dispersion of the energy-loss spectrum. The SESAM microscope delivers outstanding stability and electron optical performance which allows valence EELS and valence EFTEM experiments with both high energy and high spatial resolution to be performed.[34–36] The energy resolution of the microscope defined by the full width at half maximum of the elastic zero-loss peak is below 90 meV for routine applications and has already been demonstrated to be smaller than 50 meV.[37] The in-column MANDOLINE filter provides high dispersion, high transmissivity, and high isochromaticity allowing the selection of very small energy-loss windows (<0.2 eV) for diffraction and imaging applications.[38] Besides a significant enhancement of the energy resolution, the main benefit of using monochromated electrons involves a sharp drop of the intensity from the zero-loss peak tail, enabling the detection of spectral features in the UV-visible–near-infrared domain without any numerical processing. A series of energy-filtered images from 0.4 to 3.0 eV energy loss (corresponding to wavelengths from 400 to 3000 nm) were acquired with a collection of semiangles of 6 mrad and an energy-selecting window of 0.2 eV; thus two-dimensional spatial distributions of SPRs in the energy range of interest can be mapped close to nm resolution. Specimen thickness was determined by EELS from the ratio of zero-loss intensity and total spectral intensity.[39]

III. THREE-DIMENSIONAL-FDTD SIMULATION

Three-dimensional finite-difference time-domain (3D-FDTD) calculations were used to verify the obtained experimental data. The codes were developed at the Photonics Research Laboratory, Tehran.[40,41] For these calculations the simulation domain was discretized with cubic cells having an edge length of 5 nm. The second-order absorbing boundary condition was exploited to terminate the simulation domain. Moreover, additive sources in the form of either harmonic plane waves or focused wideband Ricker wavelets[42] were used to obtain the modal field profiles or resonance spectra, respectively. The maximum number of time steps in our simulation was 2×10^4. In order to compute the resonance spectra, the integral intensity of the electric field over the samples was computed. For the Au permittivity we used a Drude model extended by two critical-point functions[43] in order to account for intra- and interband transitions. This model is in close agreement with experimental data.

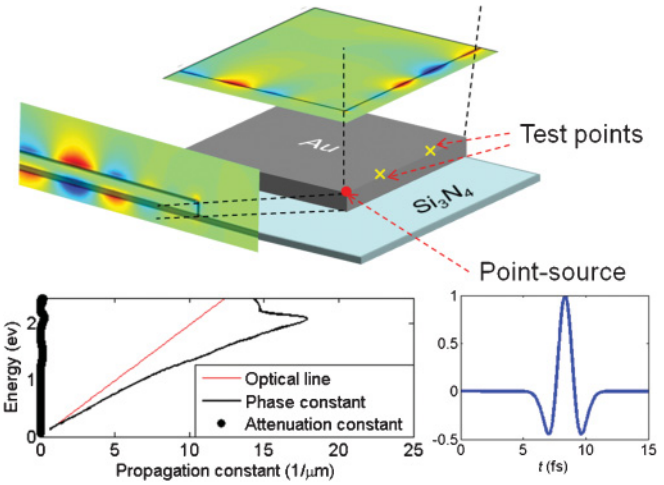

FIG. 1. (Color online) Scheme for computing the propagation constant of wedge-plasmon modes using 3D-FDTD. A wideband localized point source in the form of a Ricker wavelet (bottom right) was implemented at the red dot. The temporal evolution of the field components was detected at positions marked by yellow crosses.

In order to compute the propagation constant of the wedge-plasmon mode, we have considered a semi-infinite gold edge with an opening angle of 90°, as shown in Fig. 1. An additive source point was introduced in the form of a Ricker-wavelet temporal function at the position depicted in Fig. 1. This source gives rise to two plasmonic waves propagating along the wedges. The electromagnetic field components are computed at two introduced test points with the locations depicted in

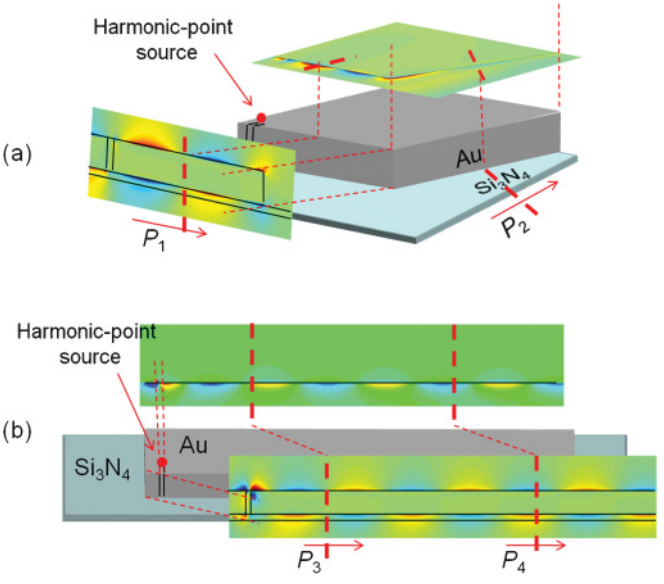

FIG. 2. (Color online) (a) Scheme for computing the transmission and reflection coefficients of the wedge-plasmon mode around a bend using 3D-FDTD. A harmonic wideband point source was introduced at the position of the red dot. Power propagation was monitored at planes indicated by red lines. This was used to calculate reflected and transmitted power. (b) Scheme for calibration of the data obtained in (a).

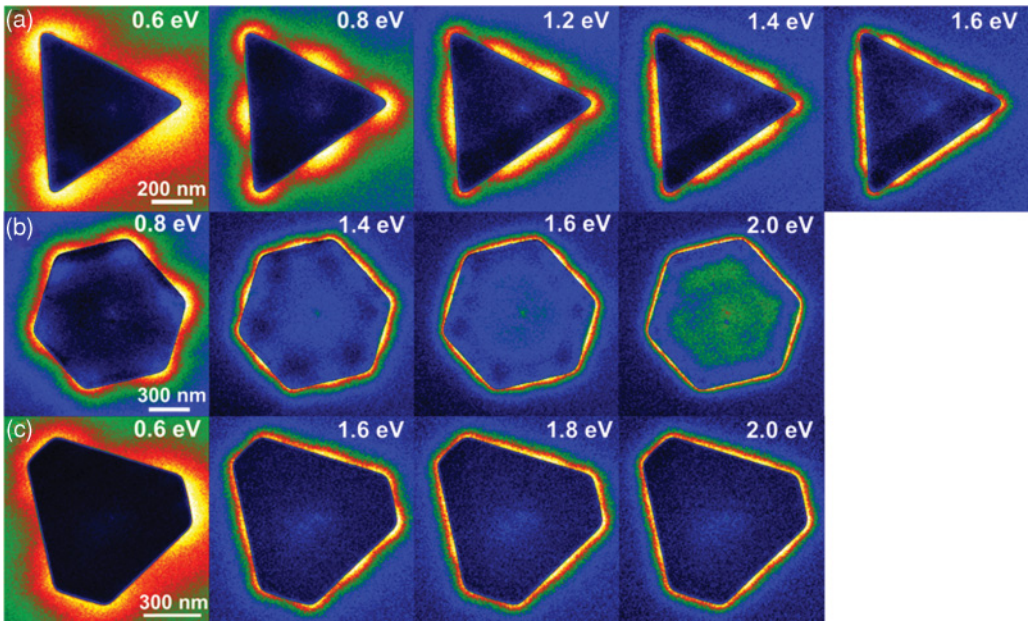

FIG. 3. (Color online) Energy-filtered images of the (a) triangular, (b) hexagonal, and (c) truncated triangular Au nanoplatelets. Colors indicate energy-loss probabilities using a temperature color scale. Low probability is indicated as blue (dark) and maximum probability as yellow (bright). The energy loss is displayed for each figure.

Fig. 1, over the whole simulation time. Then the discrete Fourier transforms of the field components are computed. Each electromagnetic field component computed at the two test points should satisfy the following equation:

$$\varphi(\vec{p}_2) = \exp(\gamma\,|\vec{p}_2 - \vec{p}_1|)\,\varphi(\vec{p}_1), \tag{1}$$

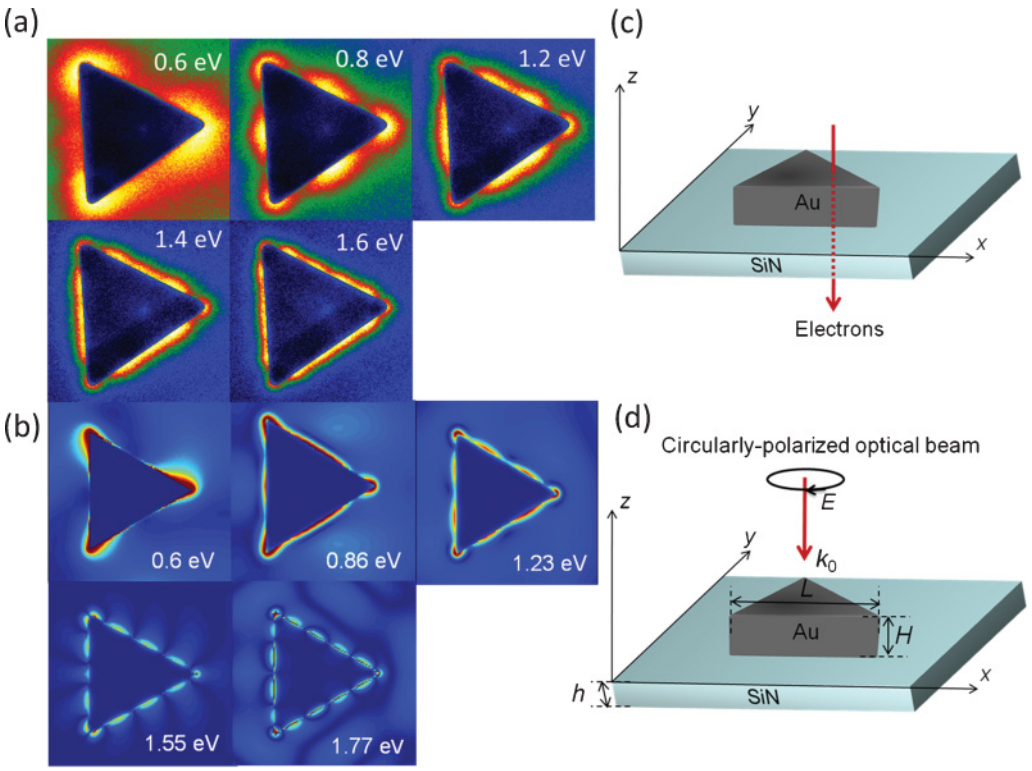

FIG. 4. (Color online) Comparison between (a) experimental and (b) simulated mode profiles of the plasmonic resonances of the triangular gold nanoplatelet on a thin Si_3N_4 substrate with the dimensions $H = 70$ nm, $h = 20$ nm, and $L = 950$ nm, as a function of the energy marked on each frame. The color scale for the experimental and simulated data was normalized to the maximum intensity. The right insets show the different schemes used to excite the plasmonic modes in EELS and FDTD simulations. Circularly polarized light is used to replicate the EELS data (see text).

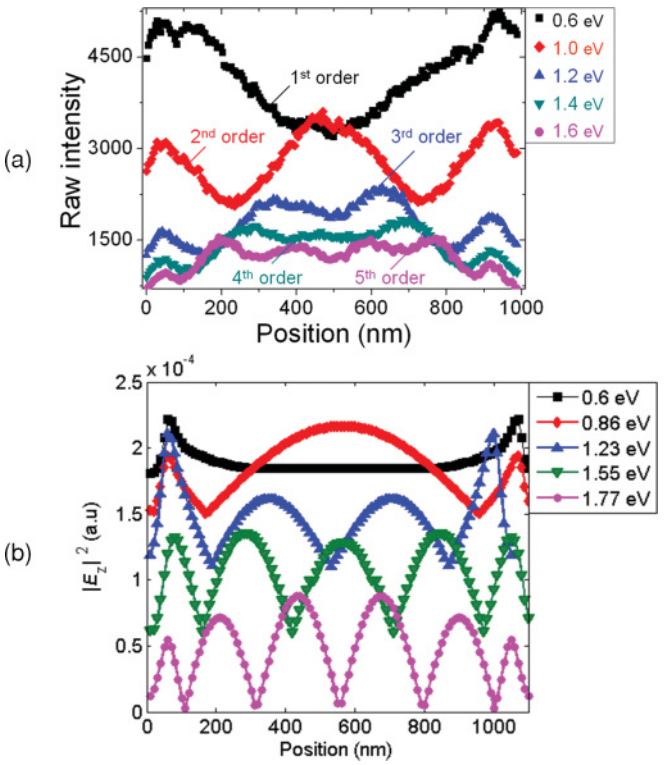

FIG. 5. (Color online) Comparison between measured and computed mode profiles along one edge of the triangular gold nanoplatelets. The data show good qualitative agreement. For quantitative agreement, rigorous calculation of the electron energy-loss process would be necessary.

where $\varphi(\vec{p}_i)$ is an arbitrary electric- or magnetic-field component at the observation point defined by $\vec{p}_i$, and γ is the complex propagation constant of the wedge-plasmon mode. Using Eq. (1), one can define a search function for computing γ:

$$F(\gamma) = \left| \frac{\varphi(\vec{p}_2)}{\varphi(\vec{p}_1)} - \exp(\gamma\,|\vec{p}_2 - \vec{p}_1|) \right|. \qquad (2)$$

The phase and attenuation constants of the wedge-plasmon mode are found by searching for the zeros of $F(\gamma)$ in the complex γ plane.

A similar approach has been used for computing the transmission (T) and reflection (R) coefficients of Table I. As shown in Fig. 2, two wedges meeting at an arbitrary angle have been considered. To excite the wedge-plasmon mode, an indentation was introduced, and a harmonic point source was located just upon the indentation. In order to calculate transmitted (P_2) and reflected (P_1) powers two planes were defined cutting the edges at positions marked by dashed lines in Fig. 2(a). These planes are normal to the wave vector of the wedge-plasmon mode. In order to distinguish between the reflected and incident power, a calibration technique is used as shown in Fig. 2(b). For this, a semi-infinite plane is considered with the same indentation and harmonic source as in Fig. 2(a). Then the power passing through the positions P_3 and P_4 [Fig. 2(b)] is computed. Using the computed powers, the T and R coefficients are computed as $T = P_2/P_4$ and $R = 1 - P_1/P_3$ at each energy.

IV. RESULTS AND DISCUSSION

The thickness of the three nanoplatelets was determined as (70 ± 15) nm, which was constant throughout the structures. This implies that coupling between the two horizontal surfaces through the bulk is negligibly small since the typical skin depth for Au is about 20–25 nm in the energy range studied here. The particles are single crystalline, which is of importance for achieving large surface-plasmon propagation lengths.[44] Energy-filtered images of the nanoplatelets are shown in Figs. 3(a)–3(c). The intensities are color coded for better visibility, and are proportional to the z-projected local photonic density of states.[45] The experimental geometry is shown in Fig. 4(c). For all particles multiple-order plasmon resonances are clearly discernible. For the case of the triangular platelet shown in Fig. 3(a), the intensity along the upper right edge is plotted in Fig. 5(a) at energy losses (wavelengths) of 0.6 (2.07 μm), 1.0 (1.24 μm), 1.2 (1.04 μm), 1.4 (0.89 μm), and

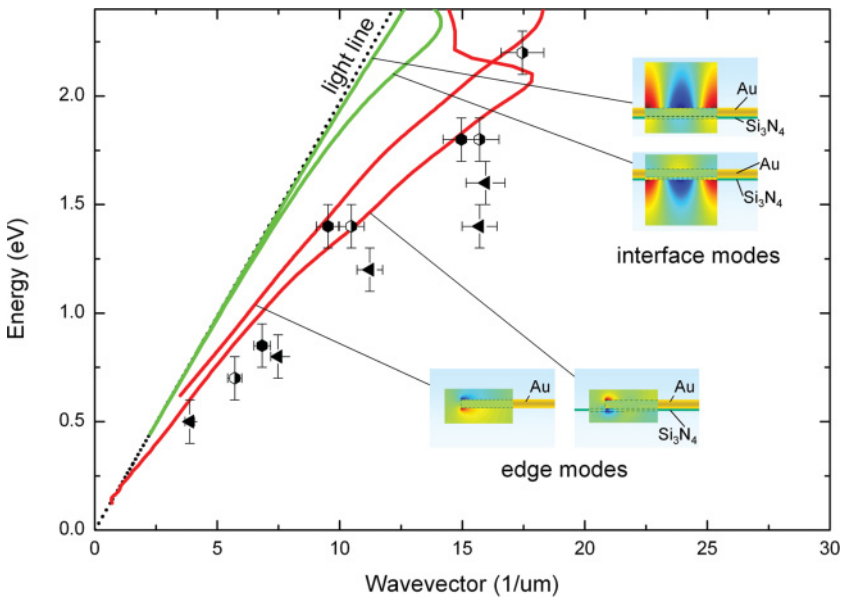

FIG. 6. (Color online) Comparison between the computed propagation constant of various plasmonic modes possible for a semi-infinite Au platelet on a Si_3N_4 substrate, and the measured wave vector of the plasmonic modes obtained from the EFTEM data (triangular symbols for the triangle and hexagonal symbols for the truncated triangle and the hexagon). The insets show the spatial distribution for the z component of the electric field.

TABLE I. Power transmission (T) and reflection (R) coefficients at platelet corners making a 60° and 120° angle, respectively. The numbers were obtained by FDTD at different energies (see Fig. 2 and text).

Energy	0.6 eV		1 eV		1.2 eV		1.4 eV		1.6 eV	
Angle	T	R	T	R	T	R	T	R	T	R
60°	0.091	0.086	0.137	0.077	0.336	0.038	0.418	0.026	0.296	0.079
120°	0.461	0.003	0.483	0.002	0.498	0.001	0.538	0.003	0.234	0.003

1.6 eV (0.78 μm). Equidistant local field enhancements are visible up to the fifth order. Similar intensity variations were found for the other nanoplatelets.

In order to identify the origin of the observed plasmon modes we compare experimental and calculated dispersion curves. We interpret the separation of the equidistant field maxima as half a wavelength of the propagating plasmon. The measured plasmon dispersions are shown in Fig. 6. Because of the very similar dispersion, hexagonal symbols were used for both the truncated triangle and the hexagon. Triangular symbols are used for the triangle. Calculated dispersion curves are shown for the Au nanoplatelet with and without the thin Si_3N_4 membrane. We can distinguish two categories of dispersion curves. For the case of an infinitely extended Au film on a thin Si_3N_4 substrate there is a plasmon located at the interface (lower green line) and another one with field maxima on the Au surface (upper green line). Both are far from the experimental data. Secondly, dispersions of plasmon modes running along the wedges of the nanoparticles (red lines) are shown, both for a freestanding Au film and a Au film on a thin Si_3N_4 substrate. These latter two dispersion curves are close to each other, which means that the thin Si_3N_4 substrate has only little influence on these modes. Most importantly, they are much closer to the experimental data than the pure interface and surface plasmons. The remaining discrepancies can possibly be explained by subtle differences between the real wedge shape and the one used in the simulation. These results are strong evidence that it is these wedge-plasmon modes that we observe in our experiments. From the inset in Fig. 6 one can clearly see that the field maxima of the wedge plasmons are located at the upper and lower wedges.[46,47] This is not unexpected since it is well known that structural discontinuities are always connected with local field enhancement.

In order to calculate the field distributions of the plasmon eigenmodes along the wedges, a circularly polarized excitation was used in the FDTD calculations and response fields at different z positions were incoherently summed up. Since the electric-field distribution around the fast electron is azimuthally isotropic the excitation by a circularly polarized electromagnetic wave resembles the EFTEM experiment much better than the excitation by a linearly polarized wave. The situation of the EFTEM experiment can then be modeled by incoherently integrating the response of the system for one full rotation of the wave's polarization. Both EFTEM and FDTD probe the same set of eigenmodes, i.e., we expect qualitatively the same results, though not quantitatively. This is confirmed by the spatial field distributions [Fig. 4(b)] and the mode profiles along the edge of the triangle [Fig. 5(b)], which both show a remarkable resemblance to the experimental data [Figs. 4(a) and 5(a)].

An important advantage of FDTD is that the dynamics of plasmon propagation can be analyzed. This gives us further important insight into the nature of the resonant plasmonic wedge modes. For this purpose, calculations with wideband local excitations in the form of Ricker-wavelet point sources were performed for the case of the triangular platelet. The locations of the point sources have been chosen in such a way as to distinguish between symmetric and antisymmetric modes, as depicted in the inset of Fig. 7(a). In Figs. 7(b) and 7(c)

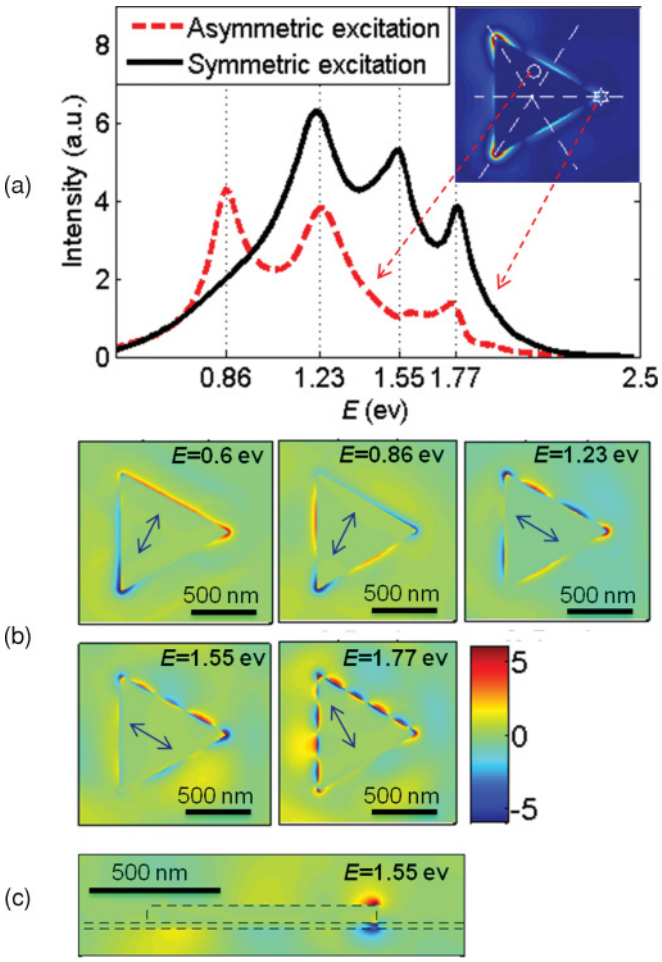

FIG. 7. (Color online) (a) Eigenmodes of the gold triangular nanoplatelets with the geometrical parameters depicted in Fig. 2, computed using FDTD with introduced wideband, localized, symmetric, and asymmetric excitations. Mode profiles at an arbitrary time, computed using FDTD for (b) top view and (c) side view.

the field distribution is shown for each resonance energy at an arbitrary time, for both top and side cross sections. In order to gain further insight into the propagation of the wedge-plasmon modes we performed FDTD calculations with local excitations at various wavelengths for the case of the triangular platelet. In Fig. 7 the field distribution is shown at each wavelength (energy). It is obvious that the wedge plasmons propagate ("transmit") around the corner of the triangle. In the case of complete transmission this effect would lead to whispering gallery modes, if the condition $\sum_{i,j}\left(\gamma L_i + \varphi_{\mathrm{tr},j}\right) = n2\pi$ is met, where γ is the propagation constant, L_i are the edge lengths of the platelet, and $\phi_{\mathrm{tr},}j$ is the phase change when the polariton propagates across the edge. In the case of complete reflection, Fabry-Pérot modes[21] are excited if $2\gamma L + \gamma_{\mathrm{left}} + \gamma_{\mathrm{right}} = n2\pi$, where L is the edge length and φ_{right} and φ_{left} are the phase changes upon reflection at the two boundaries of the edge. However, our calculations show that transmission and reflection coefficients are less than unity (Table I), i.e., we neither have the situation of a whispering gallery mode nor of a Fabry-Pérot resonator. Furthermore, we found that the sum of reflected and transmitted intensities is not equal to the excited intensity, which means that there are radiative losses at the corners. Such radiative losses at pointlike discontinuities are well known. The fractions of transmitted and reflected intensities depend on plasmon energy, as is shown in Table I. The main conclusion of these FDTD calculations is that the observed resonant behavior of the nanoplatelets originates from the interference of excited, reflected, and transmitted wedge SPPs. The relative importance of the individual contributions will depend on the size, thickness (because of coupling effects), and shape of the nanoplatelet as well as on the resonance energy.

Our interpretation of the plasmonic response of nanoplatelets became possible by the study of large nanoplatelets exhibiting multiple field maxima along their edges. In earlier studies SPRs were shown in triangular nanoplatelets[24,48] which had a circumference smaller than the resonance wavelength. Only a single field maximum along the edge was found in these studies. These SPRs are quasistatic eigenmodes of the triangles. In the present study, and also in Ref. 26, larger nanoplatelets were studied which allow us to detect modes with more than one maximum. Our simulations verify that this phenomenon is due to the *propagating* nature of SPPs along the nanoplatelet wedges. This reveals a transition from an SPR- to SPP-dominated regime when the particle circumference becomes comparable to the resonance wavelength.

Finally, we should mention that surface plasmons are also excited on the top and bottom surfaces of the nanoplatelets. However, these are much weaker than the wedge plasmons. The analysis of these modes will be addressed in an upcoming paper.

V. CONCLUSIONS

In conclusion, we showed that surface-plasmon resonances of single-crystalline gold nanoplatelets exhibit very similar behavior, only weakly depending on particle shape. Using FDTD we analyzed all plasmonic modes occurring in nanoplatelets. We found that the plasmonic behavior is dominated by wedge-plasmon modes propagating along the nanoplatelet edges, giving a very close correspondence between theory and experiment. Our results show the intriguing interplay of excited, whispering-gallery-like, and reflected SPPs in nanoplatelets.

ACKNOWLEDGMENTS

We acknowledge financial support from the European Union under the Framework 6 program under a contract for an Integrated Infrastructure Initiative, Reference 026019 (ESTEEM). X.W. thanks the National Natural Science Foundation of China (Grant No. 50872084) for supporting this research. N.T. thanks the Iran Telecommunication Research Center for financial support.

*Present address: Beijing Laboratory for Electron Microscopy, Institute of Physics, Chinese Academy of Sciences, China.
†Corresponding author: sigle@mf.mpg.de

[1] F. J. García de Abajo, Rev. Mod. Phys. **79**, 1267 (2007).
[2] M. Moskovits, Rev. Mod. Phys. **57**, 783 (1985).
[3] S. Kühn, U. Håkanson, L. Rogobete, and V. Sandoghdar, Phys. Rev. Lett. **97**, 017402 (2006).
[4] A. J. Haes, L. Chang, W. L. Klein, and R. P. Van Duyne, J. Am. Chem. Soc. **127**, 2264 (2005).
[5] G. Raschke, S. Kowarik, T. Franzl, C. Sönnichsen, T. A. Klar, and J. Feldmann, Nano Lett. **3**, 935 (2003).
[6] W. Srituravanich, N. Fang, C. Sun, Q. Luo, and X. Zhang, Nano Lett. **4**, 1085 (2004).
[7] A. Sundaramurthy, J. P. Schuck, N. R. Conley, D. P. Fromm, G. S. Kino, and W. E. Moerner, Nano Lett. **6**, 355 (2006).
[8] S. A. Maier, P. G. Kik, and H. A. Atwater, Appl. Phys. Lett. **81**, 1714 (2002).
[9] C. K. Chen, A. R. B. de Castro, and Y. R. Shen, Phys. Rev. Lett. **46**, 145 (1981).
[10] M. Rang, A. C. Jones, F. Zhou, Z.-Y. Li, B. J. Wiley, Y. Xia, and M. B. Raschke, Nano Lett. **8**, 3357 (2008).
[11] L. J. Sherry, R. Jin, R. C. A. Mirkin, G. C. Schatz, and Van R. P. Duyne, Nano Lett. **6**, 2060 (2006).
[12] J. J. Mock, M. Barbic, D. R. Smith, D. A. Schultz, and S. Schultz, J. Chem. Phys. **116**, 6755 (2002).
[13] N. Félidj, J. Grand, G. Laurent, J. Aubard, G. Lévi, A. Hohenau, N. Galler, F. R. Aussenegg, and J. R. Krenn, J. Chem. Phys. **128**, 094702 (2008).
[14] J. R. Krenn, G. Schider, W. Rechberger, B. Lamprecht, A. Leitner, and F. R. Aussenegg, Appl. Phys. Lett. **77**, 3379 (2000).
[15] A. S. Kumbhar, M. K. Kinnan, and G. Chumanov, J. Am. Chem. Soc. **127**, 12444 (2005).
[16] J. E. Millstone, S. Park, K. L. Shuford, L. Qin, G. C. Schatz, and C. A. Mirkin, J. Am. Chem. Soc. **127**, 5312 (2005).
[17] K. L. Shuford, M. A. Ratner, and G. C. Schatz, J. Chem. Phys. **123**, 114713 (2005).
[18] E. Hao and G. C. Schatz, J. Chem. Phys. **120**, 357 (2004).
[19] A. V. Zayats and I. I. Smolyaninov, J. Opt. A: Pure Appl. Opt. **5**, S16 (2003).
[20] N. Yamamoto and T. Suzuki, Appl. Phys. Lett. **93**, 093114 (2008).
[21] J. Dorfmüller, R. Vogelgesang, T. Weitz, C. Rockstuhl, C. Etrich, T. Pertsch, F. Lederer, and K. Kern, Nano Lett. **9**, 2372 (2009).

[22] J. R. Krenn, A. Dereux, J. C. Weeber, E. Bourillot, Y. Lacroute, J. P. Goudonnet, G. Schider, W. Gotschy, A. Leitner, F. R. Aussenegg, and C. Girard, Phys. Rev. Lett. **82**, 2590 (1999).
[23] M. Chu, V. Myroshnychenko, C. Chen, J. Deng, C. Mou, and F. J. García de Abajo, Nano Lett. **9**, 399 (2009).
[24] J. Nelayah, M. Kociak, O. Stéphan, F. J. García de Abajo, M. Tencé, L. Henrard, D. Taverna, I. Pastoriza-Santos, L. M. Liz-Marzán, and C. Colliex, Nat. Phys. **3**, 348 (2007).
[25] M. Bosman, V. J. Keast, M. Watanabe, A. I. Maaroof, and M. B. Cortie, Nanotechnology **18**, 165505 (2007).
[26] J. Nelayah, L. Gu, W. Sigle, C. T. Koch, I. Pastoriza-Santos, Liz-Marzán, and P. A. van Aken, Opt. Lett. **34**, 1003 (2009).
[27] W. Sigle, J. Nelayah, C. T. Koch, and P. A. van Aken, Opt. Lett. **34**, 2150 (2009).
[28] B. Schaffer, U. Hohenester, A. Trügler, and F. Hofer, Phys. Rev. B **79**, 041401 (2009).
[29] C. Xue and C. A. Mirkin, Angew. Chem., Int. Ed. **46**, 2036 (2007).
[30] R. Jin, Y. Cao, C. A. Mirkin, K. L. Kelly, G. C. Schatz, and J. G. Zheng, Science **294**, 1901 (2001).
[31] S. S. Shankar, A. Rai, B. Ankamwar, A. Singh, A. Ahmad, and M. Sastry, Nat. Mater. **3**, 482 (2004).
[32] N. Malikova, I. Pastoriza-Santos, M. Schierhorn, N. A. Kotov, and L. M. Liz-Marzán, Langmuir **18**, 3694 (2002).
[33] J. E. Millstone, S. J. Hurst, G. S. Métraux, J. I. Cutler, and C. A. Mirkin, Small **5**, 646 (2009).
[34] H. Uhlemann and H. Rose, Optik (Stuttgart) **96**, 163 (1994).
[35] H. Rose, Ultramicroscopy **78**, 13 (1999).
[36] L. Gu, V. Srot, W. Sigle, C. T. Koch, P. A. van Aken, F. Scholz, S. B. Thapa, C. Kirchner, M. Jetter, and M. Rühle, Phys. Rev. B **75**, 195214 (2007).
[37] E. Essers, G. Benner, T. Mandler, S. Meyer, D. Mittmann, M. Schnell, and R. Höschen, Ultramicroscopy **110,** 971 (2010).
[38] C. T. Koch, W. Sigle, R. Höschen, M. Rühle, E. Essers, G. Benner, and M. Matijevic, Microsc. Microanal. **12**, 506 (2006).
[39] R. F. Egerton, *Electron Energy-Loss Spectroscopy in the Electron Microscope*, 2nd ed. (Plenum Press, New York, 1996).
[40] N. Talebi and M. Shahabadi, J. Opt. Soc. Am. B **27**, 2273 (2010).
[41] N. Talebi and M. Shahabadi, J. Phys. D **43**, 135302 (2010).
[42] N. V. Kartantzis and T. D. Tsiboukis, *Higher-Order FDTD Schemes for Waveguide and Antenna Structures* (Morgan & Claypool, San Rafael, CA, 2006), p. 108.
[43] P. A. Tirkas, C. A. Balanis, and R. A. Renaut, IEEE Trans. Antennas Propag. **40**, 1215 (1992).
[44] H. Ditlbacher, A. Hohenau, D. Wagner, U. Kreibig, M. Rogers, F. Hofer, F. R. Aussenegg, and J. R. Krenn, Phys. Rev. Lett. **95**, 257403 (2005).
[45] F. J. García de Abajo and M. Kociak, Phys. Rev. Lett. **100**, 106804 (2008).
[46] J. G. Van Bladel, *Electromagnetic Fields*, edited by D. G. Dudley (Wiley, Hoboken, NJ, 2007).
[47] J. Aizpurua, A. Howie, and F. J. Garcia de Abajo, Phys. Rev. B **60**, 11149 (1999).
[48] J. Nelayah, M. Kociak, O. Stéphan, N. Geuquet, L. Henrard, F. J. García de Abajo, I. Pastoriza-Santos, L. M. Liz-Marzan, and C. Colliex, Nano Lett. **10**, 902 (2010).

CHAPTER 9

Breaking the Mode Degeneracy of Surface Plasmon Resonances in a Triangular System

Nahid Talebi[1], Wilfried Sigle[1], Ralf Vogelgesang[4], Christoph T. Koch[2], Cristina Fernandez-Lopez[3], Luis M. Liz-Marzan[3], Burcu Ögüt[1], Melanie Rohm[1], and Peter A. van Aken[1]

1. Max Planck Institute for Metals Research, Heisenbergstraße 3, 70569, Stuttgart, Germany
2. Ulm University, Albert-Einstein-Allee 11, 89081, Ulm, Germany
3. Departamento de Quimica Fisica, Universidade de Vigo, 36310, Vigo, Spain
4. Max Planck Institute for Solid State Research, Heisenbergstraße 1, 70569, Stuttgart, Germany

The effect of symmetry breaking in a triangular gold nanoplatelet has been observed by using STEM-EELS measurements and the EFTEM imaging technique. The experiments have been supported by FDTD simulations. The experiments have been performed by Wilfried Sigle, simulations have been accomplished by Nahid Talebi, and the specimens have been provided by Cristina Fernandez-Lopez and Luis M. Liz-Marzan. All co-authors have contributed to the interpretation of the results.

Langmuir

Article

pubs.acs.org/Langmuir

Breaking the Mode Degeneracy of Surface Plasmon Resonances in a Triangular System

Nahid Talebi,*[,†] Wilfried Sigle,[†] Ralf Vogelgesang,[∥] Christoph T. Koch,[†,‡] Cristina Fernández-López, Luis M. Liz-Marzán,[§] Burcu Ögüt,[†] Melanie Rohm,[†] and Peter A. van Aken[†]

[†]Max Planck Institute for Intelligent Systems, Heisenbergstraße 3, D-70569 Stuttgart, Germany

[‡]Ulm University, Albert-Einstein-Allee 11, D-89081 Ulm, Germany

[§]Departamento de Química Física, Universidade de Vigo, 36310, Vigo, Spain

[∥]Max Planck Institute for Solid State Research, Heisenbergstraße 1, D-70569 Stuttgart, Germany

ABSTRACT: In this paper, we present a systematic investigation of symmetry-breaking in the plasmonic modes of triangular gold nanoprisms. Their geometrical C_{3v} symmetry is one of the simplest possible that allows degeneracy in the particle's mode spectrum. It is reduced to the nondegenerate symmetries C_v or E by positioning additional, smaller gold nanoprisms in close proximity, either in a lateral or a vertical configuration. Corresponding to the lower symmetry of the system, its eigenmodes also feature lower symmetries (C_v), or preserve only the identity (E) as symmetry. We discuss how breaking the symmetry of the plasmonic system not only breaks the degeneracy of some lower order modes, but also how it alters the damping and eigenenergies of the observed Fano-type resonances.

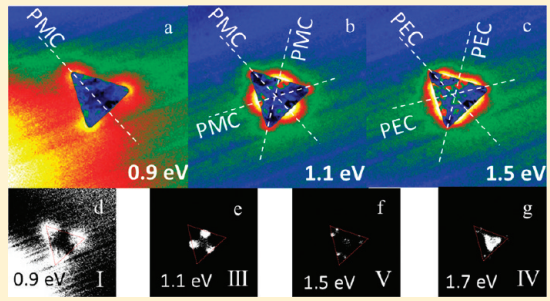

INTRODUCTION

Metallic triangular nanoparticles can support various localized surface plasmon resonances (LSPR). The basic resonance modes have field maxima at the corners, at the center of the side faces, and in the center of the triangle.[1] Using the discrete-dipole approximation, Shuford et al.[2] found that increasing the edge length and/or decreasing the prism height produces more intense red-shifted dipole peaks which was later on experimentally confirmed by Nelayah et al.[3] Shuford et al. also identified dipolar and quadrupolar modes. Experimental evidence for multipolar modes was given by Gu et al.[4] who found modes up to the fifth order. With the use of finite-difference time-domain (FDTD) calculations, they could show that it is wedge plasmons that give rise to the multipolar resonances with field maxima along the triangle edges. Furthermore, it was shown that the resonances form by interference of plasmons propagating around the triangle along the wedges and plasmons reflected at the triangle corners.

Symmetry breaking in a spherical system was studied by Wang et al.[5] showing the modification of selection rules. There are indications of symmetry breaking in triangular systems in refs 1 and 6. In chemistry, the relation of structural and orbital field symmetry is often used to predict the evolution of spectral properties. This approach has recently been transferred to the study of strongly coupled nanoparticles and identical hybridized nanosystems, such as plasmonic oligomers.[7−9] An excellent survey of this field is reported in ref 10.

Here, we systematically reduced the symmetry of a triangular system by studying LSPRs of coupled dissimilar triangles, that is, of triangles that are close to each other laterally or on top of each other. The presence of a second triangle reduces the symmetry of the system which in turn influences the plasmonic response. Plasmon resonances that are degenerate in a highly symmetric particle split into nondegenerate modes by breaking the symmetry. Understanding symmetry breaking effects may become an effective way of designing plasmonic systems for manipulation of the transmission of light.

EXPERIMENTAL AND CALCULATION DETAILS

Synthesis of Gold Nanoprisms. Tetrachloroauric acid ($HAuCl_4{\cdot}3H_2O$) and sodium borohydride ($NaBH_4$) were purchased from Aldrich. Ascorbic acid, citric acid ($C_6H_5O_7Na_3{\cdot}2H_2O$), potassium iodide (99%), and sodium hydroxide (97%) were supplied by Sigma. Cetyltrimethylammonium bromide (CTAB) was procured from Fluka. All chemicals were used as received. Milli-Q grade water was used in all preparations. The synthesis of Au nanoprisms was based on a seeded growth method.[11] Au nanoparticle seeds (average diameter ≈ 5 nm) were prepared by adding $NaBH_4$ (100 mM, 1 mL) to $HAuCl_4$ aqueous solution (0.27 mM, 37 mL) containing 10^{-5} mol of sodium citrate. After 5 min under vigorous stirring, the mixture was allowed to react overnight to allow the complete hydrolysis of unreacted $NaBH_4$. Three growth solutions were prepared for the seed-mediated growth steps. The first two solutions (A and B) were identical and contained $HAuCl_4$ (10 mM, 0.25 mL), NaOH (0.1 M, 0.05 mL), ascorbic acid

Special Issue: Colloidal Nanoplasmonics

Received: January 12, 2012
Revised: March 21, 2012
Published: March 22, 2012

(0.1 M, 0.05 mL), and CTAB (0.05 M, 9 mL; also containing 75 μL of 0.1 M KI). The final growth solution (C) comprised $HAuCl_4$ (10 mM, 2.5 mL), NaOH (0.1 M, 0.50 mL), ascorbic acid (0.1 M, 0.50 mL), and CTAB (0.05 M, 90 mL; with 75 μL of 0.1 M KI). Particle formation was initiated by adding 1 mL of seed solution to growth solution A. The solution was gently shaken, and then 1 mL of this mixture was immediately added to growth solution B. After shaking, all of the resulting mixture was added to solution C. After the final addition, the color of C changed from clear to purple over a period of 30 min.

Transmission Electron Microscopy. For imaging and electron-energy-loss spectroscopy (EELS), the Zeiss SESAM microscope[12] was used. This instrument is equipped with an omega-type electron monochromator which allows an energy resolution below 100 meV. This is important for the detection of surface plasmons because the tail of the elastic peak at zero energy loss overlaps with the energy-loss region of surface plasmons. Electron monochromation largely reduces the tail intensity. After passing the thin sample, electrons exhibit a quasi-continuous energy-loss spectrum, dominated by bulk plasmon excitations, but also excitations due to surface plasmons, interband transitions, core-loss excitations, and so forth. Electrons of different energy are dispersed in the in-column MANDOLINE energy filter[13] resulting in an energy-loss spectrum in its energy-dispersive plane. Using a mechanical slit (0.2 eV energy width in our case) electrons of a particular energy loss can be selected and an image is formed only from these electrons. This is known as energy-filtering TEM (EFTEM). By changing the high voltage of the microscope, the selected energy loss is varied, in our case from 0 to 4 eV. This ensures that the electrons passing the energy filter have constant energy and no degradation of the optical properties of the filter takes place. In fact, EFTEM image series are always recorded from high to low energy loss because image intensity increases dramatically toward 0 eV energy loss. By doing so, image artifacts from scintillator afterglow are avoided. The resulting EFTEM image series can be considered as a 3D data cube with two spatial dimensions and an energy axis. The EFTEM images are recorded on a 2048 × 2048 pixel CCD camera. For EFTEM, the camera is typically binned by a factor of 4, resulting in 256 × 256 pixel images, in order to reduce noise. Spatial resolution is not affected by binning because of the limitations of resolution mentioned below. Complementary to EFTEM, EELS spectra can be recorded from small areas by focusing the electron beam on a sub-nm spot. Typical spectra of 2048 channels cover an energy range of about 20 eV. Line scans or 2D maps (EELS spectrum images, EELS-SI) are obtained by scanning the spot across the desired line (area). In order to have a reliable energy calibration, energy-loss spectra are recorded including the elastic peak at 0 eV. Because this is orders of magnitude stronger than the plasmon peaks of interest, the EELS spectrum is spread along the nondispersive direction of the CCD camera. This prevents saturation of the camera pixels. EFTEM and EELS-SI are complementary in the sense that EFTEM offers high spatial sampling and thus gives a fast overview of the spatial distribution of resonances, whereas EELS-SI gives better sampling and better signal-to-noise ratio in energy space. EELS-SI is therefore better suited to separate fine spectral details.

Spatial Resolution. Electron beams can nowadays be focused to sub-Å spots using aberration-corrected electron optics. This allows obtaining high-angle annular dark-field images of sub-Å resolution. Close to 1 Å resolution is also achieved using electrons that have excited deeply bound 1s- or 2p-electrons thus providing atomically resolved elemental maps. However, at small energy losses, the spatial resolution is degraded due to the long-range Coulomb force between the electron probe and the dielectric material. This can be understood from image formation theory.[14] A 200 keV electron having suffered 5 eV energy loss has a characteristic inelastic scattering angle of only 12.5 μrad. According to the Rayleigh criterion small scattering angles are related with poor spatial resolution. In the energy-loss range of interest for surface plasmons (0−5 eV), the spatial resolution is of the order of 5−10 nm.[4] This obviously far exceeds the electron probe size and is in the range of the latest scanning near-field optical microscopy techniques. An important advantage of electron spectroscopy is that energy losses from about 400 meV (λ = 3 μm) up to several keV (λ = 5 Å) can be detected. This of course covers the whole optical spectrum. Despite electron monochromation, below 400 meV, spectral details start to become invisible because of the overlap with the tail of the elastic peak at 0 eV.

Peak-Finding Algorithm. EFTEM is a highly efficient technique for the fast visualization of the spatial distribution of particular energy losses. However, in the regime of low energy losses, it reaches its limits when weak energy-loss features superimposed by a large background are to be displayed. This is because background subtraction is complicated due to the lack of an analytical background function, as is available at high energy losses. Therefore, we developed a simple peak-finding algorithm which allows displaying the spatial locations of weak spectral peaks. The algorithm was written in Digital Micrograph (Gatan) script language. For this, spectra are extracted from each image pixel (i, j) (i, j = 1... 256) of the EFTEM series data cube. In each spectrum, those energy positions are set to intensity "1" whose neighboring energy channels have lower intensity. All other energy values are set to intensity "0". This results in a new data cube with binary data. Cutting this new cube parallel to the x−y-plane directly displays the spatial distribution of spectral peaks. Peaks below 1 eV energy loss would normally not be detectable by this technique because they overlap severely with the tail of the elastic peak at 0 eV and therefore appear as a shoulder rather than as a peak. In order to identify also these peaks we eliminated the zero-loss tail by extrapolation and subtraction of a power-law function fitted to a region of the elastic peak between 0.3 and 0.45 eV.

FDTD Calculations. Using the finite-difference time-domain method, the electromagnetic response of the structure was theoretically investigated. In order to effectively resolve different modes of the structure, a symmetry decomposition technique was exploited. Considering a simple triangle with three symmetry planes, each mode can be distinguished by being either symmetric or antisymmetric with respect to a specific symmetry plane. Antisymmetric modes are distinguished by considering a perfect electric conductor (PEC) at the position of a symmetry plane, while the symmetric modes hold true by a perfect magnetic conductor (PMC) positioned at the same symmetry plane. In our analysis, we have used different polarizations of the excitation beams to satisfy the preassumed configurations of either PEC or PMC symmetry planes.

For our FDTD analysis, the computation domain was discretized by cubic cells of 5 nm side length and the normal Yee's mesh was exploited. To model the dispersive behavior of gold, the Drude model with two added critical-point functions was used.[15] A Ricker-wavelet function was introduced as the temporal dependence of the incident beam, which allows us to excite energetically different modes of the structure in only one simulation attempt. By applying a discrete Fourier transform technique, the near-field spectrum of the structures was obtained. We used the concept of an additive source in our code, which allows us to introduce a vibrating plane at a location of about 1 μm above the structure. The spatial distribution and the temporal delays at the different points of the excitation plane are controlled in a way to preserve the desired optical beam, so that either linearly polarized plane-waves or TE and TM modes of the free space are excited. The TE mode is the free-space mode of electromagnetic waves having no z-component of the electric field, while the TM mode has no z-component of the magnetic field.

RESULTS AND DISCUSSION

Figure 1 shows the bright-field TEM images of the structures that are investigated in this paper. The single triangle shown in Figure 1a exhibits three symmetry planes. The structure shown in Figure 1b is composed of a small triangle of only 120 nm edge length on top of a larger triangle of about the same size as that of the single triangle. The location of the small triangle is such that the structure has still one symmetry plane. The structure shown in Figure 1c has no symmetry plane. The

dx.doi.org/10.1021/la3001762 | Langmuir 2012, 28, 8867−8873

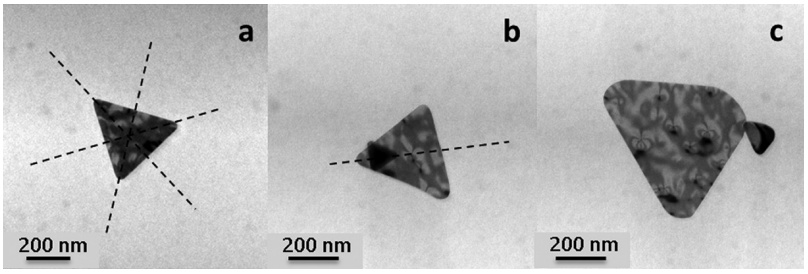

Figure 1. Bright-field images of (a) a single Au triangular nanoprism (edge length 400 nm), (b) a small Au triangle of 120 nm edge length on top of a larger triangular nanoprism with 370 nm edge length, and (c) a small Au triangle of 120 nm edge length located close to the corner of a larger nanoprism with 500 nm edge length. All nanoprisms are deposited on a 30 nm thick SiN_x membrane.

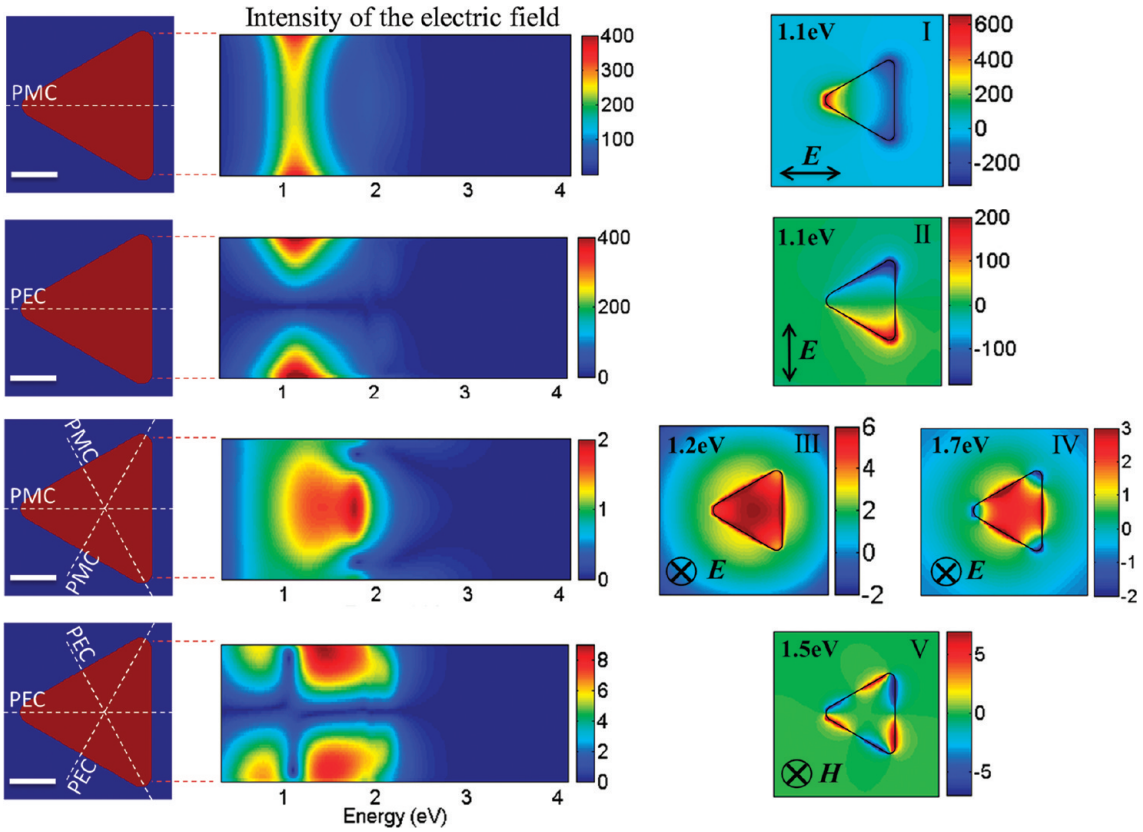

Figure 2. Plasmonic resonances of the single triangle, as calculated by FDTD, distinguished by their different symmetries. The middle column shows the intensity spectrum along the right edge. The right column shows the spatial distribution of the *z*-component of the electric field in the *xy*-plane at a distance of 5 nm above the nanoprism. The Intensity spectrum is normalized to the intensity of the incident wave. The scale-bars are all 150 nm.

height of the large and small triangles, determined from the low-loss EELS data, is 40 and 30 nm, respectively.

Before discussing the electromagnetic response of the structures, we recall that the fast electron transfers momentum mainly in the plane perpendicular to the propagation direction;[4] that is, it mainly excites modes having an electric field component in the *x*−*y*-plane. However, the electron energy loss is mediated by the *z* component of the electric field of the plasmon modes. FDTD simulations have been performed here using electric-field polarizations in the *x*−*y* plane (linear and circular) and along *z*. It should be mentioned that even though in some cases a TM_z excitation with the electric field polarized along the *z* direction is used, the scattered field will give rise to the polarizations in the other directions as well. That describes why the simulated results with optical excitations can be compared with the experimental EELS and EFTEM results.

Using FDTD, the optical modes of the simple Au nanoprism were numerically investigated. In order to determine the resonance energies, the distribution of the near-field intensity of the electric field along the edges of the nanoprism was computed. Figure 2 shows the various computed modes for the different configurations of symmetry planes. The middle column shows the intensity of the electric field computed at the location of the test points, positioned along the vertical edge of the triangle. The fundamental mode of the single triangle is the doubly degenerate E-mode of the C_{3v} group.[16,17] There is no difference in energy between the PMC and PEC symmetry plane configurations, although a distinct behavior is obvious for the spatial distribution of the field components. The right column shows the spatial distribution of the *z*-component of the electric field at the resonance energies, at 5 nm above the nanoprism. These very different modes can be excited optically by the two orthogonal linear polarizations, respectively. Nevertheless, their resonance energies are identical.

dx.doi.org/10.1021/la3001762 | *Langmuir* 2012, 28, 8867−8873

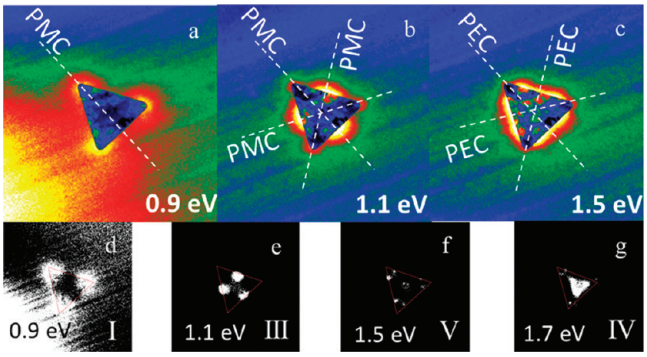

Figure 3. (a–c) EFTEM images and (d–g) peak maps of a single triangular nanoprism at the depicted energy losses. Roman numbers denote the modes as specified in Figure 2.

An intuitive understanding emerges if one considers the alternative circular symmetry. This kind of triangle does not distinguish between clockwise and anticlockwise direction. Correspondingly, optical absorption spectra using left- and right-circularly polarized light must reveal identical peak energies. As the linear polarization states can be constructed by superposition of the two circular ones, all their resonance energies are the same.

For an incident TM wave, the structure sustains two plasmonic resonances, distinguished by two peaks in the intensity spectrum. Both belong to the A_1-symmetry class of the C_{3v} group. The lower-energy mode (1.2 eV) with the hot spots mainly at the center of the edges is a monopolar mode, while the higher-energy one (1.7 eV) is a multipolar mode with a hot spot at the center of the triangle. These modes are denoted by III and IV, respectively.

The experimental EELS and EFTEM results of this structure are shown in Figure 3. From the EFTEM data (Figure 3a–c) modes I/II, III, and V (which has A_2-symmetry) are clearly distinguishable. However, detection of mode IV (Figure 3g) was only possible using the peak maps (Figure 3d–g) which show all monopolar and multipolar modes of the triangle. It should be noted that the modes shown as I and II in Figure 2 are degenerate and not distinguishable in the EFTEM images. It should also be noted that energy loss values from EFTEM data have an error of ±0.1 eV because of the slit width of 0.2 eV.

The 3-fold C_{3v} symmetry of the Au nanoprism is reduced to C_v by positioning a smaller nanoprism symmetrically on top of the large nanoprism, as shown in Figure 1b. This structure has only one symmetry plane, which classifies all eigenmodes into either A′ (symmetric) or A″ (antisymmetric).

Figure 4 shows the computed eigenmodes of this structure. It is obvious that modes I and II are still nearly degenerate, even though they suffered breaking of their former *E*-symmetry into A′ (mode I) and A″ (mode II). Apparently, the symmetry breaking potential of the small add-on particle is not large enough to induce significant energy splitting.

Another A′ eigenmode is observed at an energy of 1.9 eV. This originates from the coupling of the fundamental "corner mode" of the small triangle with an induced dipolar mode of the large triangle. It is important to note that this induced dipolar mode is not present in a single triangle at this eigenenergy.

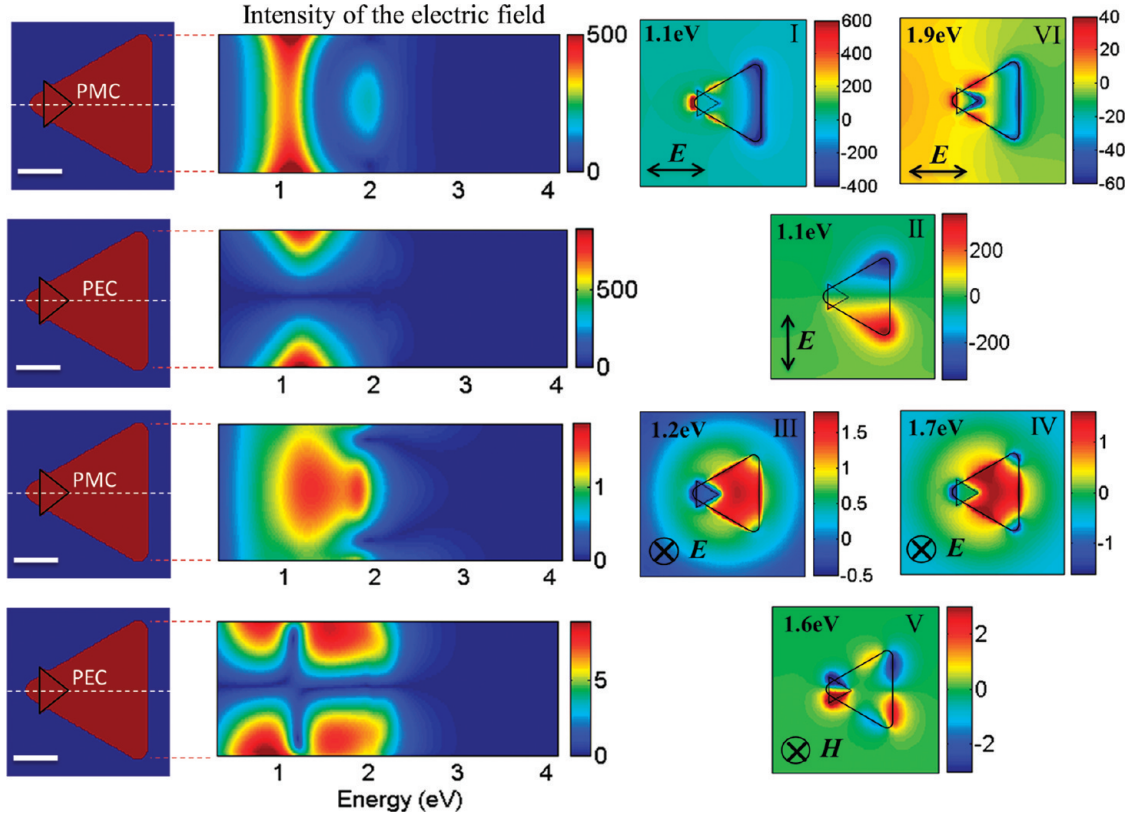

Figure 4. FDTD computed plasmonic resonances of the coupled triangles (Figure 1b) distinguished by their different symmetries. The middle column shows the intensity spectrum at the position of the test points shown in the left image. The right column shows the spatial distribution of the *z*-component of the electric field in the *xy*-plane at a distance of 5 nm above the nanoprism. The Intensity spectrum is normalized to the intensity of the incident wave. The scale-bars are all 150 nm.

dx.doi.org/10.1021/la3001762 | *Langmuir* 2012, 28, 8867–8873

Mode III has a broad spectrum and correspondingly a short dephasing, while mode IV has a narrow spectrum. This situation is appropriate for the excitation of Fano-type resonances.[18] However, in order to see this kind of resonance, an observable is required that is sensitive to the interference.[18] It is observed in the near-field spectrum at the location of some precisely defined test-points. Figure 5 shows the calculated near-field spectrum at the location of the test point depicted at the insets, for the case of both a simple nanoprism and the coupled prisms. The sharp dip at 1.6 eV is due to the interference of the modes III and IV. When comparing mode IV of the coupled system with the corresponding mode of a simple nanoprism, a broader resonance is observed for this structure. This is especially evident from the intensity spectrum. This phenomenon will result in a much narrower dip at the position of the test point depicted in the upper inset of Figure 5. It is evident that this dip is shallower in comparison with that of Figure 3. Moreover, the peaks are also shifted by 1 eV.

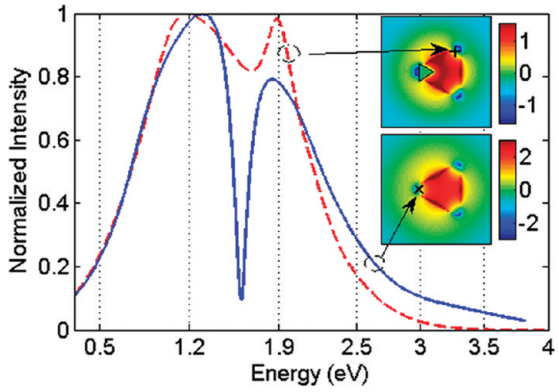

Figure 5. Fano resonance due to the overlap of the broad and narrow optical modes denoted as III and IV in the text, observed at the location of the test point depicted in the inset. The inset shows the calculated spatial distribution of the *z*-component of the electric field, at energy of 1.7 eV, normalized to the amplitude of the incident wave.

The damping of the plasmonic resonances can be readily computed from the width of the resonances. Moreover, the quality factor can be estimated as the ratio of the resonance frequency over the full width at half-maximum of a Gaussian resonance. To achieve this, a summation of Gaussian resonances is fitted to the spectrum, for both numerical and experimental results. Using this procedure, we have obtained the quality factor of the optical resonances shown in Figures 2 and 4. The highest quality factor corresponds to the optical mode IV for a simple triangle, which equals to 7.92. The quality factor of this mode reduces to 3.80 for the case of the coupled nanoprisms. Mode III has the lowest quality factor of only 1.20. The spectrum of this mode shows almost no change by reducing the symmetry of the nanoprism to *C*.

This shows that the presence of the smaller nanoprism has more effect on the radiation damping for the case of mode IV, since the material loss is almost the same for both modes. It can be readily noticed that the location of the smaller nanoprism is close to the hot spots preserved by this mode, which has

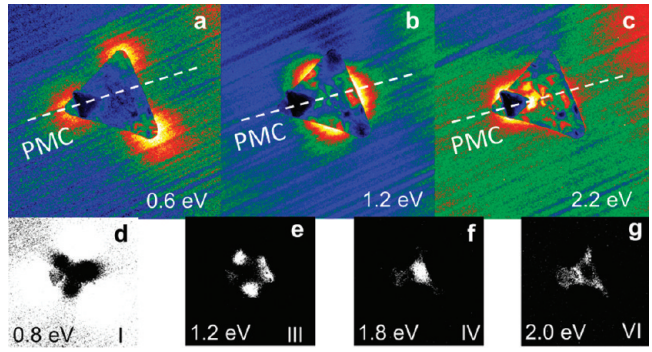

Figure 7. (a–c) EFTEM images of a small triangular Au nanoprism (edge length 120 nm) on top of a large Au nanoprism (edge length 370 nm). (d–h) peak maps at different energy losses, extracted from the EFTEM series. Roman numbers denote the modes as specified in Figure 5.

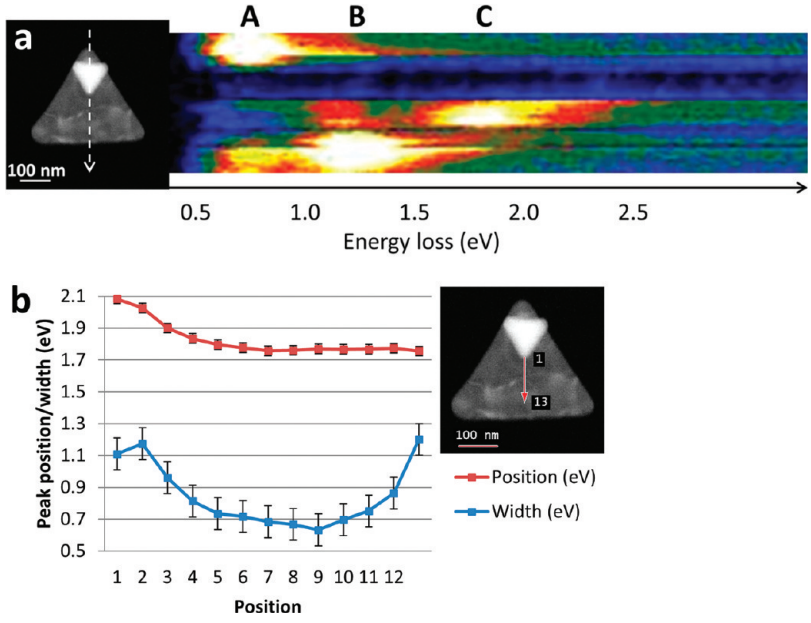

Figure 6. (a) 50 electron energy-loss spectra acquired along the arrow depicted in the left image. Three peaks at 0.75 eV (A), 1.2 eV (B), and 1.8 eV (C) are discernible. Peak A is excited close to the corner, peak B in the center, and peak C at the edge of the large triangle, compare also with Figure 8. (b) Dependence of position and width of peak C on the position of electron excitation, as indicated by the red arrow on the image at the right.

dx.doi.org/10.1021/la3001762 | *Langmuir* 2012, 28, 8867–8873

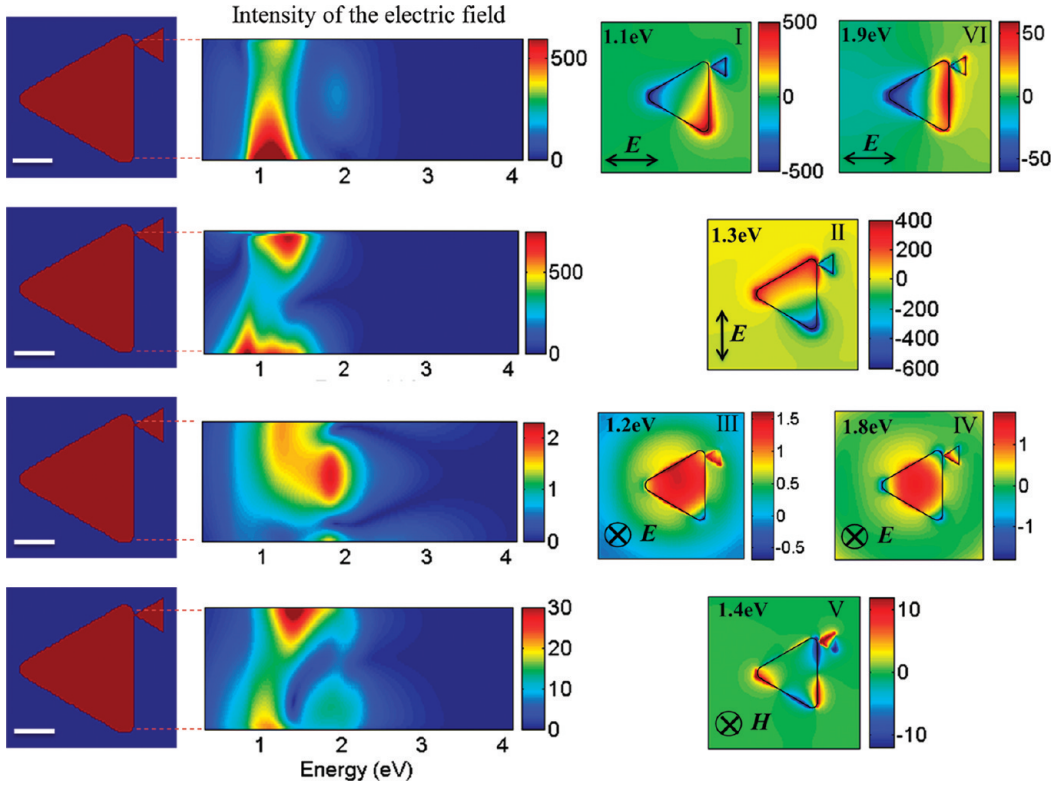

Figure 8. FDTD computed plasmonic resonances of the coupled triangles (Figure 1c). The middle column shows the intensity spectrum at the position of the test points depicted in the left image. The right column shows the spatial distribution of the *z*-component of the electric field in the *xy*-plane at a distance of 5 nm above the nanoprisms. The Intensity spectrum is normalized to the intensity of the incident wave. The scale-bars are all 150 nm.

resulted in more perturbation in comparison with mode III. Figure 6a shows a series of 50 EELS spectra acquired along the dashed arrow in the left image. Three resonance peaks, denoted by A, B, and C, can be distinguished at energy losses of 0.75, 1.2, and 1.8 eV, respectively. The corresponding EFTEM and peak maps at the identified eigenenergies (Figure 7) show a good correspondence to the FDTD data. Symmetry breaking is readily visible from Figure 7e. Careful inspection of Figure 6a shows that the energy of peak C red-shifts from the corner of the small triangle toward the edge of the large triangle. This can be attributed to the simultaneous excitation of modes V (1.7 eV) and VI (1.9 eV) by the fast electron. Moreover, the tail of the broad mode labeled as III can also interfere with the mentioned resonances. By fitting Gaussian functions to the 50 spectra this energy shift as well as the peak width were precisely determined (Figure 7b). Obviously the width of peak C exhibits a maximum near the sharp corner of the small triangle which we believe is due to radiation losses. The Fano resonance observed in the simulation by decomposing the optical modes into the symmetric and antisymmetric ones cannot be observed in the EELS analysis of the simple nanoprism. This is because by EELS and EFTEM are sensitive to any mode with nonvanishing E_z-nearfield component, i.e. EFTEM images display the incoherent superposition of electrons having excited any eigenmode of the structure with an eigenenergy within the range of the energy-selecting slit. Especially modes which are degenerate cannot be distinguished. Mode V has a resonance energy exactly located at the dip of the Fano resonance. The overlap of the spectra due to the excitation of all the modes will not allow an observer to report the interference occurring by the two resonances of III and IV.

The position of the small triangle on top of the Au nanoprism is such that it does not disturb the mode profiles of the large nanoprism, so their coupling is considered to be weak. This is the reason for the good agreement between the resonance energies of the structures depicted in Figure 1a and b.

The position of the smaller triangle shown in Figure 1c is such that the overall structure preserves no symmetry, that is, the appropriate symmetry group is E, which contains only the identity. The results of numerical investigations for the plasmonic resonances of this structure are shown in Figure 8. It should be mentioned that the size of the larger nanoprism in the simulation is assumed to be the same as for the previous structures, for the sake of an easier comparison between their resonance energies, and to show the effect of the symmetry breaking on the plasmonic resonances in a distinct way. As it is obvious from these results, the modes numbered as I and III are not degenerate anymore. Moreover, in comparison with the previous structures, these modes have exchanged their sequence with regard to their energies and the incident polarization. Similar to the previous structure, the fundamental mode of the small triangle is obvious at 1.9 eV.

The Fano-type resonances which were observable at the previous structures are no longer preserved here, which is directly related to the symmetry breaking phenomenon which has a strong effect on the distribution and the quality factor of the mode labeled as III.

Figure 9 shows the EFTEM and peak maps of the structure shown in Figure 1c. It should be noted that the symmetry of the simple nanoprism is broken not only by the smaller nanotriangle, but also because of the rounder upper corner of the large nanoprism. This may result in some degree of

dx.doi.org/10.1021/la3001762 | *Langmuir* 2012, 28, 8867−8873

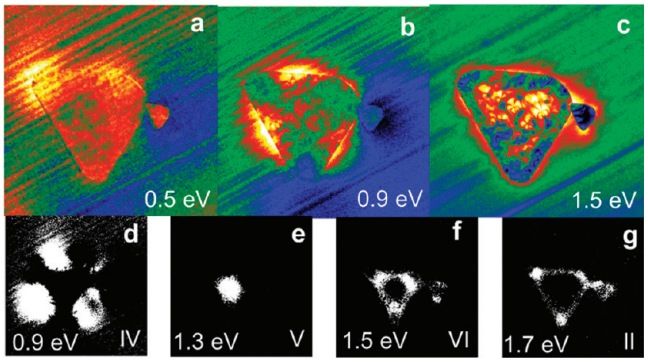

Figure 9. (a–c) EFTEM images of a small triangular Au nanoprism positioned close to the larger Au nanoprism, near to the upper right corner. (d–g) peak maps at different energy losses, extracted from the EFTEM series. Roman numbers denote the modes as specified in Figure 7.

deviation of the numerical results versus the experimental ones. The lowest-energy resonance (Figure 9a) is hardly visible because of the overlap with the tail of the strong elastic zero-loss peak. This energy is not present in the peak map plots (Figure 9d–g). The other resonances are in qualitative agreement with our numerical simulations.

■ CONCLUSIONS

We presented here a systematic study of the symmetry-breaking effect on the eigenmodes of a gold triangular nanoprism. We showed that breaking the symmetry of the structure results in splitting the degeneracy of the eigenmodes and even exchanging the sequence of eigenenergies regarding the incident polarization. Moreover, an induced dipolar mode of the nanoprism is observed at a much higher frequency than the corresponding mode of the simple nanoprism. Using the decomposition techniques, the different modes of the nanoprisms were investigated according to their symmetry. It has been shown that due to the interference of a broad monopolar mode with a narrow multipolar mode, a Fano-type resonance is observable at the near-field spectrum of a single nanoprism. In the broken symmetry case, this resonance rapidly deteriorates.

■ AUTHOR INFORMATION

Corresponding Author

*E-mail: talebi@is.mpg.de. Telephone: +49 711 689 3649. Fax: +49 711 689 3522.

Notes

The authors declare no competing financial interest.

■ ACKNOWLEDGMENTS

We would like to thank Dr. Isabel Pastoriza-Santos for her advice regarding the choice of the synthesis method. N.T. would like to thank the Alexander-von-Humboldt Foundation for the financial support. L.M.L.-M. acknowledges the ERC for an Advanced Grant (PLASMAQUO, 267867).

■ REFERENCES

(1) Nelayah, J.; Kociak, M.; Stéphan, O.; Garcia de Abajo, F. J.; Tencé, M.; Henrard, L.; Taverna, D.; Pastoriza-Santos, I.; Liz-Marzán, L. M.; Colliex, C. Mapping Surface Plasmons on a Single Metallic Nanoparticle. *Nat. Phys.* **2008**, *3*, 348–353.

(2) Shuford, K. L.; Ratner, M. A.; Schatz, G. C. Multipolar Excitation in Triangular Nanoprisms. *J. Chem. Phys.* **2005**, *123*, 114713-1–9.

(3) Nelayah, J; Kociak, M.; Stéphan, O.; Geuquet, N.; Henrard, L.; Garcia de Abajo, F. J.; Pastoriza-Santos, I.; Liz-Marzán, L. M. Colliex, Two-Dimensional Quasistatic Stationary Shoert Range Surface Plasmons in Flat Nanoprisms. C. *Nano Lett.* **2010**, *10*, 902–907.

(4) Gu, L.; Sigle, W.; Koch, C. T.; Ögüt, B.; van Aken, P. A.; Talebi, N.; Vogelgesang, R.; Mu, J.; Wen, X. Mao, Wedge-Plasmon Modes in Single-Crystalline Gold Nanoplatelets. *J. Phys. Rev. B* **2011**, *83*, 195433–1–7.

(5) Wang, H.; Wu, Y.; Lassiter, B.; Nehl, C. L.; Hafner, J. H.; Nordlander, P.; Halas, N. J. Symmetry Breaking in Individual Plasmonic Nanoparticles. *Proc. Natl. Acad. Sci. U.S.A.* **2006**, *103*, 10856–10860.

(6) Rang, M.; Jones, A. C.; Zhou, F.; Li, Z.-Y.; Wiley, B. J.; Xia, Y.; Raschke, M. B. Optical Near-Field Mapping of Plasmonic Nanoprisms. *Nano Lett.* **2008**, *8*, 3357–3363.

(7) Lassiter, J. B.; Sobhani, H.; Fan, J. A.; Kundun, J.; Capasso, F.; Nordlander, P.; Halas, N. J. Fano Resonances in Plasmonic Nanoclusters: Geometrical and Chemical Tunability. *Nano Lett.* **2010**, *10*, 3184–3189.

(8) Hentschel, M.; Saliba, M.; Vogelgesang, R.; Giessen, H.; Alivisatos, A. P.; Liu, N. Transition from Isolated to Collective Modes in Plasmonic Oligomers. *Nano Lett.* **2010**, *10*, 2721–2726.

(9) Hentschel, M.; Dregely, D.; Vogelgesang, R.; Giessen, H.; Liu, N. Plasmonic Oligomers: The Role of Individual Particles in Collective Behavior. *ACS Nano* **2011**, *5*, 2042–2050.

(10) Halas, N. J.; Lal, S.; Chang, W.; Link, S.; Nordlander, P. Plasmons in Strongly Coupled Metallic Nanostructures. *Chem. Rev.* **2011**, *111*, 3913–3961.

(11) Millstone, J. E.; Wei, W.; Jones, M. R.; Yoo, H.; Mirkin, C. A. Iodide Ions Control Seed-mediated Growth of Anisotropic Gold Nanoparticles. *Nano Lett.* **2008**, *8*, 2526–2529.

(12) Koch, C. T.; Sigle, W.; Höschen, R.; Rühle, M.; Essers, E.; Benner, G.; Matijevic, M. SESAM: exploring the frontiers of electron microscopy. *Microsc. Microanal.* **2006**, *12*, 506–514.

(13) Uhlemann, S.; Rose, H. Acceptance of Imaging Energy Filters. *Ultramicroscopy* **1996**, *63*, 161–167.

(14) Egerton, R. F. *Electron Energy-Loss Spectroscopy in the Electron Microscope*, 2nd ed.; Plenum Press: New York, 1996; pp 347–352.

(15) Etchegoin, P. G.; Le Ru, E. C.; Meyer, M. An Analytic Model for the Optical Properties of Gold. *J. Chem. Phys.* **2006**, *125*, 1564705.

(16) Harris, D. C.; Bertolucci, M. D. *Symmetry and Spectroscopy: Introduction to Vibrational and Electronic Spectroscopy*; Oxford University Press: New York, 1980.

(17) Bishop, D. M. *Group Theory and Chemistry*; Dover Publications: New York, 1993.

(18) Lukyanchuk, B; Zheludev, N. I.; Maier, S. A.; Halas, N. J.; Nordlander, P; Giessen, H.; Chong, C. T. The Fano Resonance in Plasmonic Nanostructures and Metamaterials. *Nat. Mater.* **2010**, *9*, 707–715.

CHAPTER 10

Conclusions and Future Outlook

The very rapidly evolving field of plasmonics, which will be a key element of various engineering and medical science applications in the very near future, is becoming more popular every single day. As the plasmonics research progresses, it is realized that the plasmonic behaviour can easily be manipulated by using different material systems and geometries.

The main objective of this doctorate project was to analyze plasmonic coupling behaviours of different structures. EELS and EFTEM imaging are of severe importance while measuring and identifying the plasmonic behaviour with nanometer spatial and a few tens of meV spectral resolution with short acquisition times, typically less than half an hour. EELS and EFTEM are also favourable as they allow detecting dark modes, which are normally undetectable with optical techniques. Moreover, the simulation results based on DDA, FEM, and 3D-FDTD gave a broader view of the electromagnetic characteristics of the structures to electron beam illumination. Plasmonic behaviours of rectangular slits, compilation of circular holes arranged in oligomer or grape-like shape, and nanoparticles having tariangular, hexagonal and truncated triangular shapes were investigated. Every experiment led to the discovery of new plasmonic phenomena during this PhD work.

The EFTEM experiments involving the single and double rectangular slits have given the possibility to directly illustrate Babinet's principle, which states that the particles and holes having the same geometry possess electromagnetically complementary characters. Besides this, plasmonics research on slit structures showed that DDSCAT is not appropriate for the simulation of holes having a diameter larger than ~200 nm as it requires a huge amount of time and computer memory. Therefore other techniques offering adaptive mesh refinement are more suitable for this purpose. HFSS simulation results, which are in perfect agreement with experimental findings, showed that the plasmonic modes observed along the length of the rectangular slits are Fabry-Pérot-like interferences. In addition, the closely placed slits hybridize

due to magnetic coupling through the connecting bridge. Moreover the rectangular system is a prototype for Babinet self-complementarity.

The comprehensive research on the compilation of circular holes arranged in different fashions revealed two different phenomena. Firstly, circular holes arranged in an oligomeric configuration led to the experimental observation of toroidal moments at optical wavelengths for the first time, which were confirmed through 3D-FDTD simulations. This is another example for the power of EFTEM imaging combined with 3D-FDTD simulations. Eigenmodes with toroidal character are impossible to detect with optical techniques due to their nearly radiation-free ultra-dark nature. Even if one surrounding hole or the central hole is removed, it is still possible to detect the toroidal mode, which is an optically ultra-dark mode. As future work, multilayers of oligomer nanocavities could be produced and investigated, as such a device with nearly no radiation loss can be a perfect candidate for Purcell effect applications. Secondly, a compilation of 6 holes forming a plasmonic grape structure showed different electromagnetic coupling phenomena. A hybridization scheme could be constructed based on the dipolar and quadrupolar resonances that are obtained from DDSCAT simulations for single holes and electromagnetic coupling through 3-hole resonances in the center of the grape structure. Circular holes arranged in different fashions are expected to play a crucial role for the design of components in plasmonic circuits as well as in solar cell engineering.

During investigations of single-crystalline gold nanoprisms, EFTEM experiments combined with 3D-FDTD has attributed the plasmonic behaviour to wedge plasmons independent from the prism shape. In addition, these structures could be beneficial for Fano resonance engineering applications by breaking the symmetry of the structures with the addition of one neighbour particle. The additional particle is important for switching on/off the Fano resonance.

Last but not least, there are still a lot of mysteries to be solved in the young world of plasmonics, such as the effect of grain boundaries on the plasmonic behaviour. Also specimen-preparation techniques using e-beam nanolithography (such as the results in supplementary chapter 4) could be improved, because these allow two or three dimensional manufacturing of nanostructures which possess properties that do not exist in nature, namely metamaterials. Investigations of chiral structures using this technique by using vortex beams might open new avenues to comprehend the dichroism phenomenon. Another alternative could be investigations

of graphene for plasmonic applications. As it is well known from recent literature, there is a growing trend in understanding the plasmonic properties of graphene. Although graphene can easily be damaged by a high-voltage electron beam, this could be prevented by using accelerating voltages below 80 keV.

Acknowledgements

It would not be possible to finish my doctorate work without the support of some people that I would especially like to mention below;

First of all I would like to thank Prof. Dr. Peter A. van Aken accepting me as a PhD student to his group. I am grateful for his guidance, support and the fruitful discussions throughout the article publication and thesis preparation procedure at a friendly atmosphere.

I owe my deepest gratitude to Prof. Dr. Wolfgang Jäger for accepting me as a PhD student to his Chair of Microanalysis of Materials at Materials Science Department in Christian-Albrechts-University of Kiel. His continuous support like a real father ever since I started my master studies in Kiel University is invaluable for me.

I am heartily thankful to my supervisor Dr. Wilfried Sigle, whose encouragement, guidance and support from initial to final level enabled me to develop and understand the subject.

I would like to express my appreciation to Dr. Ralf Vogelgesang for always enlightening my way with innovative ideas about my doctorate project, especially at the interpretation stage of my experimental results.

I would like to show my gratitudes to Prof. Dr. Christoph T. Koch, for recommending HFSS program as the simulation code for my experiments, his positive approach, and being a living example of how to be an excellent scientist.

Dr. Nahid Talebi Sarvari is acknowledged for performing the 3D-FDTD simulations.

Prof. Dr. Luc Henrard and Dr. Nicolas Geuquet deserve special thanks for their supervision about how to perform discrete dipole approximation simulations and their hospitality during my stay at their group at University of Namur, Belgium.

Dr. Jens Dorfmüller deserves thanks for the fruitful discussions especially at the very beginning of my PhD period.

The financial support from the European Union under the Framework 6 program under a contract for an Integrated Infrastructure Initiative, Reference 026019 (ESTEEM) is gratefully acknowledged.

“My dear sister” Dr. Vesna Srot deserves very very special thanks deep from my heart for everything that she did for me ever since I started living in Stuttgart. I am grateful for all the moral and scientific support that I got from her.

“My lovely supervisor” Ass. Prof. Dr. Jaysen Nelayah is acknowledged for the scientific support at the very beginning of my PhD work. I am thankful for his friendship and wonderful sense of humour, additionally.

I am indebted to Ulrike Eigenthaler, Ilse Lakemeyer, Kersten Hahn, Marion Kelsch, Ute Salzberger, Peter Kopold and Bernhard Fenk for the support during the specimen preparation and experimental stages of this work.

I would especially like to thank “my brother” Dr. Burak Özdöl for all the joy and friendship throughout my PhD and life in Stuttgart.

I further acknowledge my colleagues Cigdem Özsoy Keskinbora, Kahraman Keskinbora, Yeliz Unutulmazsoy and Burak Han Unutulmazsoy for their friendship and daily discussions about politics and life.

This thesis would not be possible without the moral support of my friends in Turkey and Germany, especially, Dr. Nazlı Olgun Kıyak, Özgün Bayramoğlu, Serpil Özpınar Önen, Erdem Kıyak, Nihan Sekirden Baraş, Dr. Başak Kısakürek Ibsen, Ceren Özaydin, Aynur Gerede, Sabina Bunea, and Lindsay Howe. I am really grateful to all of these people for bringing sunshine into my life and always being by my side for better or worse ever since we have met.

Finally, I would like to thank my mother Güzide Öğüt and my father Atanur Zafer Öğüt for their infinite love and affection throughout my whole life. This thesis, and every single success that I have achieved during this PhD work are dedicated to my parents. I am nothing without them.

Curriculum Vitae

PERSONAL INFORMATION

Name:	Burcu Öğüt
Date of Birth:	27.01.1984
Place of Birth:	Istanbul, Turkey
Marital Status:	Single
Nationality:	Turkish
E-mail:	ogut@is.mpg.de

EDUCATIONAL INFORMATION

2008 – today	Ph.D. in Materials Science and Engineering at Max Planck Institute for Intelligent Systems, Stuttgart, Germany Christian-Albrechts-University of Kiel, Germany
2006 – 2008	M.Sc. in Materials Science and Engineering at Christian-Albrechts-University of Kiel, Germany
2002 – 2006	B.Sc. in Metallurgical and Materials Engineering, Middle East Technical University, Ankara, Turkey
1995 – 2002	Burak Bora Anatolian High School, Istanbul, Turkey

PUBLICATIONS

Articles:

1. **B.Ögüt**, N. Talebi, R. Vogelgesang, W. Sigle, P. A. van Aken, in preparation (2012).

2. **B.Ögüt**, N. Talebi, R. Vogelgesang, W. Sigle, P. A. van Aken, "Toroidal plasmonic eigenmodes in oligomer nanocavities for the visible", Nano Letters, 12, (2012), 5239-5244.

3. N. Talebi, W. Sigle, R. Vogelgesang, C.T. Koch, C. Fernández-Lopez, L.M. Liz-Marzán, **B. Ögüt**, M. Rohm, P.A. van Aken, "Breaking the mode degeneracy of surface plasmon resonances in a triangular system", Langmuir, 28, (2012), 8867-8873.

4. **B. Ögüt**, R. Vogelgesang, W. Sigle, N. Talebi, C.T. Koch, P.A. van Aken, "Hybridized Metal Slit Eigenmodes as an Illustration of Babinet's Principle", ACS Nano, 5, (2011), 6701-6706.

5. P.A. van Aken, N.-Y. Jin-Phillipp, C.T. Koch, **B. Ögüt**, V.B. Özdöl, F. Phillipp, B. Rahmati, W. Sigle, V.Srot, "The Stuttgart Center for Electron Microscopy at the Max Planck Institute for Metals Research", International Journal of Materials Research, 102, (2011), 815-827.

6. L. Gu, W. Sigle, C.T. Koch, **B. Ögüt**, P.A. van Aken, N. Talebi, R. Vogelgesang, J. Mu, X. Wen, J. Mao, "Resonant Wedge Plasmon Modes in Single Crystalline Gold Nanoplatelets", Physical Review B, 83, (2011), 195433.

7. W. Sigle, J. Nelayah, C.T. Koch, **B. Ögüt**, L. Gu, P.A. van Aken, "EFTEM Study of Surface Plasmon Resonances in Silver Nanoholes", Ultramicroscopy, 110, (2010), 1094-1100.

8. D. Häußler, C. Morawe, U. Roß, **B. Ögüt**, E. Speiecker, W. Jäger, F. Hertlein, U. Heidorn, J. Wiesmann "Aperiodic W/B_4C Multilayer Systems for X-ray Optics: Quantitative Determination of Layer Thickness by HAADF-STEM and X-ray Reflectivity", Surface and Coatings Technology, 204, (2009), 1929-1932.

Proceedings:

1. W. Sigle, N. Talebi, **B. Ögüt**, L. Gu, R. Vogelgesang, C.T. Koch, and P.A. van Aken, "Surface plasmon eigenmodes in metallic nanostructures", Microscopy Conference MC2011 (2011), IM5.512, ISBN: 978-3-00-033910-3.

2. **B. Ögüt**, W. Sigle, N. Talebi, R. Vogelgesang, C.T. Koch, and P.A. van Aken, "Plasmonic eigenmodes of rectangular slits in thin silver films", Microscopy Conference MC 2011 (2011), IM5.P163, ISBN: 978-3-00-033910-3.

3. W. Sigle, L. Gu, N. Talebi, **B. Ögüt**, C.T. Koch, R. Vogelgesang, and P.A. van Aken, "EELS and EFTEM of surface plasmon in metallic nanostructures", Microscopy and Microanalysis, 17 (Suppl 2), (2011) 762-763.

4. P. A. van Aken, W. Sigle, C. T. Koch, **B. Ögüt**, J. Nelayah, and L. Gu, "Low loss EFTEM Imaging of surface plasmon resonances in Ag nanostructures", *Microscopy and Microanalysis*, **16**, Suppl. 2 (2010) 1438-1439.

5. W. Sigle, J. Nelayah, C.T. Koch, **B. Ögüt**, and P.A. van Aken, "Surface plasmon resonance effects in a perforated Ag film studied by energy-filtering TEM", *Microscopy Conference 2009*, Aug. 30-Sept. 4, Graz, Austria: G. Kothleitner, M. Leisch (Eds.), MC 2009, (Verlag TU Graz, Graz) (2009) 1, 111-112.

6. **B. Ögüt**, W. Sigle, J. Nelayah, C.T. Koch, and P.A. van Aken, "Study of Surface Plasmon Resonances on Assemblies of Slits in Thin Ag Films by Low-loss EFTEM Imaging", *Microscopy Conference 2009*, Aug. 30-Sept. 4, Graz, Austria: G. Kothleitner, M. Leisch (Eds.), MC 2009, (Verlag TU Graz, Graz) (2009) 1, 131-132.

Abstracts:

1. W. Sigle, **B. Ögüt**, I. Alber, N. Talebi, M. Rohm, M.E. Toimil-Molares, R. Vogelgesang, and P.A. van Aken, "Surface-plasmon coupling in metallic nanostructures", The 15th Electron Microscopy Congress, EMC 2012, 16-21 September 2012, Manchester, England.

2. N. Talebi, R. Vogelgesang, L. Gu, W. Sigle, C.T. Koch, **B. Ögüt**, M. Rohm, L.M. Liz-Marzán, and P.A. van Aken, "Surface-plasmon modes and mode degeneracy in a triangular system", The 15th Electron Microscopy Congress, EMC 2012, 16-21 September 2012, Manchester, England.

3. N. Talebi, R. Vogelgesang, L. Gu, W. Sigle, C.T. Koch, **B. Ögüt**, M. Rohm, L.M. Liz-Marzan, and P.A. van Aken, "Surface-plasmon modes and mode degeneracy in a triangular system", Symposium 1C, XXI. International Materials Research Congress 2012, 12-17 August, Cancun, Mexico.

4. W. Sigle, **B. Ögüt**, I. Alber, N. Talebi, M. Rohm, M.E. Toimil-Molares, R. Vogelgesang, and P.A. van Aken, "Surface-plasmon coupling in metallic nanostructures", Symposium 1C, XXI. International Materials Research Congress 2012, 12-17 August, Cancun, Mexico.

5. W. Sigle, **B. Ögüt**, I. Alber, N. Talebi, M. Rohm, M.E. Toimil-Molares, R. Vogelgesang, and P.A. van Aken, "Coupled surface-plasmons and Babinet complimentarity in nanowire and slit dimers", 12th International Conference on near-field optics, nanophotonics and related techniques, NFO 2012, (2012) San Sebastian, Spain.

6. N. Talebi, R. Vogelgesang, L. Gu, W. Sigle, C.T. Koch, **B. Ögüt**, M. Rohm, L.M. Liz-Marzan, and P.A. van Aken, "Real-space imaging of localized and delocalized plasmonic modes

in triangular nanostructures", 12th International Conference on near-field optics, nanophotonics and related techniques, NFO 2012, (2012) San Sebastian, Spain.

7. M. Rohm, T. Reindl, W. Sigle, **B. Ögüt**, N. Talebi, R. Vogelgesang, and P.A. van Aken, "Surface plasmon coupling in split ring resonator dimers", 12th International Conference on near-field optics, nanophotonics and related techniques, NFO 2012, (2012) San Sebastian, Spain.

8. N. Talebi, W. Sigle, R. Vogelgesang, **B. Ögüt**, L. Gu, C.T. Koch, and P. A. van Aken, "From localized to long-range plasmons in metallic nano-platelets", 3rd International conference on Metamaterials, Photonic Crystals and Plasmonics, META 2012, 19-22 April, Paris, France.

9. **B. Ögüt**, W. Sigle, N. Talebi, R. Vogelgesang, C.T. Koch, and P.A. van Aken, "Plasmonic eigenmodes of rectangular apertures in thin silver films", Summer School on Plasmonics 2, (3-7 October 2011), Porquerolles Island, Côte d'Azur, France.

10. W. Sigle, N. Talebi, **B. Ögüt**, L. Gu, R. Vogelgesang, C.T. Koch, and P.A. van Aken, "Wedge plasmon eigenmodes in metallic nanostructures", Summer School on Plasmonics 2, (3-7 October 2011), Porquerolles Island, Côte d'Azur, France.

11. P. A. van Aken, W. Sigle, **B. Ögüt**, N. Talebi, C.T. Koch, and R. Vogelgesang, "Plasmonic eigenmodes in metallic structures", International Workshop on Nanoplasmonics for Energy and Environment (IWONEE), 7-10 June 2011, Sanxenxo, Spain.

12. **B. Ögüt**, W. Sigle, N. Talebi, C. T. Koch, P.A. van Aken, and R. Vogelgesang, "Plasmonic eigenmodes in rectangular apertures in thin single films", The fifth International Conference on Surface Plasmon Photonics (SPP5), 15-20 May 2011, Busan, South Korea.

13. P.A. van Aken, W. Sigle, **B. Ögüt**, N. Talebi, C.T. Koch, and R. Vogelgesang, "Excitation of surface plasmon resonances in metallic nanostructures", The fifth International Conference on Surface Plasmon Photonics (SPP5), 15-20 May 2011, Busan, South Korea.

14. W. Sigle, **B. Ögüt**, C.T. Koch, N. Talebi, R. Vogelgesang, and P. A. van Aken, "EELS and EFTEM of metallic structures",Nano structures on surfaces and light scattering Proceedings" Institut für Werkstofftechnik, IWT, 24-25 March 2011, Bremen, Germany.

15. W. Sigle, **B. Ögüt**, C.T. Koch, P.A. van Aken, "Surface plasmon resonance effects in Ag nanoholes studied by energy-filtering TEM", MRS Fall Meeting 2010, Boston, USA, M.4.2.

16. **B. Ögüt**, W. Sigle, C.T. Koch and P.A. van Aken, "Study of surface plasmon resonances on rectangular slits in thin Ag films by low-loss EFTEM imaging", Fourth International Congress

on Advanced Electromagnetic Materials in Microwaves and Optics (METAMATERIALS IV): Proceedings, (2010) Karlsruhe, Germany.

17. W. Sigle, J. Nelayah, C.T. Koch, **B. Ögüt**, and P. A. van Aken, "Excitation of surface plasmons in perforated Ag films by fast electrons", Fourth International Congress on Advanced Electromagnetic Materials in Microwaves and Optics (METAMATERIALS IV): Proceedings, (2010) Karlsruhe, Germany.

18. P. A. van Aken, **B. Ögüt**, W. Sigle, and C. T. Koch, "Excitation of surface plasmon resonances in nanostructured Ag films", *IMC 17-Proceedings*, Rio de Janeiro, Brazil (2010), I5.12.

19. P.A. van Aken, W. Sigle, C.T. Koch, and **B. Ögüt**, "EFTEM study of surface plasmon resonances in silver nanostructures", Symposium Q, EMRS Spring Meeting, 7-11 June 2010, Strasbourg, France.

20. **B. Ögüt**, W. Sigle, J. Nelayah, C.T. Koch, and P.A. van Aken, "Study of Surface Plasmon Resonances on Assemblies of Slits in Thin Ag Films by Low-loss EFTEM Imaging", 60th IUVSTA Workshop, "Low Energy Spectroscopy and Simulation", 11-13 November 2009, Vienna, Austria.

ORAL PRESENTATIONS

1. B. Ögüt, "Tomorrow of plasmonics with aberration corrected transmission electron microscopy", StEM Workshop on Advanced Transmission Electron Microscopy Techniques, 11^{th}-13^{th} July 2012, Ringberg Castle, Lake Tegernsee, Bavaria, Germany.

2. B. Ögüt, R. Vogelgesang, W. Sigle, N. Talebi, C.T. Koch, P.A. van Aken, "EFTEM imaging and FEM simulation of plasmonic eigenmodes in nanoslits", International Workshop on "Current Topics in Transmission Electron Microscopy: Plasmonics & Tomography", 27^{th}-29^{th} July 2011, Ringberg Castle, Lake Tegernsee, Bavaria, Germany.

3. B. Ögüt, W. Sigle, N. Talebi, C.T. Koch, P.A. van Aken, R. Vogelgesang "Plasmonic eigenmodes in rectangular apertures in thin silver films", The 5^{th} International Conference on Surface Plasmon Photonics, SPP5, 15^{th}-20^{th} May 2011, Busan, South Korea.

4. B. Ögüt, W. Sigle, C. T. Koch, P. A. van Aken, "Surface plasmon resonances on rectangular slits in thin Ag gilms by low-loss EFTEM imaging", Short Lecture at Materials Science Colloquium, 12^{th} July 2010, Max Planck Institute for Metals Research, Stuttgart, Germany.

POSTER PRESENTATIONS

1. M. Rohm, T. Reindl, W. Sigle, B. Ögüt*, N. Talebi, R. Vogelgesang, and P.A. van Aken, "Surface plasmon coupling in split ring resonator dimers", 12th International Conference on near-field optics, nanophotonics and related techniques, NFO 2012, (2012) San Sebastian, Spain. (*presenting author)

2. B. Ögüt, W. Sigle, N. Talebi, R. Vogelgesang, C.T. Koch, and P.A. van Aken, "Plasmonic eigenmodes of rectangular apertures in thin silver films", Summer School on Plasmonics 2, (3-7 October 2011), Porquerolles Island, Côte d'Azur, France.

3. B. Ögüt, W. Sigle, N. Talebi, R. Vogelgesang, C.T. Koch, and P.A. van Aken, "Plasmonic eigenmodes of rectangular slits in thin silver films", Microscopy Conference MC 2011 Kiel, Germany.

4. B. Ögüt, R. Vogelgesang, W. Sigle, N. Talebi, C. T. Koch, P. A. van Aken, "Hybridized metal slit eigenmodes as an illustration of Babinet's principle", International Workshop on "Current Topics in Transmission Electron Microscopy: Plasmonics & Tomography", 27^{th}-29^{th} July 2011, Ringberg Castle, Lake Tegernsee, Bavaria, Germany.

5. B. Ögüt, W. Sigle, C.T. Koch and P.A. van Aken, "Study of surface plasmon resonances on rectangular slits in thin Ag films by low-loss EFTEM imaging", Fourth International Congress on Advanced Electromagnetic Materials in Microwaves and Optics (METAMATERIALS IV):, 2010, Karlsruhe, Germany.

6. B. Ögüt, W. Sigle, J. Nelayah, C.T. Koch, and P.A. van Aken, "Study of Surface Plasmon Resonances on Assemblies of Slits in Thin Ag Films by Low-loss EFTEM Imaging", *Microscopy Conference 2009*, Aug. 30-Sept. 4, Graz, Austria.

7. B. Ögüt, W. Sigle, J. Nelayah, C.T. Koch, and P.A. van Aken, "Study of Surface Plasmon Resonances on Assemblies of Slits in Thin Ag Films by Low-loss EFTEM Imaging", 60_{th} IUVSTA Workshop, "Low Energy Spectroscopy and Simulation", 11-13 November 2009, Vienna, Austria.

CONFERENCES & WORKSHOPS ATTENDED

1. 12^{th} International Conference on Near Field Optics, Nanophotonics and Related Techniques, (3-7 September 2012), San Sebastian, Spain.

2. The Lindau Nobel Laureate Meeting, Boat trip (06 July 2012), representing MPI for Intelligent Systems, Lindau, Germany.

3. Summer School on Plasmonics 2, (3-7 October 2011), Porquerolles Island, Côte d'Azur, France.

4. Microscopy Conference MC 2011, organised by German Microscopy Society, (28 August-02 September 2011), Kiel, Germany.

5. International Workshop on "Current Topics in Transmission Electron Microscopy: Plasmonics and Tomography", (27-29 July 2011), Ringberg Castle, Lake Tegernsee, Bavaria, Germany.

6. The 5th International Conference on Surface Plasmon Photonics, SPP5, (15-20 May 2011), BEXCO, Busan, South Korea.

7. Workshop, "Nano structures on surfaces and light scattering", organised by Institut für Werkstofftechnik, IWT, (24-25 March 2011), Bremen, Germany.

8. Seventh Workshop on EELS/EFTEM, (27-29 October 2010), Zurich, Switzerland.

9. Fourth International Congress on Advanced Electromagnetic Materials in Microwaves and Optics, METAMATERIALS IV, (September 2010), Karlsruhe, Germany.

10. 60th IUVSTA Workshop, "Low Energy Spectroscopy and Simulation", (11-13 November 2009), Vienna, Austria.

11. Microscopy Conference 2009, MC 2009, (30 August - 4 September 2009), Graz, Austria.

12. International Workshop on "Current Topics in TEM: Plasmonics and Strain Mapping", (22-25 July 2009), Ringberg Castle, Lake Tegernsee, Bavaria, Germany.

13. Educational Workshop on Ceramics, METU Management Society, (March 2004), Ankara, Turkey.

AWARDS

1. Best Poster Prize at the 12th International Conference on Near Field Optics and Related Techniques, 3-7 September 2012, San Sebastian, Spain.

2. Best Poster Prize at the 5th International Conference on Surface Plasmon Photonics in Busan, South Korea.

2. Scholarship from German Electron Microscopy Society (DGE) covering the travelling expenses of MC 2011, Kiel, Germany.

ERKLÄRUNG

Hiermit erkläre ich, dass ich die vorliegende Arbeit selbständig und ohne unerlaubte Hilfe angefertigt habe. Es wurden keine anderen Hilfsmittel außer den angegebenen Quellen benutzt. Diese Arbeit wurde weder ganz noch zum Teil einer anderen Stelle im Rahmen eines Prüfungsverfahrens vorgelegt. Ferner habe ich noch keinen Promotionsversuch an dieser oder einer anderen Hochschule unternommen.

Burcu Öğüt